

Design and Development of a Monitoring Station for the Long-Term Investigation of Dust Pollution Effects on the Performance of PV Panels

by

Andreas Tangeni Ndapuka

*Thesis presented in partial fulfilment of the requirements for the degree
Master of Engineering in the Faculty of Engineering at the University of
Stellenbosch*



Supervisor:

Dr. Johann M. Strauss

-December 2015-

Declaration

By submitting this thesis electronically, I declare that the entirety of the work contained therein is my own, original work, that I am the sole author thereof (save to the extent explicitly otherwise stated), that reproduction and publication thereof by University of Stellenbosch will not infringe any third party rights and that I have not previously in its entirety or in part submitted it for obtaining any qualification.

December 2015

Copyright © 2015 University of Stellenbosch

All rights reserved

Abstract

The past decade has seen impressive growth of the photovoltaic solar power industry as a response to increased global energy demand and a quest for sustainable energy supply. It is necessary to understand the natural challenges that are affecting this industry to promote efficient and economic use of solar power in South Africa and elsewhere.

Photovoltaic modules are widely regarded as maintenance-free power generators or are often marketed as such. While this might particularly be true for most of the small rooftop installations, the same cannot be said about large photovoltaic power plants. Large photovoltaic plants have to be continuously monitored and corrective measures must be taken in a timeously manner if they are to ensure maximum power yield.

The challenges facing solar PV installations vary from place to place. In dry and semi-arid areas (like in large areas in South Africa), dust pollution is one of the most serious challenges that large PV plants have to battle with and is thus a research area of interest. While the effect of dust pollution on the yield of solar panels have been confirmed and documented in the Middle East and North African (MENA) regions, studies on this crucial aspect in the region of Sub-Saharan Africa are particularly rare.

In this project, a monitoring station has been developed for long-term monitoring of dust pollution and its effects on the performance of PV modules. It may also be used in future to aid in the forecasting and planning of cleaning needs and costs for a particular site.

The station is pole mounted and consists of two identical solar panels, two active loads to load the panels as desired, a maximum power point tracker that serves as a battery charger for a 12V battery, and a control system for the operation of the station and communication to external devices or systems.

The station was designed to collect data (e.g. panel voltage, current, temperatures and current-voltage curve) which can be accessed via different means for analysis. Collection of the data may be scheduled to be taken at intervals from 1 minute up to 60 minutes.

It is shown that the various subsystems were developed successfully and that it forms a good base for a pole mounted monitoring station for long-term monitoring of dust pollution.

Opsomming

Die afgelope dekade was daar indrukwekkende groei in die fotovoltaïese sonkrag industrie in reaksie op die toename in globale energieaanvraag en in die soeke na volhoubare energietoevoer. Dit is noodsaaklik om die natuurlike uitdagings wat hierdie industrie beïnvloed te verstaan ten einde die doeltreffende en ekonomiese aanwending van sonkrag in Suid-Afrika en elders te bevorder.

Fotovoltaïese modules word wyd gereken as onderhoudsvrye gratis generators van krag of word dikwels bemark as sodanig. Terwyl dit in besonder waar mag wees vir die meeste klein dakgebaseerde installasies, kan dieselfde nie gesê word vir groot fotovoltaïese sonkragaanlegte nie. Groot fotovoltaïese aanlegte moet deurlopend gemoniteer word en regstellende maatreëls moet tydig geneem word om maksimum energieopbrengs te verseker.

Die uitdagings wat fotovoltaïese sonkragaanlegte in die gesig staar varieer van plek tot plek. In droë halfwoestyn areas (soos in groot dele van Suid-Afrika) is stofbesoedeling een van die mees ernstige uitdagings wat oorkom moet word en is daarom 'n navorsingsarea van belang. Terwyl die uitwerking van stofbesoedeling op die opbrengs van sonpanele bevestig en gedokumenteer is vir die Midde-Oosterse – en Noord-Afrikaanse streke (Eng: MENA), is studies oor hierdie kritieke aspek besonder skaars vir die Sub-Sahara streek van Afrika.

In hierdie projek is 'n moniteringstasie ontwikkel vir die langtermynmonitering van stofbesoedeling en die uitwerking daarvan op die werkverrigting van fotovoltaïese modules. Dit mag ook gebruik word in die toekoms om te help met die voorspelling en beplanning van skoonmaakbehoefte en –koste vir 'n bepaalde terrein.

Die stasie is paalgemonteer en bestaan uit twee identiese sonpanele, twee aktiewe laste om die panele te belas soos verlang, 'n maksimumdrywingspuntvolger wat dien as batterylaaier 'n 12V battery, en 'n beheerstelsel om die stasie te bedryf en om met eksterne toestelle of stelsels te kommunikeer.

Die stasie is ontwerp om data in te samel (bv. paneelspanning, -stroom, -temperatuur en stroom-spanningskromme) wat weer toeganklik is via verskillende maniere vir analise. Insameling van die data mag geskeduleer word om geneem word met vanaf 1 minuut intervalle tot en met 60 minuut intervalle.

Daar word getoon dat die verskeie substelsels suksesvol ontwikkel is en dat dit 'n goeie basis vorm vir 'n paalgemonteerde moniteringstasie vir die langtermynmonitering van stofbesoedeling.

Acknowledgements

First and foremost, I would like to thank the Almighty God for His unconditional love, protection and guidance all the way. It is all because of His love and blessings that I look forward to the future with optimism.

I am expressing special appreciations for my supervisor, Dr. Johann Strauss, for your invaluable support and persistence. Thank you for sharing your wealth of knowledge and experience with me and for always believing in me even in the days when I doubted my own capabilities.

Special thanks go to all fellow students with whom I have shared the Energy Conversion Lab. Thank you for your supports of any form; from a cup of coffee to tackling those problems together.

I wish to record special gratitude to the University of Namibia, the Staff Development Office in particular, for the financial support and understanding during the turbulent times of this journey.

Special recognition goes to my entire family, friends and all the relatives for always being there for me. Your words of encouragement have always armed me with more strength.

I would like acknowledge the priceless contributions of this lovely person, Priskila. You have been the pillar of my strength throughout and you gave me reasons to smile even in the most difficult days.

Last, but not least I want to say thank you to the Namibian community in Kraaifontein. I highly value all your support during my stay in Stellenbosch.

Dedications

To
Aluhe Tukwafa

Table of Contents

List of Figures	xii
List of Tables	xv
Nomenclature	xvi
CHAPTER 1 INTRODUCTION	2
1.1 Overview	2
1.2 Brief Insight on Solar PV	2
1.3 Dust Pollution.....	4
1.4 Project Motivation.....	6
1.5 Project Description.....	8
1.6 Thesis Structure.....	8
CHAPTER 2 HIGH-LEVEL PROJECT OVERVIEW.....	11
2.1 Overview	11
2.2 The Station Structure.....	11
2.3 Preliminary Choices and Decisions.....	12
2.3.1 The Solar Panels	12
2.3.2 The MPPT Battery Charger	13
2.3.3 Active Load.....	13
2.3.4 Communication.....	14
2.3.5 The Microcontroller	15
2.3.6 Programming.....	15
2.3.7 The Control System	15
2.3.8 Cleaning Mechanism	16
2.3.9 Batteries	16
CHAPTER 3 THEORY AND LITERATURE REVIEW	17
3.1 Overview	17
3.2 The Solar Cell.....	17
3.2.1 Operating Principle	18
3.2.2 Equivalent Circuit	19
3.2.3 The I-V Curve	20
3.3 Dust Pollution and PV Performance	21

3.3.1	Effect of Depositions	22
3.3.2	Effect of Humidity and Rain.....	24
3.3.3	Effect of Wind.....	25
3.3.4	Effect of Tilt Angle	25
3.4	Maximum Power Point Tracking (MPPT) Battery Charger	26
3.4.1	Analysis of DC-DC Converters	27
3.4.2	The Switch	29
3.4.3	The Inductor.....	30
3.4.4	Freewheeling Diode	31
3.4.5	The Capacitors	31
3.4.6	Algorithms	32
3.5	Measurements.....	34
3.5.1	Current Measurement.....	35
3.5.2	Voltage Measurement	38
3.6	Signal Conditioning.....	38
3.6.1	Amplifier Circuit.....	38
3.6.2	Low-Pass Filter	39
3.7	Cleaning of PV Panels.....	40
CHAPTER 4 Design OF the MPPT BATTERY CHARGER.....		41
4.1	Overview	41
4.2	Hardware Design.....	41
4.2.1	Design Parameters	41
4.2.2	Power Supply	42
4.2.3	Current Measurement.....	43
4.2.4	Voltage Measurement	44
4.2.5	Sallen-Key Low-Pass Filter	45
4.2.6	The Switching Devices	46
4.2.7	Inductor Design.....	46
4.2.8	Capacitors Selection.....	49
4.2.9	Power Dissipation and Thermal Management.....	49
4.2.10	PCB Design.....	54
4.3	Software Design	55

4.3.1	PWM and Switching Frequency	55
4.3.2	Communication (USART)	56
4.3.3	ADCs and their Calibration	57
4.3.4	Real Time Clock (RTC).....	58
4.3.5	Operating and Control Modes.....	59
4.3.6	P&O Algorithm Implementation	60
4.4	Testing and Results	61
4.4.1	Algorithm Performance	62
4.4.2	Battery Charging Algorithm	65
4.4.3	Measurements Accuracy	66
4.4.4	Communication Effectiveness	67
4.4.5	Efficiency	67
4.4.6	Conclusion	68
CHAPTER 5 Active Load Design		69
5.1	Overview	69
5.2	Principle of Operation	70
5.3	Active Load Hardware Design.....	71
5.3.1	Design Parameters	71
5.3.2	Current Measurement.....	72
5.3.3	Voltage Measurement	72
5.3.4	Capacitor and Inductor Selection.....	72
5.3.5	Dumping Resistor	75
5.3.6	Power Supply	75
5.3.7	PCB Design.....	75
5.4	Software Design	76
5.4.1	Calibration.....	76
5.4.2	P&O Algorithm.....	78
5.5	Testing and Results	78
5.5.1	Experiment Setup.....	78
5.5.2	Algorithm Performance	79
5.5.3	IV Curve Derivation	82
5.5.4	Measurement Accuracy	82

5.5.5	Communication Effectiveness	83
5.5.6	Conclusion	83
CHAPTER 6 THE STATION.....		85
6.1	Overview	85
6.2	The Layout	86
6.3	Preliminary Settings	88
6.3.1	Device Address and Baud Rate.....	88
6.3.2	Time	88
6.4	User Interface	88
6.5	Operation Schedule and Coordination	89
6.6	Data Management	89
6.6.1	Data Logging	90
6.6.2	Error Handling	90
6.7	Cleaning Schedule.....	90
CHAPTER 7 RESULTS AND DISCUSSIONS		92
7.1	Overview	92
7.2	Results	92
7.2.1	Operation Data: Day 1	92
7.2.2	Operation Data: Day 2	93
7.2.3	Panel Temperature	94
7.2.4	Battery Charging.....	95
7.3	Unexpected Challenges	95
7.3.1	Microcontroller Size	96
7.3.2	Switching Noise and Measurement Accuracy	96
7.3.3	Components Availability Issues	96
CHAPTER 8 CONCLUSIONS AND RECOMMENDATIONS.....		97
8.1	Overview	97
8.2	Conclusion.....	97
8.3	Recommendations	98
Bibliography		99
Appendices.....		102
A.	MPPT Program Flow Diagrams.....	103

B.	MPPT Modbus Commands Documentation	109
C.	Active Load Flow Diagrams	111
D.	MPPT Test Results.....	113
E.	Active Load Modbus Commands Documentation.....	118
F.	MPPT BATTERY CHARGER Schematics and PCB Layout.....	121
G.	Active Load Schematics and PCB Layout.....	127
H.	Active Load Test Results	133
I.	Commissioning data.....	136
I.1	Active Loads Data: Day 1	136
I.2	Active Loads Data: Day 2.....	137
I.3	Temperatures: Day 2.....	138
I.4	MPPT Data: Day 2.....	139

List of Figures

Figure 1-1: Historical development in average efficiency of mono and polycrystalline PV modules [1].	3
Figure 1-2: Historical change of PV modules price [1]. The red line indicates the trend of price change.	3
Figure 1-3: Annual income and energy loss as a function of mean dust deposition densities on PV panels' surfaces [7].	6
Figure 2-1: Structure of the station's components.	11
Figure 3-1: Principle of Solar Cell operation [11].	18
Figure 3-2: (a) Solar Cell image (Source: EPIA) (b) Solar Cell equivalent circuit [11].	20
Figure 3-3: The $I-V$ curve and power output for a PV module [12].	21
Figure 3-4: Image showing increase of temperature in the area with depositions [15].	23
Figure 3-5: Effect of partial shading with and without bypass diodes [12].	23
Figure 3-6: Relationship between irradiance and relative humidity [16].	24
Figure 3-7: Soiling losses at different tilt angles [18].	26
Figure 3-8: Irradiance and temperature dependence characteristics [19].	26
Figure 3-9: Basic MPPT System.	27
Figure 3-10: (a) Buck Converter and (b) its Switching waveforms [21].	28
Figure 3-11: Hill-Climbing technique and the sign of the power gradient.	32
Figure 3-12: Flowchart of the perturbation cycle.	33
Figure 3-13: Measurement System Overview.	34
Figure 3-14: Low (left) and high (right) side current measurement [29].	35
Figure 3-15: Shunt Resistor current sensing technique.	35
Figure 3-16: Low-Pass Filtering System Overview.	39
Figure 4-1: Simplified MPPT Power Supply Circuit.	42
Figure 4-2: MPPT Current Measurement Circuit.	43
Figure 4-3: MPPT Voltage Measurement Circuit.	45
Figure 4-4: Sallen-Key low-pass filter.	45
Figure 4-5: Picture of the MPPT battery charger.	54
Figure 4-6: Flow diagram for PWM generation and switching frequency selection.	55
Figure 4-7: Flow Diagram for USART settings.	56
Figure 4-8: ADC calibration effects illustrated.	57

Figure 4-9: MPPT Operation and Control modes flow chart.59

Figure 4-10: Test Circuit of the MPPT battery charger.62

Figure 4-11: PV and Battery voltages before and after switching on the MPPT battery charger.63

Figure 4-12: Change in PV Current, output current and the duty cycle.63

Figure 4-13: Test Results: MPPT’s dynamic response to loading (Voltages).64

Figure 4-14: Test Results: MPPT’s dynamic response to loading (Currents and Duty Cycle).
.....64

Figure 4-15: Battery charging and control method [38].65

Figure 4-16: Battery Charging and Control results.66

Figure 4-17: MPPT Efficiency vs Duty Cycle.67

Figure 5-1: Block diagram of the station with two Active Loads included.69

Figure 5-2: Active Load Simplified Circuit.70

Figure 5-3: Active Load Simulation Circuit.72

Figure 5-4: Input current and voltage of the Active Load.73

Figure 5-5: Voltage and current after the first filter stage.73

Figure 5-6: Voltage and Current after the second filter stage.74

Figure 5-7: Active Load simulation results showing maximum load current switching waves.
.....74

Figure 5-8: Selected dumping resistor, 1Ω 350W [RS Components].75

Figure 5-9: The picture of the Active Load.76

Figure 5-10: Active Load Calibration procedures.77

Figure 5-11: Active Load Test Circuit.79

Figure 5-12: Active Load Test Results – PV Power, PV Voltage and Switching Duty Cycle.
.....80

Figure 5-13: Active Load Test Results – PV Current and PV Power.80

Figure 5-14: Active Load test results showing fluctuations of the operating voltage.81

Figure 5-15: Active Load Test Results showing Duty Cycle fluctuations.81

Figure 5-16: Active Load test results showing the derived $I - V$ curve.82

Figure 6-1: Figurative Architecture of the Station.85

Figure 6-2: The picture of the station as mounted on the roof (Front View).86

Figure 6-3: The picture of the station as mounted on the roof (Back View).87

Figure 6-4: Inside the enclosure.87

Figure 7-1: Power generated over time by both panels on day 1.	93
Figure 7-2: Power generated over time by both panels on day 2.	93
Figure 7-3: Temperatures of the panels recorded on day 2.	94
Figure 7-4: Effect of clouds on generated power and panels temperatures.....	94
Figure 7-5: Battery Voltage and charge current on day 2.....	95

List of Tables

Table 2-1: Characteristics of the solar panels at Standard Test Conditions (STC).....	13
Table 3-1: Analysis of Cleaning Mechanisms.	40
Table 4-1: MPPT Battery Charger Design Parameters.	42
Table 4-2: Selected MOSFET specifications.....	46
Table 4-3: Inductor Design Specifications.....	47
Table 4-4: Core Specifications.....	47
Table 4-5: Summary of the switching losses in the MPPT battery charger.....	52
Table 4-6: Heat Sink Specifications.....	53
Table 4-7: Characteristics (STC) of the test panels.	61
Table 4-8: Operating characteristics (STC) of two test panels in series.	61
Table 5-1: Active Load Design Parameters.	71

Nomenclature

AC:	Alternating Current	ISP:	In-System Programming
ADC:	Analog-to-Digital Converter	KCL:	Kirchhoff's Current Law
AWG:	American Wire Gauge	LED:	Light Emitting Diode
CCM:	Continuous Conduction Mode	MFB:	Multiple Feedback
CMRR:	Common Mode Rejection Ratio	MISO:	Master-In-Slave-Out
CRC:	Cyclic Redundancy Check	MOSFET:	Metal-Oxide Semiconductor Field-Effect Transistor
DC:	Direct Current	MOSI:	Master-Out-Slave-In
DC-DC:	Direct Current-to-Direct Current	MPP:	Maximum Power Point
DCM:	Discontinuous Conduction Mode	MPPT:	Maximum Power Point Tracker
DSC:	Digital Signal Controller	P&O:	Perturb and Observe
DSP:	Digital Signal Processor	PC:	Personal Computer
E&E:	Electrical and Electronic	PCB:	Printed Circuit Board
EEPROM:	Electrically Erasable Programmable Read-Only Memory	PTC:	Positive Temperature Coefficient
ESR:	Equivalent Series Resistance	PV:	Photovoltaic
GPIO:	General Purpose Input/Output	PWM:	Pulse Width Modulation
IC:	Integrated Circuit	RE:	Renewable Energy
IDE:	Integrated Development Environment	ROI:	Return On Investment
IGBT:	Insulated Gate Bipolar Transistor	RTC:	Real Time Clock
IPP:	Independent Power Producers	SCK:	Serial Clock
		SMPS:	Switch Mode Power Supply
		SPI:	Serial Peripheral Interface
		STC:	Standard Test Conditions
		USART:	Universal Synchronous Asynchronous Receiver/Transmitter

CHAPTER 1 INTRODUCTION

1.1 Overview

Escalating global energy demand, the quest for sustainable energy generation and the understanding that dependence on fossil fuels is finite, are some of the leading reasons that are transforming Renewable Energy (RE) into one of the most important areas of research and development today. Alternative sources of energy must be developed and augmented because they hold the solution to sustainable development, energy security, carbon footprint management as well as employment creation.

Although the South African solar industry is still in its infant stage, it is anticipated to grow unprecedentedly. The introduction of the Renewable Energy Independent Power Producer Procurement Programme is one of the factors that are leading the transformation of this sector.

1.2 Brief Insight on Solar PV

Solar Photovoltaic (PV) is one of the feasible alternative forms of energy sources. It is widely favourable because it uses energy from the sun which is abundantly available in most parts of the world at absolutely no cost. For as long as the sun continues to shine, solar energy is always there.

With the cost of solar modules decreasing considerably while their efficiency is showing an uphill trend, solar PV is emerging to be a worthwhile investment and a competitive energy source.

The last decade has seen significant increase in the efficiency of solar panels as shown in Figure 1-1. Furthermore, the drop in average price of solar panels has made them more affordable which led to doubling of their installed capacity as shown Figure 1-2.

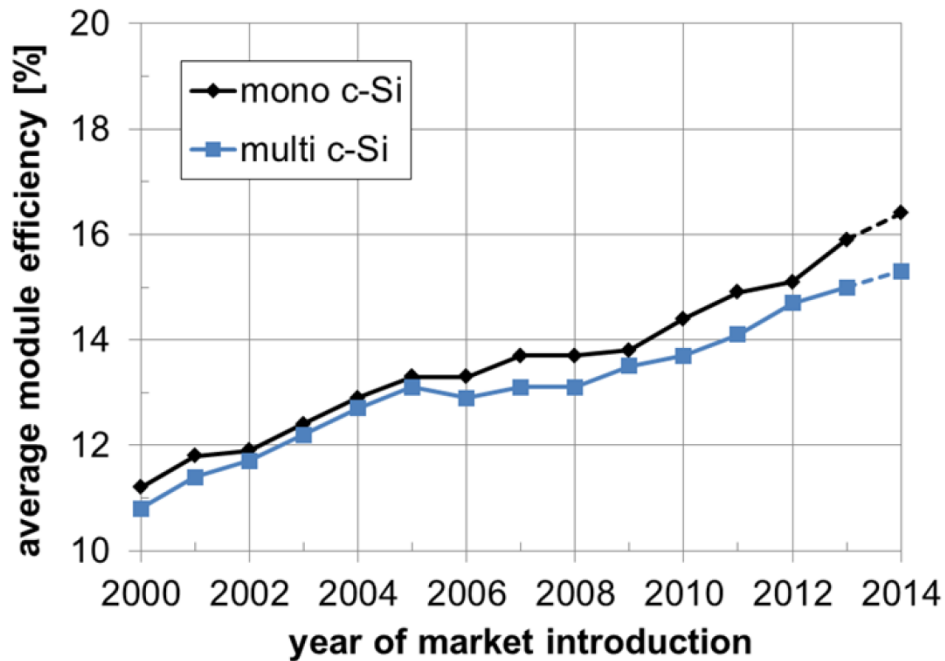


Figure 1-1: Historical development in average efficiency of mono and polycrystalline PV modules [1].

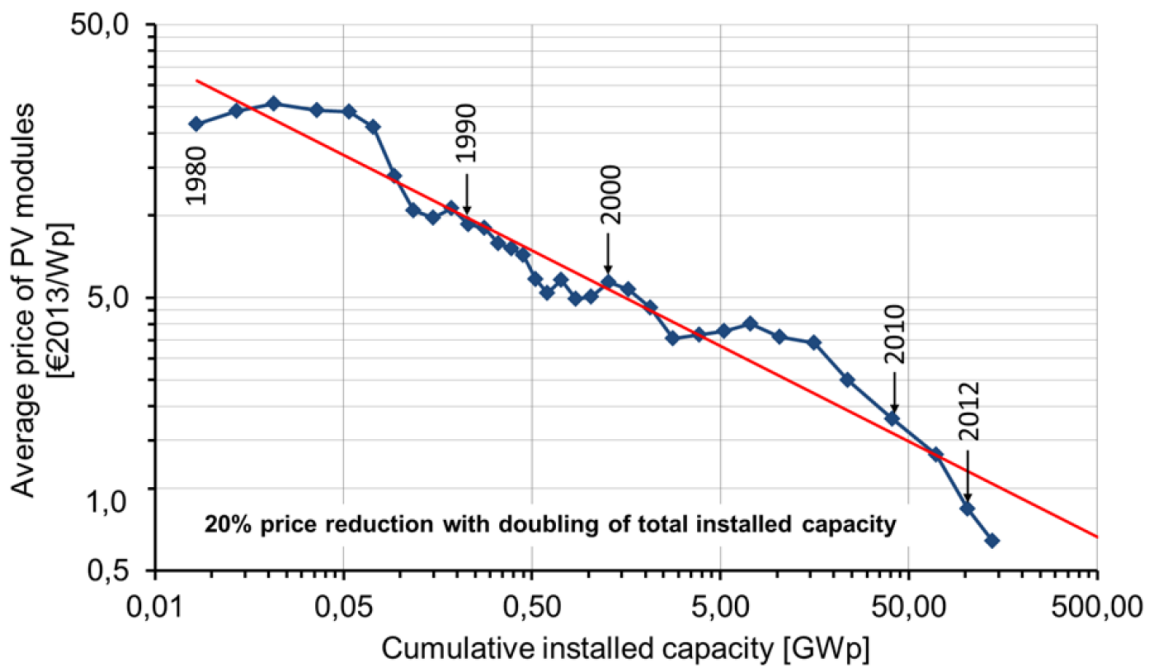


Figure 1-2: Historical change of PV modules price [1]. The red line indicates the trend of price change.

There are several reasons that make solar PV a competitive sector. Few of them are briefly discussed here.

Solar PV provides energy security and independence by reducing dependence from imports of fossil fuels (oil, gas or coal). With solar power, costs of transporting fossil fuels to power stations are completely eliminated. On top of that, solar power eases the decentralisation of energy generation thereby avoiding long transmission and distribution lines. Solar PV is a suitable option for rural electrification in countries like Namibia which are sparsely populated but receive many hours of direct solar radiation per day throughout the year. Solar power is also attractive because it produces clean energy and as a result mitigates the emissions of greenhouse gasses. Finally, solar power can be easily customised to generate just the energy that is needed. It is ideal for demand based generation stations.

Apart from energy production, solar industry also provides opportunities for employment to the local community during construction, maintenance and operation. In countries with net-metering and feed-in-tariffs, solar PV serves as source of income for many people through the Independent Power Producers (IPP) agreements and other means. In Germany, for example, approximately 56 000 people were employed in the solar PV industry in 2013.

Other features like absence of fuel costs and moving parts (wear and tear) significantly reduce the operating and maintenance costs of PV installations; a great benefit when compared to fuel based energy sources.

1.3 Dust Pollution

When solar panels are in operation, they are exposed not only to solar irradiance but also to all meteorological conditions. Some of these atmospheric conditions are harsh and they pose challenges to the performance and yield of the panels.

The challenges facing the solar industry vary highly with geographic locations, seasons and weather conditions. In cold regions, the industry is faced with snow which covers the panel's surface during winter, thereby reducing the penetration of sunlight to the solar cells. In tropical regions, the industry is battling with shading from tall trees and high ambient temperatures, while in arid and desert areas, high ambient temperatures and dust pollution or soiling are the major concerns.

Dust is a term used to describe minute solid particles less than 500 μm in diameter. Other minute pollutants such as bacteria and fungi, and microfibers emanating from clothes, carpets and fabrics are also classified as dust when settled on surfaces.

Dust pollution, also referred to as soiling, is a consequence of various environmental and weather conditions. Agricultural, pedestrian and vehicular activities, volcanic eruptions, industrial pollution and wind contribute immensely to dust concentration in the atmosphere.

As mentioned earlier, dust pollution is one of the serious natural challenges that PV plant operators are likely to experience in South Africa and other arid countries of southern Africa. The extent to which dust pollution affects PV power production varies widely from location to location. However, the main and common issue here is that dust pollution results in solar panels generating less power than expected. Regardless of its quantity, in terms of efficiency, any power loss is a concern and it must be addressed where possible.

Based on land availability, open spaces like farms and coastal areas might be the most appropriate and favourable places for solar parks. However, the same sites are also prone to dust pollution. Even in urban areas, industrial and transportation activities can greatly contribute to the pollution of PV panels and affect their yield.

Commercial solar panels are already characterised with intrinsic low conversion efficiency, therefore additional power losses are absolutely undesirable.

It is widely documented in most parts of the globe that the accumulation of dust particles, bird droppings, leaves and salt debris on PV panel's surface has a negative effect on their energy output.

In Malaysia up to 50% power loss due to accumulated dust has been recorded. In Egypt up to 25% reduction in panel's output due to dust depositions has been reported just after two months without cleaning the panels, with the losses increasing to 40% after one year of continuous dust accumulation.

A study by Google on its 1.6MW solar installation, in the USA, found that flat-mounted panel's output has doubled when panels were cleaned after 15 months of dust accumulation. Eight months later, the panels were cleaned again and the output shot up by 36% [2].

While such power losses might not have significant consequences for small residential installations, it can result in low Return on Investment (ROI) for large PV plants which can eventually lead to longer payback times and other financial complications.

The relationship between power losses and income losses as a result of dust pollution was investigated in Greece as presented in Figure 1-3. The results evidently show that income losses increased with the increase in dust pollution.

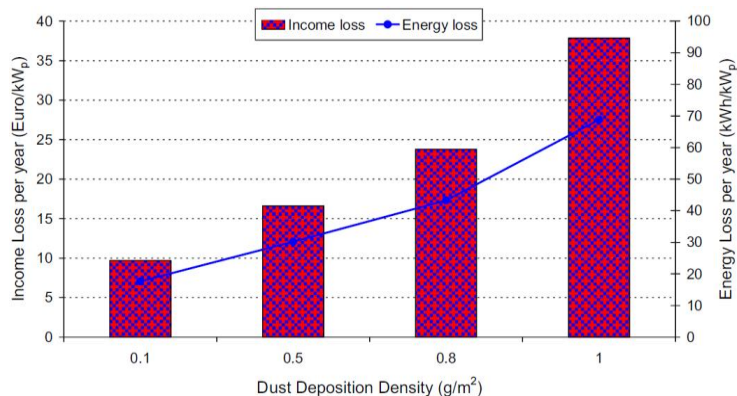


Figure 1-3: Annual income and energy loss as a function of mean dust deposition densities on PV panels' surfaces [3].

1.4 Project Motivation

With the growth of the South African solar industry, many questions and uncertainties also arise about this industry. While dust pollution and its effect have been investigated and documented in other parts of the world, it is worth noting that no documentation on this subject done in southern Africa was found. However, as cited earlier, the effect of dust pollution depends heavily on the geographic location.

A sudden drop in the panel's or array's power production can be due to several factors, including amongst others, cloud cover, tree shading or a sandstorm clouding the panels with dust. Without proper monitoring tools, the exact cause(s) cannot always be easily determined. Even harder to detect or determine is the decrease in panels' output due to gradual accumulation of dirt on its surface over a long period of time. That is one of the serious concerns that this project intends to address.

Some places or sites are more prone to dust pollution than others and might not be suitable for solar parks or they may demand frequent cleaning as a result. The cleaning frequency, method and resources required are the other decisions that cannot always be easily made without proper monitoring.

On the other hand, some PV plants are too large to perform visual inspection on all panels. Some are located in remote areas and it might not always be practical to access the site frequently to attest the performance, however losing even just few watts per module daily can have serious financial consequences.

PV plant operators and planners are always faced with the aforesaid uncertainties. A monitoring station has been designed and developed in this project as a tool to address some of the problems and challenges discussed above.

The station is primarily designed for research purposes to monitor and evaluate long term effects of dust pollution on the performance of solar panels in different parts of South Africa. It aims to create awareness around the issue of dust pollution regarding its effects on productivity and maintenance consequences. It also facilitates easy documentation of dust pollution as well as forecasting its future influence and expected losses. The station will also be helpful in identifying the factors that contribute to dust pollution.

Furthermore, the station is expected to contribute positively in different stages of the PV project cycle. During planning and feasibility study stages, the station can be utilised to provide and assess pollution data for a particular site of interest. The suitability of the site can then be determined in combination with other relevant factors. This data could particularly be vital for large PV plants. Considering the impact of pollution when forecasting power production would lead to more accurate calculations of expected yields, revenue to be generated and eventually payback periods.

Furthermore, the data from the station can also be used during the operation stage to decide on the frequency of cleaning as well as the cleaning resources needed. Cleaning PV panels in large plants may require a significant volume of water, time, energy and labour depending on the cleaning method. It is therefore cost effective to clean only when necessary.

The overall objective was to develop an easy to install, easy to use, cost-effective but reliable platform that will serve to provide long-term data on the effects of dust pollution on PV panels, thereby allowing data-based conclusions and decisions. The station will provide PV plant operators with more control over the issue of dust pollution.

1.5 Project Description

This project entails the design and development of a standalone station capable of monitoring long-term effect of dust pollution on the performance of PV panels. The station is capable of operating the panels at Maximum Power Point (MPP) at any time. It measures and records the operating characteristics (currents and voltages) of the panels and avail the data through the Control System to the operator or researcher for analysis.

The key part of the project is the design and development of two intelligent devices; the Maximum Power Point Tracker (MPPT) battery charger and the Active Load. These devices were designed, fabricated and tested. After testing individual devices, the entire station was assembled and tested. See Chapter 2 for the detailed overview of the project and its main components as well as their respective roles.

Designs and testing of the devices were carried out in the Energy Conversion Lab at the University of Stellenbosch.

1.6 Thesis Structure

This thesis consists of 8 chapters and below is the breakdown of what is deliberated in each one of them.

Chapter 2: This chapter provides detailed overview of the stations fundamental devices and their respective roles. Reasons supporting the selected approach to the problem and all preliminary choices are also explained here.

Chapter 3: In this chapter, a review of literature on the Solar PV industry is discussed, particularly on the subject of dust pollution. Further, solar cells principle of operation is discussed to help understand how dust pollution influences its power generation process.

The operations and design theory of DC-DC converters as fundamental components for the MPPTs and the Active Load are also presented.

This chapter continues with the analysis of the published investigations and their methodologies on the effects of dust pollution on performance of PV panels. Proposed mitigation measures to this phenomenon are also explored.

Design choices and major component selections are analysed for the MPPT battery charger and the Active Load. MPPT algorithms, their implementation and data acquisition methods are also investigated here.

Finally, existing solar PV cleaning mechanisms are compared based on their effectiveness, cost and implementation challenges.

Chapter 4: This chapter concentrates on the design process of the MPPT battery charger from schematics to Printed Circuit Boards (PCB) fabrication and testing. Fundamental design choices and component selections are explained.

The development of the software for the MPPT battery charger and its testing are also documented here. Finally, the test results of the MPPT battery charger are presented and discussed.

Chapter 5: In this chapter, the Active Load design process is documented. Its theory of operation is explained. Design choices (hardware and software) are presented and elaborated.

Testing results and the effectiveness of the Active Load are explained and the conclusions are given.

Chapter 6: This chapter presents the assembling of the different components of the station into a functioning unit. The architecture and coordination of all the devices of the station are further explained.

Chapter 7: The performance of the station is analysed based on its initial design goals. Commissioning results of the station are discussed and interpreted here. Design challenges and limitations are also addressed.

Chapter 8: Ultimately, project conclusions are presented and recommendations are made on how this monitoring station and further studies in this area can be enhanced to overcome the encountered and future challenges.

CHAPTER 2 HIGH-LEVEL PROJECT OVERVIEW

2.1 Overview

The aim of this chapter is to provide a detailed insight of the fundamental components of the station and their respective roles. This chapter also explains the reasons behind the preliminary choices and decisions taken leading to the final architecture of the station.

2.2 The Station Structure

The station is comprised of two identical solar panels, a Maximum Power Point Tracking (MPPT) battery charger, two Active Loads, a battery bank, and a Control System; all interconnected in a manner shown in Figure 2-1. The functions of each of the devices are discussed in the next sections.

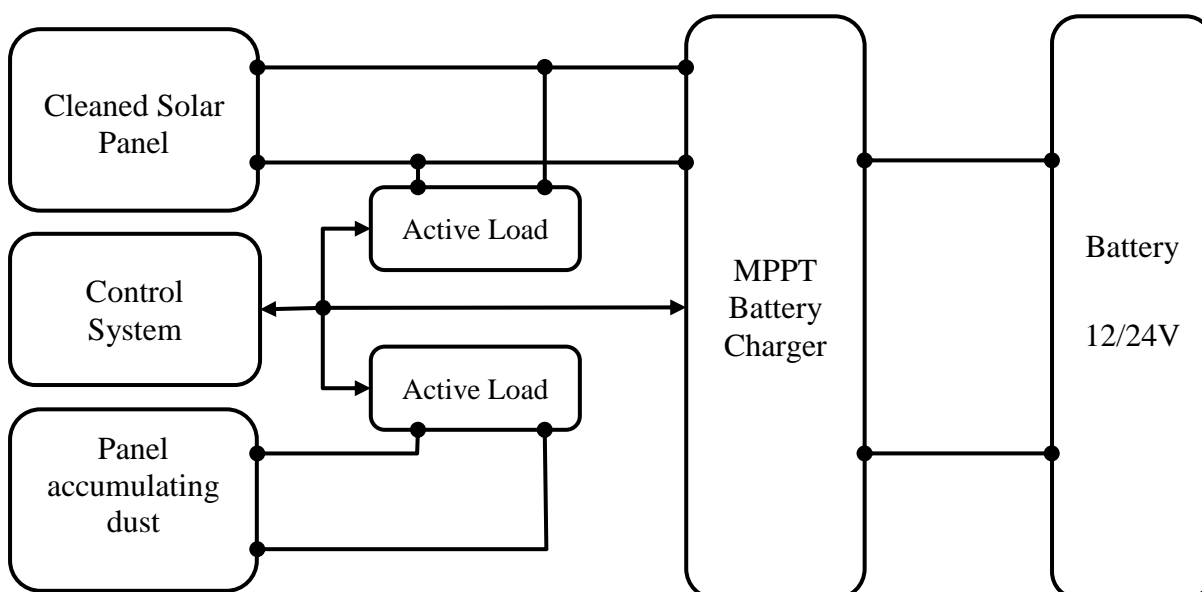


Figure 2-1: Structure of the station's components.

The power generated by the cleaned solar panel at any instant can either be used for battery charging through the MPPT battery charger or be dumped through the Active Loads while the power generated by the other panel is always dumped through the Active Load. Both the MPPT battery charger and Active Load are capable of measuring the operating conditions of

the connected panel. The measured data is either stored internally or sent to the Control System by request; for storage, analysis and for control purposes.

The first panel is the cleaned panel which is kept clean always through scheduled cleaning cycles. The cleaning time and frequency are determined accordingly. The second panel is the reference panel. This panel is allowed to accumulate dust under normal conditions for the particular period of investigation.

Apart from measuring the panels' terminal conditions, both the MPPT battery charger and the Active Load are capable of operating the solar panels at their maximum power points. This capability enables the station to determine the maximum amount of power available at any specific time. It is also important that the panels are monitored under their normal operating conditions.

By analysing the output powers or $I - V$ curves of the two identical panels, the power losses due to dust accumulation can be monitored and remedial actions can be taken or proposed.

2.3 Preliminary Choices and Decisions

After deciding on the architecture of the station, it is time to select the specific types and sizes of the major components. The decisions on whether to design or employ off-the-shelf devices are also investigated here.

2.3.1 The Solar Panels

The two solar panels to be used must be identical - same manufacturer, same technology and same power rating. The size of the solar panels is decided based on their power ratings such that they are compatible with both the MPPT battery charger and the Active Load. The panels are selected such that the combination of their open circuit voltage and short circuit current do not exceed the rated voltage and current of the station's devices (100V, 5A or 50V, 10A).

The solar panels used for the prototype are polycrystalline type manufactured by Solairedirect Technologies and their characteristics are shown in Table 2-1.

Table 2-1: Characteristics of the solar panels at Standard Test Conditions (STC).

Open Circuit Voltage (V_{oc})	Short Circuit Current (I_{sc})	Maximum Power Voltage (V_{MP})	Maximum Power Current (I_{MP})	Maximum Power Point (P_{MPP})
37.0V	8.66A	30.0V	8.0A	240.0W

2.3.2 The MPPT Battery Charger

The main function of the MPPT battery charger is to operate the panels at MPP while charging the battery. As mentioned earlier, the MPPT battery charger also has the capability to record and transmit the panels' operating characteristics to the operator when necessary.

By using the MPPT battery charger, the batteries can be charged much faster as compared to conventional charging methods of connecting panels directly to the battery or using normal regulators. A decision was made to design and develop an MPPT battery charger for this project as opposed to employing commercial MPPTs. This was necessitated by the fact that a research-oriented system is expected to be customisable as well as to operate and deliver over a wide range of operating conditions.

To the contrary, most commercial MPPTs are not customisable while some have no communication capabilities and they may not be reprogrammable. As such the operator cannot modify it and does not have control over its operating conditions. Mainly due to those deficiencies, a multifunction, research-focused, and fully customisable MPPT battery charger has been designed and developed for this project.

The theory of operation of the MPPT battery charger is discussed in section 3.4, while its design and testing are addressed in Chapter 4.

2.3.3 Active Load

To have the capability to always operate the panels at MPP while ensuring that all the power generated by the solar panels is consumed, a smart load has to be employed. An Active Load was designed and developed for this project. The Active Load keeps the panel(s) operating at MPP by dumping the generated power through a dumping resistor.

The Active Load was designed based on the principle of operation of DC-DC converters for power control as discussed in detail in section 5.2.

The other option considered was to dump power by operating MOSFETs in their linear region as proposed by Frey et al. [4]. This option can achieve higher power dumping with minimal component count and it entirely eliminates the need for a dumping resistor. However, it poses several implementation challenges for this application as explained below and it was thus ruled out.

First, this option is not suitable for outdoor implementation since its heat dissipating components demand artificial cooling. Second, since heat is dissipated by the MOSFETs themselves, they must certainly be housed inside a weatherproof enclosure; which makes thermal management more complicated. To implement both weatherproof protection and forced cooling becomes a daunting task. Third, operating MOSFETs in their linear region subjects them to high thermal stress due to the simultaneous occurrence of high drain voltage and current which leads to high power dissipation. However, when the thermo-electrical stress reaches a critical limit, thermal hotspots may occur in the silicon leading to the failure of the MOSFET .

On the other hand, the selected option is implemented with natural cooling since the heat dissipating component does not need weatherproof protection and is therefore housed outside of the component enclosure. That makes this option more suitable for this outdoor application.

The design parameters of the Active Load were also selected to make it compatible with a wide range of commercial solar panels. Detailed information on the theory of operation, design and testing of the Active Load is provided in Chapter 5.

2.3.4 Communication

The main role of this station is to provide accurate data effectively. Consequently, efficient communication as well as compatibility and coordination between several devices of the station are very important. The physical communication layout between the devices of the station is achieved through the RS485 standard interface which guarantees secure and accurate data transmission over distances up to 1200 m, while the popular and efficient Modbus Protocol was implemented as the software standard of communication.

Modbus Protocol provides a simple platform for establishing master/slave communication between several intelligent devices. This protocol was preferred because it is open-source and

is widely used in most industries. Additionally, Modbus Protocol has suitable error checking and handling capabilities. See the Modbus Implementation Guide [5] for detailed guidance.

2.3.5 The Microcontroller

The choice of a microcontroller for both devices was mainly influenced by application needs; program and data memory, resolution, maximum clock speed, number of General Purpose Input/Output (GPIO) pins and internal peripherals like PWM, USART, SPI, etc. Community based support, ease of programming, Integrated Development Environment (IDE), power consumption, and costs were also important factors that were considered.

Eventually, Atmel's AVR ATmega328 was selected. These series of microcontrollers have a brilliant community based support, free compilers and IDE, many useful peripherals, and inexpensive ISP programmers.

2.3.6 Programming

Both the software of the MPPT battery charger and Active Load were developed in C language because the compilers are readily available. On the other hand, C is a rich and powerful programming language but also easy to understand. The C language is one of the most dominant languages in embedded microcontroller programming because it is compatible with most of the microcontroller families.

Programming is done in-system (in-circuit) for both devices. This allows for the devices to be fully reprogrammable.

2.3.7 The Control System

The functionality of the entire station revolves around a Control System. The Control System coordinates all the functions of the station including switching devices ON and OFF, data logging and battery charging. It also initiates all the communications.

The Control System also serves as the communication interface between the operator and other devices of the station. The role of the Control System can be played by a normal PC. However, due to its small size, low power consumption, easy portability and superior capabilities, the Raspberry Pi was found to be more suitable for remote and standalone application. The BeagleBone Black was also considered but it was ruled out because of its long delivery period to South Africa whereas the Raspberry Pi was readily available.

2.3.8 Cleaning Mechanism

For the prototype, manual cleaning is implemented due to several reasons. First, manual cleaning is quite effective, and is not labour-intensive in this scenario (only one or two panels to clean at a time). Second, the prototype needs constant visual monitoring such that if there is any flaw in the station's operation, it can be detected early enough.

Automatic cleaning mechanism is recommended for autonomous operation; monitoring in remote areas and areas where ease of access is not always possible.

2.3.9 Batteries

The batteries are the primary power source for all the devices of the station. All the devices are designed or selected to be compatible with both 12V and 24V batteries as their power supply.

The choice of the batteries primarily depends on the voltage rating, capacity, as well as on the charging and discharging characteristics.

Deep Cycle batteries were selected because they can withstand deep discharge cycles without internal damage. Additionally, they are able to withstand a certain magnitude of ripple current, although measures to reduce their exposure to ripple currents have been implemented in the hardware design of the MPPT battery charger.

Two FB International batteries (HGL 12-12) are used for the prototype. Their rated voltage is 12 V and each has a capacity of 12 Ah.

CHAPTER 3 THEORY AND LITERATURE REVIEW

3.1 Overview

This chapter provides insight and theoretical analysis of all the major components used in the design and development of the monitoring station.

A typical stand-alone solar PV system is normally comprised of the following elements: energy generator (solar cell, module or array), charge controller or MPPT, storage (battery) and the load (consumer). Some installations might also have an inverter to convert the generated Direct Current (DC) into Alternating Current (AC) for compatibility with most loads or for integration into the grid in case of grid-connected systems.

The overall efficiency of the solar PV system is a sum of the efficiencies of all the elements in the source-to-load chain. To ensure that the load receives the maximum available power, the efficiencies of all the components in the source-to-load chain must be optimised. The power losses have to be minimised as much as practically possible.

For that purpose, the theories of operation and optimisation possibilities of those components are therefore analysed.

3.2 The Solar Cell

A solar cell is the elementary component of any PV system in existence. As such, to fully comprehend the operations of solar panels we have to start from the basics, the solar cell.

Solar cells are made from two layers of semiconducting materials. Different materials are used to produce solar cells and the research on new and more efficient materials is ongoing. Most solar cells in the market today are made from silicon (Si); an element which is readily available and abundant in the earth's crust. There are also solar cells made from compound materials. The efficiency, availability and cost of raw materials as well as the manufacturing process dictate the market price and popularity of the specific type of solar cell.

The output voltage of one silicon solar cell is normally in the range of 0.5-0.6 V, which is insufficient for virtually any useful application. For that reason, multiple solar cells are usually connected in series and parallel arrangements to achieve a specific voltage and current outputs which forms a panel, also known as a module. Modules are in turn connected in series and parallel arrangements to form arrays of specific currents and voltages as discussed later in this chapter.

3.2.1 Operating Principle

Solar cells are formed when two oppositely doped semiconducting materials are connected back to back as indicated in Figure 3-1. Doping of semiconducting materials is a chemical process of adding impurities to an element, such that the result is either a majority or minority carrier, i.e. to either contain a surplus of positive charge carriers (p-layer) or surplus of negative charge carriers (n-layer). The two oppositely doped semiconductor layers are then connected together to form a p-n junction of the solar cell, to which positive and negative conducting leads are added.

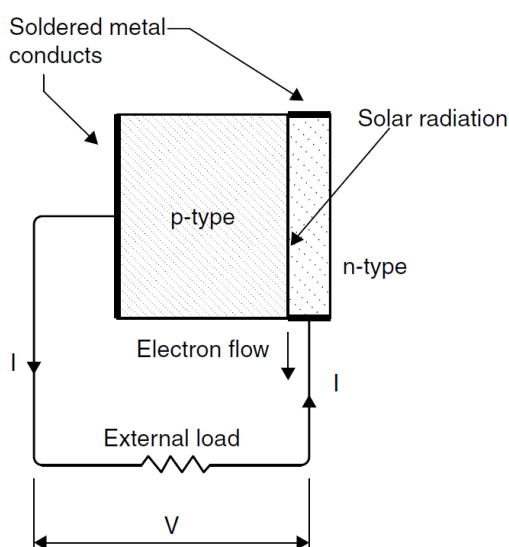


Figure 3-1: Principle of Solar Cell operation [6].

The solar PV power generation process is explained in brief in the next paragraphs.

Semiconducting materials have an energy band (forbidden band) between the valence band and the conduction band. A valence band is the energy level in which electrons are tied to the nucleus of the host atom and as such they cannot move freely, while the conduction band is

the energy level in which the electrons are released from the nucleus of the host atom and can thus roam freely.

When the sun shines, it emits radiant energy in small units called photons. When a photon penetrates into the n-layer semiconducting material, it increases the energy of the electron that has absorbed it. The energy of the electron increases just enough (equal to band-gap energy) to enable it to cross to the conduction band and electron-hole pairs are created.

It is this migration of the electron-hole pairs across the p-n junction that causes the current to flow when a circuit is closed. The current will continue flowing for as long as incident photons with sufficient energy are being absorbed by the solar cell. The physics of semiconductors and photovoltaic effect is well documented by both Kalogirou [6] and Masters [7]. The effect of dust pollution on this process of power generation is discussed later in this chapter.

3.2.2 Equivalent Circuit

The equivalent circuit is necessary for modelling, analysis and simulations of solar cells. There are several models of the solar cell equivalent circuit. These equivalent circuits vary in terms of accuracy or complexity depending on the parameters included.

Figure 3-2 shows a general model of an arbitrary solar cell. It consists of a photocurrent source (I_{ph}), a diode, a shunt resistor (R_{sh}) indicating a leakage current, and a series resistor (R_s) representing an internal resistance due to the flow of current. The output current is expressed according to Kirchhoff's Current Law (KCL) as the difference of the photocurrent and the diode current (I_D):

$$I = I_{ph} - I_D - \frac{V}{R_{sh}} \quad (3-1)$$

The solar cell can also be modelled only as a current source in parallel with a diode i.e. without leakage and internal losses ($R_{sh} = \infty$) and $R_s = 0$. That results in the simplest equivalent circuit of a solar cell, however that would be an ideal cell. Such a model can only be used for applications where high modelling accuracy is not desired.

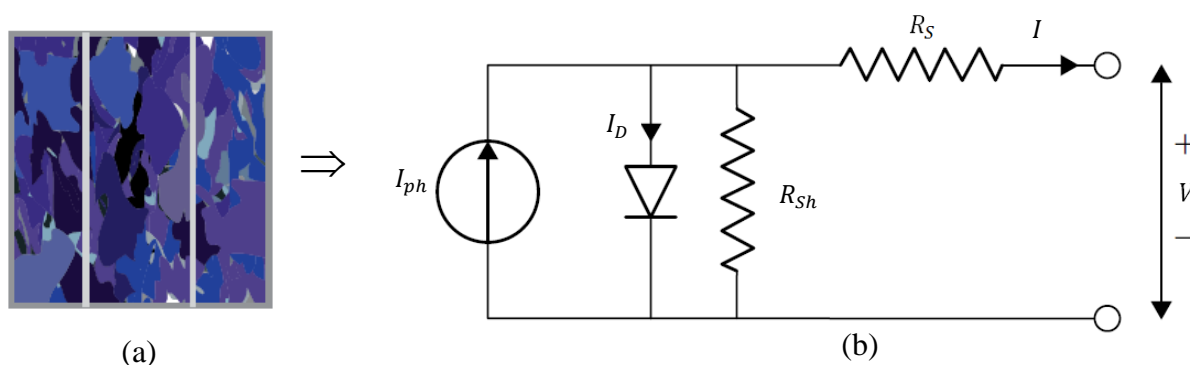


Figure 3-2: (a) Solar Cell image (Source: EPIA) (b) Solar Cell equivalent circuit [6].

3.2.3 The I-V Curve

The I - V curve of a solar cell is a graph derived primarily from its open- and short-circuit characteristics. The current and voltage of a solar cell vary every instant depending on its intrinsic properties, temperature, and on the amount of solar radiation that the cell is receiving at that specific moment.

At a particular irradiance and temperature, the highest PV current is obtained when the cell terminals are short-circuited such that the voltage across them is zero. This current is called the short-circuit current, I_{SC} , of the cell. On the other hand, the highest voltage is obtained when the circuit of the solar cell is open, such that no current is flowing through it. This is the open-circuit voltage of the cell, V_{OC} , at that specific irradiance.

The maximum (rated) power can be determined by varying the load connected on the solar cell terminals and plot the results as indicated in Figure 3-3. For a certain atmospheric condition, there is a specific optimum load resistance that results in the maximum power output. This power is known as the maximum or peak power and the solar modules are rated at this power, $P_{R(max)} = V_R I_R$, under the Standard Test Conditions (STC).

The solar cell is most efficient when operated at the maximum power point [7]. The maximum efficiency is expressed as the ratio of the maximum power (P_{max}) to the irradiance falling on the cell of area A (m^2).

$$\eta = \frac{P_{max}}{P_{in}} = \frac{V_R I_R}{A G_a} \quad (3-2)$$

In equation (3-2), G_a is the irradiance (W/m^2).

Another important parameter used to define the performance of a solar cell is the Fill Factor (FF), which is a ratio of the shaded rectangle ($V_R I_R$) to the rectangle $V_{OC} I_{SC}$ in Figure 3-3.

$$FF = \frac{P_{max}}{V_{OC} I_{SC}} = \frac{V_R I_R}{V_{OC} I_{SC}} \quad (3-3)$$

The value of the Fill Factor is usually used to determine the quality of a particular solar cell. Solar cells with Fill Factors greater than 0.7 are regarded higher in terms of quality.

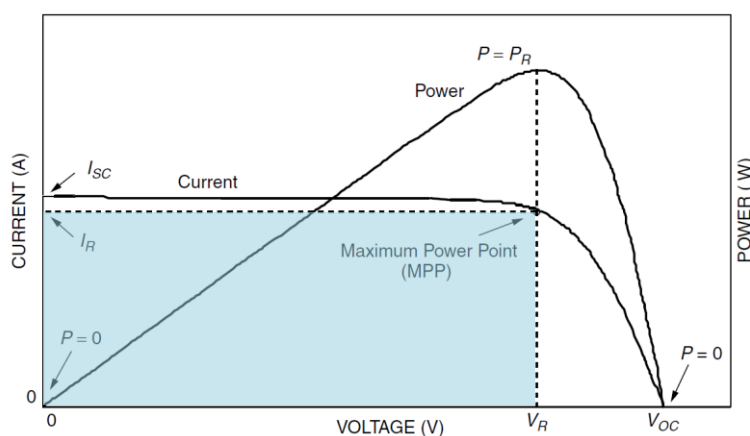


Figure 3-3: The $I-V$ curve and power output for a PV module [7].

3.3 Dust Pollution and PV Performance

It was revealed in Chapter 1 that dust pollution affects the performance and overall yield of solar panels. The influence of dust pollution on the effectiveness of the panel's power generation capabilities can be classified in multiple ways. The effects discussed below have been investigated by Fali et al. .

- 1. Blocking Solar Radiation.** It was established that dust particles in the air or on the glass cover of the solar panel reduce the number of photons that reach and can be absorbed by the solar cells. The dust particles also weaken some of the absorbed photons by absorbing a portion of its energy before it reaches the solar cell. In dusty areas, sand storms can greatly reduce energy absorption of PV arrays at an instant.

2. **Increase in Temperature.** Dust on the surface of the panel absorbs some of the energy from the solar radiation and convert it to heat. This heat contributes to the increase in surface temperature of the panel which eventually results in lower efficiency of the solar cells due to their Positive Temperature Coefficient (PTC) resistance characteristics.
3. **Surface Damage.** Prolonged accumulation of dust and other dirt on the surface of the panel, coupled with humid conditions can result in the degradation or corrosion of the panel's glass cover. Such deterioration results in lower sunlight absorption capabilities even after the panels have been cleaned. Although most panels are designed to survive severe weather conditions, chemical processes may still damage their surface causing permanent or semi-permanent defects.

The abovementioned factors and their effects on PV panels' performance are thoroughly discussed by Fali et al. [8].

3.3.1 Effect of Depositions

As deliberated in section 1.3, dust pollution or bird droppings on the surface of the panel reduce power output by blocking solar radiation from the solar cell forming semi-permanent shading. This effect will be discussed in detail under this section as shading from depositions.

To understand the effects of depositions properly, it is essential to first zoom into the arrangement and connectivity of solar cells inside the solar panel or module.

Solar cells inside a panel or module are normally connected in series forming strings to achieve a practically usable voltage. Because of this particular arrangement of cells, shading from depositions leads to several negative impacts on the output of a PV module. Even if only one cell is covered, the performance of the whole panel is affected.

Semi-permanent shading will reduce the power output of the affected solar cell in the ways outlined below.

First, depositions block the solar radiation absorbed by that specific solar cell which results in that cell generating less power [9].

Secondly, they increase internal losses of the covered cell. This effect is greater in series string because the current produced by the cells that are not covered, must flow through all the cells including the defective one. But a cell with depositions on its surface will have a higher resistance and it will act as a resistor in the path of currents produced by the cells that are not affected. The shaded cell will eventually overheat as shown in Figure 3-4 and it might be damaged permanently [10].

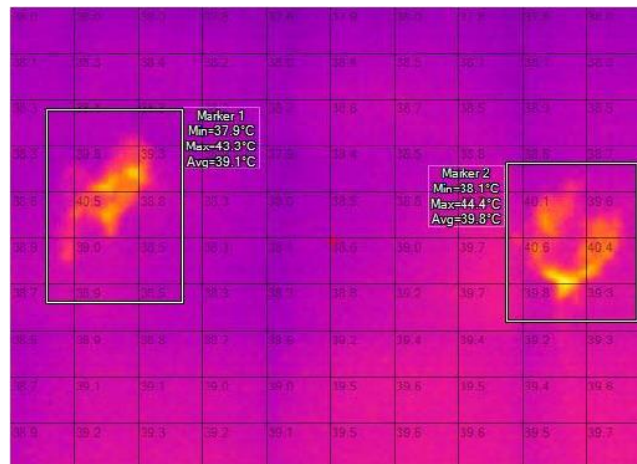


Figure 3-4: Image showing increase of temperature in the area with depositions [10].

For that reason, external anti-parallel diodes are normally included in parallel with each PV panel to reduce the impacts of shading in the array as shown in Figure 3-5.

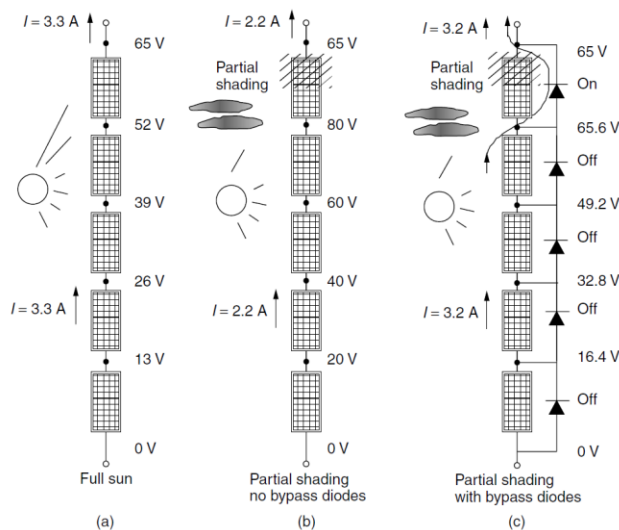


Figure 3-5: Effect of partial shading with and without bypass diodes [7].

When a shaded panel starts to generate smaller current compared to other panels in the same string, the bypass diode will turn on and provide an alternative path for the load current and thereby avoiding the shaded panel.

3.3.2 Effect of Humidity and Rain

Humidity in this context refers to the percentage of water vapour in the air. The effect of humidity can be analysed in three categories.

First, the dispersion effect (reflection, refraction and diffraction) of water vapour particles in the atmosphere on the irradiance reaching the solar cell. Second is the formation of water droplets (condensation) on the panel's surface. Third and last, is how the amount of water vapour in the air affects the weight and concentration of airborne particulates.

A relationship between irradiance and relative humidity has been investigated by Gwandu and Creasey [11] as illustrated in Figure 3-6.

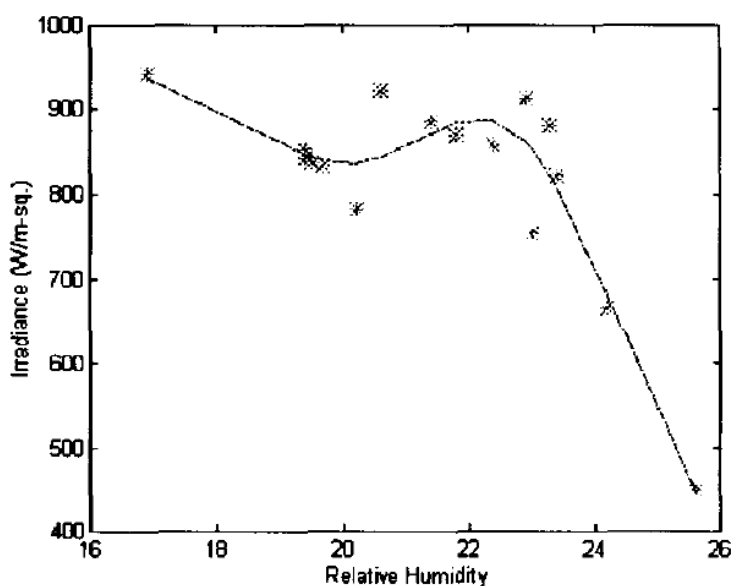


Figure 3-6: Relationship between irradiance and relative humidity [11].

Gwandu and Creasey carried out a study in the humid tropical region of Nigeria, and they convincingly concluded that humidity does affect irradiance levels. Their study outcomes revealed a non-linear variation of the module open-circuit voltage to humidity while the short-circuit current showed a linear dependence.

Moon [2] found that rainfall helps to wash away most dirt on the surface of tilted panels, but normally leaving some dust accumulated in the corners of the solar panel's frame. Rain was however not found to have a noticeable effect on the panels in a horizontal position (not tilted).

Fali et al. have concluded that the impact of rain on dust accumulation also depends on its intensity; the heavier the rain, the more the dust that is washed away. They also noticed that while heavy rain helps to clean the solar panels, light rain on the other hand leads to the formation of dust spots and helps the dust coatings to stick firmly on the panel's surface thereby making it hard to be blown off by wind .

3.3.3 Effect of Wind

Panels in operation are always exposed to wind blowing in various directions and at different speeds. Wind acts as a carrier of dust particles and other airborne particulates and it directly affects the concentration and suspension of these objects in the atmosphere. This means that wind can have a substantial effect on the accumulation of dust on the surface of solar panels. Depending on its speed and direction, the wind can either aid dust to settle on the panel's surface or blow it off.

Goossens and Van Kerschaever have established that wind velocity is an important factor on solar PV performance, as higher power drops were experienced with the increase in wind speed because the layout and structure of the dust coating on the cells depends, amongst others factors, on wind speed.

The effect of wind was also investigated by Fali et al. [8], and it was found to influence the effectiveness of rain as it changes the angle by which the rain drops are falling on the panel's surface. Under no or low wind conditions, rainwater falls vertically, close to 90 degrees to the ground. Under strong winds, that angle is less and it was found to affect the quantity of dust that is washed off the panels' surface.

3.3.4 Effect of Tilt Angle

The effect of tilt angle on the accumulation of dust was investigated by Cano [12] who concluded that as the tilt angle of the solar panel becomes increasingly horizontal, the soiling effect increases. Energy losses of 1% to 4% due to soiling were recorded for horizontal solar

panels. Soiling effect was observed at all tilt angles, but as can be seen in Figure 3-7, the flatter the solar panel, the more the soiling effect. This conclusion can be attributed to the fact that gravity supports the process of dust removal while its effect lessens as the tilt angle decreases.

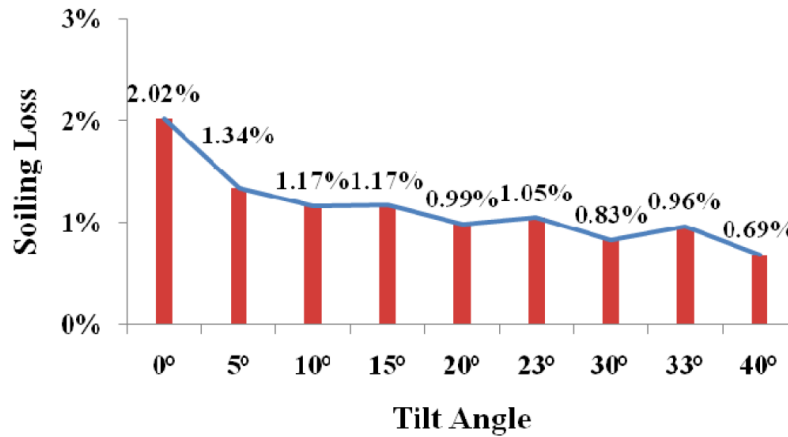


Figure 3-7: Soiling losses at different tilt angles [12].

It is important to also note that the tilt angle affects the influence of rainfall and wind on dust accumulation.

3.4 Maximum Power Point Tracking (MPPT) Battery Charger

As shown in Figure 3-8, the relationship between voltage and current of a solar cell is non-linear.

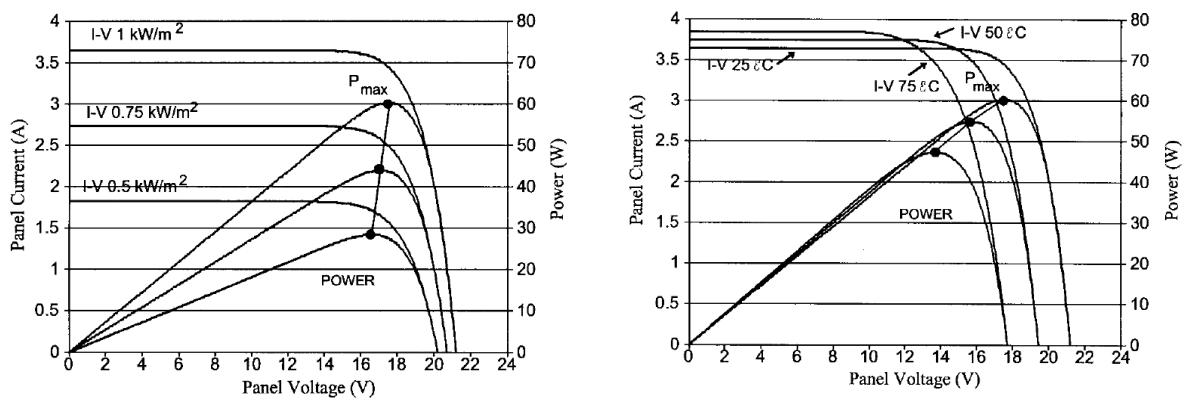


Figure 3-8: Irradiance and temperature dependence characteristics [13].

This means that, at any given time there is an operating point on the I - V curve where voltage and current of the solar panel results in the maximum possible power being delivered to the load. This is the Maximum Power Point (MPP), which is not static but changes over a wide range with the irradiance and temperature [13].

The MPP is also affected by the aging of the panel, shading and other atmospheric conditions. It can be seen from Figure 3-8, that temperature greatly affects the panel's voltage while irradiance changes mainly affect the panel's operating current.

The MPPT battery charger ensures that a solar panel is always operating at its MPP and that the maximum amount of power available is always delivered to the battery. It achieves its function by manipulating the terminal conditions of the solar panel and modulating the output voltage and current to match the characteristics that are optimal for the connected battery.

The fundamental element of the MPPT battery charger is a DC-DC switch-mode converter, mostly employing Pulse Width Modulation (PWM) control and algorithms to track the MPP instantaneously. The algorithms for MPP tracking are discussed in detail in section 3.4.6.

3.4.1 Analysis of DC-DC Converters

The DC-DC converters used in MPPTs belong to a big family of power electronic Switch Mode Power Supplies (SMPS) with PWM control. The DC-DC converter supplies a regulated DC output voltage to a load from a variable DC input voltage as illustrated in Figure 3-9 below.

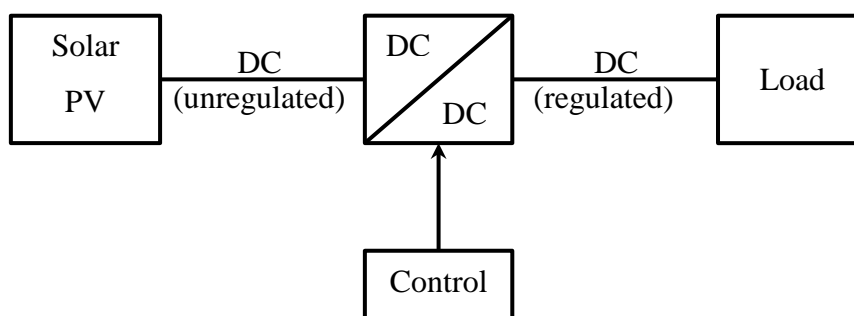


Figure 3-9: Basic MPPT System.

The difference between the input and output power of the MPPT depends only on its conversion efficiency.

Various MPPT converter topologies have been discussed and proposed in [13], [14] and [15]. Based on application requirements, converters in MPPTs are employed to either step down (Buck) or step up (Boost) unregulated DC input voltage into a DC output voltage with the desired magnitude. There are also converter topologies that provide both step down and step up (Buck-Boost) functionalities.

In this project, the required output voltage is less than the input voltage, therefore a buck converter is used and only its operation is discussed further.

A buck converter gained such a name because it outputs a bucked or chopped voltage i.e. the average output voltage (V_{out}) has a lower magnitude than the input voltage (V_{in}). The advantages of this converter are simplicity and low cost [14], as well as higher conversion efficiency [15].

A basic buck converter and its switching waveforms are shown in Figure 3-10.

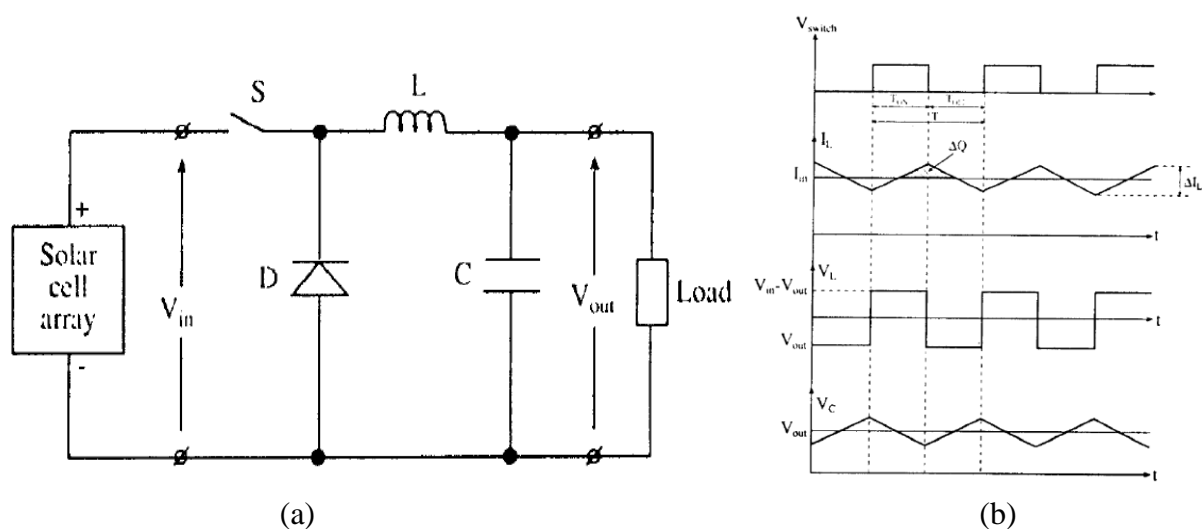


Figure 3-10: (a) Buck Converter and (b) its Switching waveforms [15].

The main components of a buck converter are the switch (S), inductor (L), freewheeling diode (D) or switch (for synchronous converters), and input as well as output filtering capacitors (C_{in} and C_{out}).

The output voltage of a buck converter is expressed by the following equation:

$$V_{out} = DV_{in} \quad (3-4)$$

Where D is the duty cycle ($0 < D < 1$) i.e. the ratio of the time for which the switch is ON (T_{on}) to the switching time period, T .

$$D = T_{on} / T \quad (3-5)$$

$$T = T_{on} + T_{off} \quad (3-6)$$

3.4.2 The Switch

The switch is normally a power semiconductor device (MOSFET, BJT or IGBT). It is called an active switch since its state is determined by the PWM signal that is applied to its control terminal.

The switching device must be capable of fast switching and must carry out its functions with minimum conduction losses [16]. It must be selected such that it safely conducts load current continuously and block OFF-state voltage without damage.

Another crucial aspect for the switching device is thermal management to avoid exceeding the allowed operating temperature.

Power MOSFETs are popular with applications operating at higher frequencies but lower voltages whereas for voltages above 500V and lower frequencies, IGBTs are preferable [14].

The operating frequency is normally selected based on the type of switching device and efficiency requirements. The switching frequency affects the physical sizes and values of most converter components, especially capacitors and inductors. For example, for the same ripple current requirements, the inductance required at 1 MHz is twice less than what would be required at 500 KHz . Higher operating frequency reduces significantly the overall physical size of the converter. However, too high frequency can also result in higher magnetic losses in the inductor core and high switching losses in the switching devices.

Due to the PTC of the MOSFET's on-state resistance, conduction losses can be reduced by connecting the MOSFETs in parallel so that the total current is shared. This in turn benefits the thermal management, since each MOSFET will only now carry a portion of the total current (half, if two MOSFETs are paralleled). As the current conducted by one MOSFET increases, its on-state resistance also increase. On the other hand, the current share of the other MOSFET will reduce and so does its on-state resistance. This current sharing continues automatically since the PTC acts as a slow negative feedback system. As a result, such

behaviour (process) reduces conduction losses and thermal resistance resulting in stabilisation effect or balance of currents and temperature.

Several factors must be considered to ensure successful paralleling of MOSFETs. The first consideration is that the gates of paralleled MOSFETs must not be connected directly to the driver but with a small damping resistor in series with each gate. The gate resistor is meant to curb high frequency oscillations or ringing resulting from stray inductances and gate capacitances and must be close as physically possible to the gate of the respective MOSFET.

Another consideration is that the PCB layout of paralleled MOSFETs must be symmetric to each other.

Lastly, junction temperatures of the paralleled devices must be kept balanced as close as possible. It is therefore advisable for the paralleled switching devices to be mounted on the same heat sink.

3.4.3 The Inductor

The inductor is one of the most critical components in the buck converter. It must be designed or selected to carry maximum load current without saturating and with minimum copper losses while providing the required inductance. Maximum load current dictates the approximate size of the inductor. If the inductor is saturated, the converter efficiency decreases considerably.

Amongst other vital features, inductance value determines the fraction of ripple current in the load current and it also determines if the converter operates in continuous or discontinuous conduction mode (CCM or DCM). In CCM, the inductor current does not attenuate to zero during the switch-OFF time (T_{off}) while in steady state operation.

The minimum inductance value is determined by:

$$L_{min} = \frac{V_{in} - V_{out}}{\Delta i_L} D T_s \quad (3-7)$$

Where Δi_L is the peak-peak inductor ripple current value (A) and, T_s is the switching period in second (s).

3.4.4 Freewheeling Diode

To maintain the continuous flow of current through the load and in the same direction, an alternative current path must be provided when the switching device is turned OFF (switch is open). This function is fulfilled by a freewheeling diode. When the transistor turns OFF, it forces the inductor current to decrease. This results in the inductor voltage becoming sufficiently negative to forward-bias the diode, and the diode starts to conduct. The diode selected for this purpose must be a fast-recovery diode.

Typically, diodes have high forward voltage drop (0.4-0.8V) which results in high conduction losses and eventually lower converter efficiency. This problem can be solved by replacing the diode with a MOSFET resulting in a synchronous converter operation [17]. The synchronous converter implementation poses some complications with switching synchronisation. However, a good dual gate driver with sufficient dead time can handle the switching synchronisation quite easily.

3.4.5 The Capacitors

Together with the inductor, input and output capacitors form a low-pass filter. The capacitors must be large enough to overcome voltage overshoots and ripples generated in the converter during the switching process.

The capacitors also provide a path for ripple current and protect ripple-sensitive loads like batteries. For this reason the selected capacitor must have capacitance large enough such that its impedance at the switching frequency is much smaller than the load impedance [14]. The Input capacitance also reduces sharp variations in the panel voltage. Capacitors must be selected largely based on the value of their equivalent series resistance (ESR), as opposed to their capacitance value [17].

The minimum required output capacitance value is calculated by:

$$C_{out} = \frac{\Delta i_L T_s}{8\Delta v_{out}} \quad (3-8)$$

Where Δv_{out} is the allowed peak-peak voltage ripple (V).

3.4.6 Algorithms

As discussed earlier, the MPP of a PV panel is a dynamic point which changes depending on various factors. Unlike the conventional energy sources where unused energy remains in the source, solar energy that is not harvested is lost. For this reason, MPPTs are used to harvest the maximum energy possible from the PV panel at any instant time. The effectiveness of the MPPT to track the MPP depends enormously on the type of the algorithm (technique or method) employed.

Esrarn and Chapman have discussed and compared 19 algorithms that are widely used in MPPTs, while Dolara et al. comparatively analysed the performance of the seven widely adopted algorithms. The choice of the algorithm is influenced by factors like implementation complexity, tracking accuracy, convergence speed, cost etc. Each algorithm has its merits and deficits, but the final choice must be a compromise between tracking accuracy and implementation costs.

After analysing different algorithms proposed in literature and considering the recommendations made, a Perturb and Observe (P&O) algorithm was chosen. This algorithm was chosen because of its ease of implementation and its decent performance at slight irradiance variations. Only this algorithm will be further discussed. The Perturb and Observe algorithm is based on ‘hill-climbing’ techniques as shown in Figure 3-11.

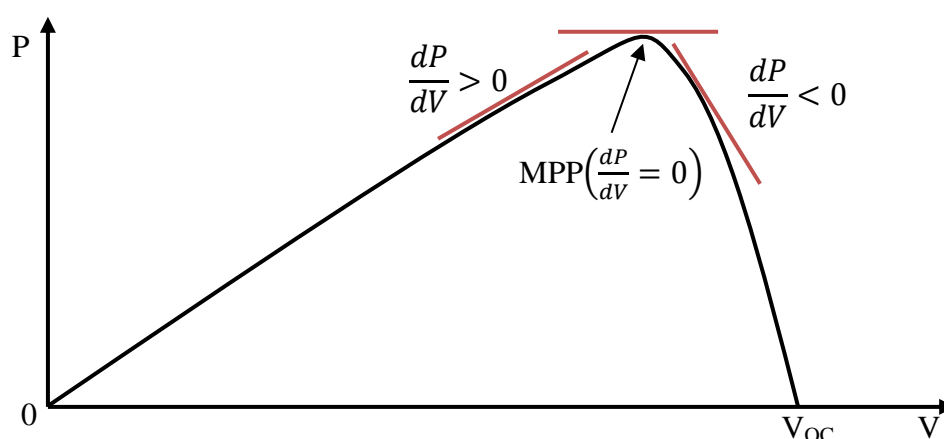


Figure 3-11: Hill-Climbing technique and the sign of the power gradient.

This technique involves periodically perturbing the gradient (dP_{PV}/dV_{PV}), of the power curve and to then observe the direction in which the power is increasing.

The operating voltage of the panel is perturbed such that its power output increases ($dP_{PV}/dV_{PV} > 0$) or decreases ($dP_{PV}/dV_{PV} < 0$). The algorithm uses the sign of the difference between current and previous power to determine whether to move the operating point further in that direction (if power increases) or to move it in the opposite direction (if power decreases). At MPP the gradient of the power curve equals zero ($dP_{PV}/dV_{PV} = 0$), since previous power would be equal to current power.

These steps constitute a perturbation cycle and they are repeated periodically as indicated by the flow diagram in Figure 3-12.

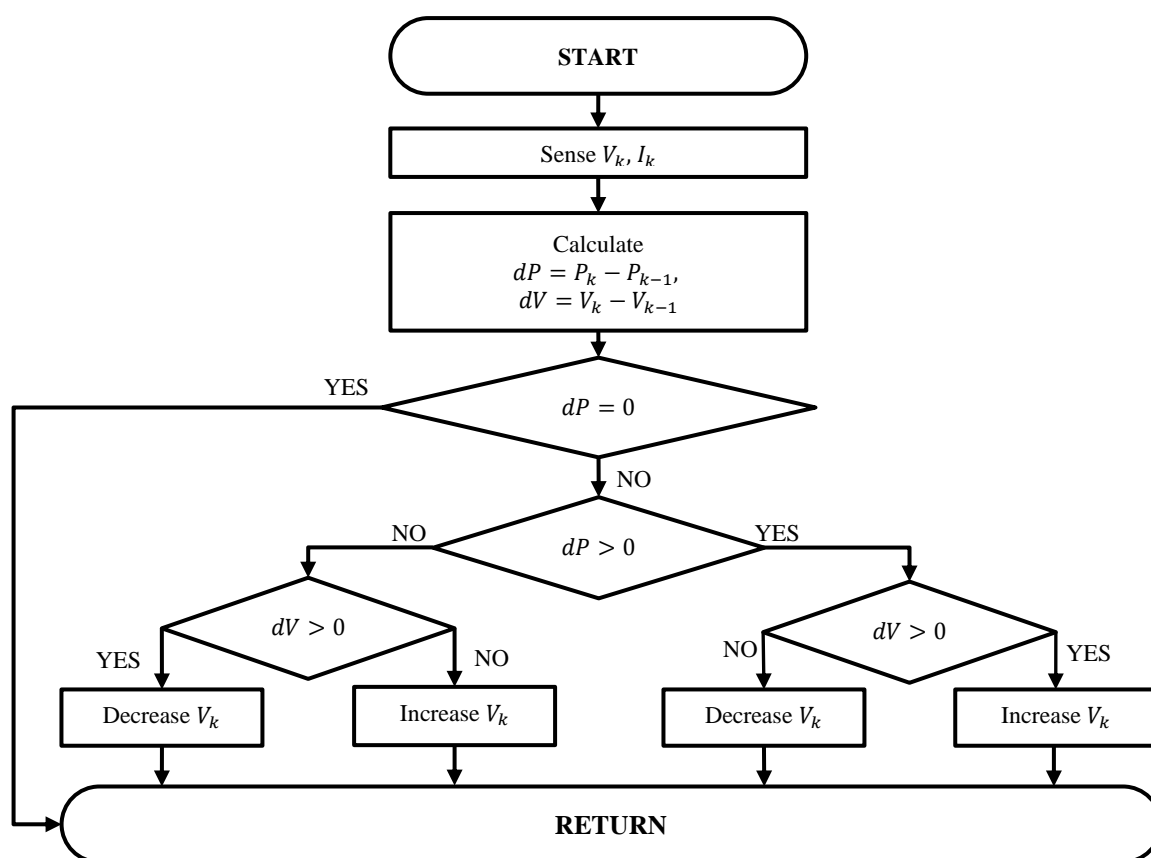


Figure 3-12: Flowchart of the perturbation cycle.

The main weakness of this algorithm is the oscillations around the MPP [18]. The time it takes to reach the MPP depends on the step size (increment or decrement) being used. Small step values reduce oscillations around MPP and therefore reduce power losses, however the algorithm may take longer to reach the MPP. The size of the step is determined during software development. This algorithm also fails to recognise whether the change in the power

is due to its own perturbation or due to the change in irradiance. That makes it hard for this algorithm to trace the MPP under unstable (fast-changing) irradiance conditions.

Optimised P&O algorithms overcoming some of these drawbacks have been proposed in literature. The optimisations however also come with some implementation difficulty. The implementation of this algorithm is discussed in section 4.4.1.

3.5 Measurements

In order to track the MPP, most if not all, algorithms require measurements of either current, voltage or both. This section gives an overview on the current and voltage measurement techniques. Ways of processing signals to reduce noise and to maintain signal quality and accuracy improvement are also looked into.

Typically, a measurement system consists of the three basic elements as indicated in the figure below.

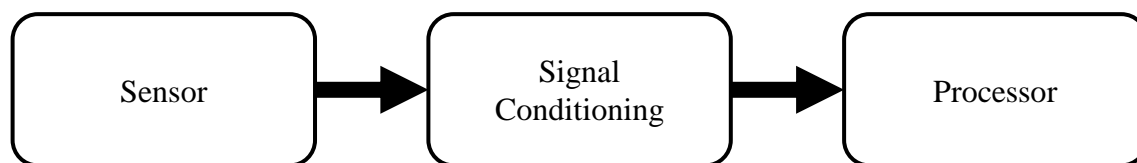


Figure 3-13: Measurement System Overview.

The sensor block consists of the transducer which converts a signal being measured into the desired form and/or level. The signal conditioning involves manipulating the sensed signal to be in the range and quality required. This may include amplification, buffering, filtering, and digitisation. Signal conditioning is discussed in detail in section 3.6. The processor block consists of the control, storage and/or interface devices (microcontroller or digital signal processor (DSP)).

3.5.1 Current Measurement

Current measurement is a fundamental requirement for the MPPT control. The measurement can either be done on the low or high side of the load as shown in Figure 3-14.

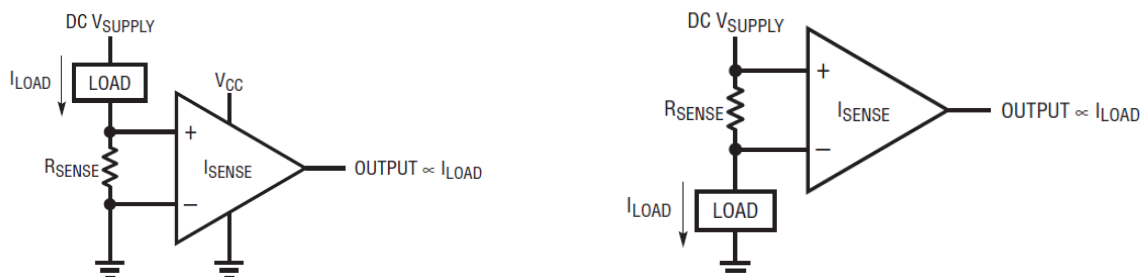


Figure 3-14: Low (left) and high (right) side current measurement [19].

The low side refers to the return path (negative rail) while the high side is the supply path (positive rail). The advantages and disadvantages of each option are analysed in the application notes [19] and [20].

There are a variety of current sensing techniques. The choice of the sensing technique is determined by design requirements and restrictions such as maximum current handling capabilities, accuracy, Printed Circuit Board (PCB) space, efficiency, thermal considerations, and cost.

The following current sensing techniques were considered.

a) Shunt Resistor

This is possibly the most popular technique used for current sensing due to its relative low cost and low power losses, and high reliability. This method employs a low power resistor (R_{shunt}) with a precise value such that the voltage drop (V) across it is directly proportional to the current (I) flowing through it [19].

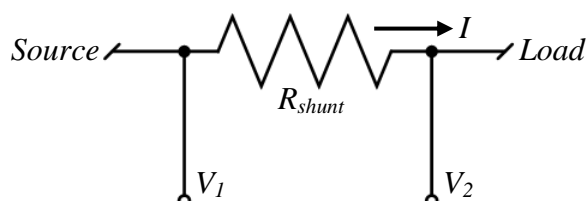


Figure 3-15: Shunt Resistor current sensing technique.

This relationship is expressed mathematically as:

$$V = V_1 - V_2 = I \times R_{shunt} \quad (3-9)$$

The key advantages of this sensing technique are simplicity of implementation, mechanical robustness, low cost and high reliability [21]. Although shunt resistors are manufactured to dissipate as little power as possible and with low temperature coefficients to avoid temperature drift, their accuracy still mainly depend on the precision of their manufacturing.

The main drawback of this technique is that its operation relies entirely on the phenomenon of voltage drop across the shunt resistor which translates into power dissipation (losses) . For high current applications, even low resistances can result in high power dissipation and it can significantly reduce the efficiency of the entire system.

The resistance of the shunt resistor can also be affected by soldering; for instance, too much solder can increase its resistance by a small but significant margin.

The lack of galvanic isolation between the circuit and measurement devices is another vital concern for some applications. Using this technique, leaves measurement devices easily exposed to high voltages and currents.

b) PCB Copper Trace

Due to the desire for very low value resistor to measure high currents, free sensing resistors in the form of PCB copper have been proposed by Ziegler et al. [21] and Spaziani [22]. They concluded that the copper of a PCB can be utilised to sense current, although its implementation has several limitations. The resistance (Ω) of a copper trace as a function of temperature can be determined by:

$$R(T) = \rho(T) \frac{l}{A} \quad (3-10)$$

Where $\rho(T)$ is the temperature dependent resistivity of copper, $\Omega\text{-cm}$, l is the length of the copper trace, cm, and A is the area of the trace, cm^2 ($A = \text{width} \times \text{height}$).

Therefore, equation (3-10) allows a PCB trace to be routed with a specific length and width to result in a specific trace resistance.

Ziegler et al. [21] noted that tolerances due to PCB manufacturing technology can affect the accuracy of this technique. The other factor is that the length-to-width ratio of a PCB resistor can be quite large due to the low resistivity of PCB copper. As a result the sensing resistor may demand a large portion of the PCB space.

c) Hall effect

This sensing technique is based on the knowledge that when current flows through a conductor, it creates a magnetic field around the conductor and its strength (H) is directly proportional to the current (I) magnitude [20]:

$$H = \frac{I}{2\pi r} \quad (3-11)$$

Whereas the magnetic flux density is expressed as:

$$B = \mu_0\mu_r H = \frac{\mu_0\mu_r I}{2\pi r} \quad (3-12)$$

In equation (3-12) the following symbols apply:

$\mu_0 = 4\pi \cdot 10^{-7}$ Vs/Am, is the permeability of vacuum.

μ_r is the permeability of the material.

r is the radial distance from the centre of the conductor.

A magnetic material is placed around the current carrying conductor to capture and concentrate the generated magnetic flux. A Hall Effect IC is then used to measure the concentrated magnetic flux density and it outputs 'Hall voltage' which is directly proportional to the current in the conductor [20] and can therefore be used to measure that specific current.

The main advantages of this technique are galvanic isolation (contactless sensing) of the measuring circuit and zero power losses. Out of the three current measurement techniques discussed, this is the only technique that does not depend on the voltage drop.

Its accuracy however depends on the magnetic sensitivity of the sensor and its intrinsic offset due to temperature. The field concentrator costs and magnetic interferences are also some of the shortcomings associated with this technique.

3.5.2 Voltage Measurement

Voltage measurement is also a requirement for most MPPT algorithms. Unlike current sensing which normally requires conversion of the sensed signal into a different form, voltage sensing is straight forward. Voltage sensing is commonly achieved by means of a resistor ladder that scales the measured voltage signal to an acceptable level (e.g. 0-5 V) that can be processed by the analog-to-digital converter (ADC).

See section 4.2.4 for the implementation of voltage measurement.

3.6 Signal Conditioning

As mentioned earlier, the sensed signal must be conditioned before it can be processed. The extent to which conditioning is required depends mainly on the type of the sensor being employed . Signal conditioning consists of several steps.

3.6.1 Amplifier Circuit

Usually, the sensed signals are of considerably low amplitudes. For this reason an amplifier circuit must be used to convert the signals to appropriate levels and reduce the noise impact on signal quality.

The amplifier circuit can be implemented using standard operational amplifiers or instrumentation amplifiers. For very low level signals an instrumentation amplifier is preferable. Its advantage is that it amplifies the differential of the two input signals while cancelling out (rejecting) any signals that are common to both inputs, thereby ensuring that even small signals are extracted from the sensors. This feature of instrumentation amplifier is known as the common-mode rejection ratio (CMRR). The higher the CMRR, the better is the instrumentation amplifier. CMRR is expressed mathematically as:

$$CMRR = A_D \left(\frac{V_{CM}}{V_{OUT}} \right) \quad (3-13)$$

Where A_D is the differential gain of the amplifier, V_{CM} is the common-mode voltage present at both amplifier inputs, and V_{OUT} is the output voltage present when a common-mode input signal is applied to the amplifier.

In contrast to the instrumentation amplifier, a typical operational amplifier operated in the inverting or non-inverting amplifier configuration will process common-mode signals, passing them through to the output, without rejecting them as well [23].

Apart from high CMRR, instrumentation amplifiers are also favoured in many applications due to their high DC precision, low inherent noise, and high input impedance [24]. Other qualities like low offset voltage and offset voltage drift, frequency response (bandwidth and slew rate) and simple gain setting must also be considered in selecting an instrumentation amplifier.

3.6.2 Low-Pass Filter

To further reduce the effect of noise, the amplified signal must be filtered prior to digital conversion. Although the signals of interest here are fundamentally DC, there are high frequency signals present in the measurement circuits. These high frequency signals are generated in the switching circuits outside of an amplifier or come from inside of the amplifier itself.

Filtering ensures that the signal is clean (free of noise), and it contains frequencies only in a certain range (band-limited) [25]. Filtering is implemented using anti-aliasing low-pass filters. These are analog filters that attenuate any input signal with a frequency greater than the cut-off frequency.

The basic low-pass filtering system is shown in Figure 3-16.

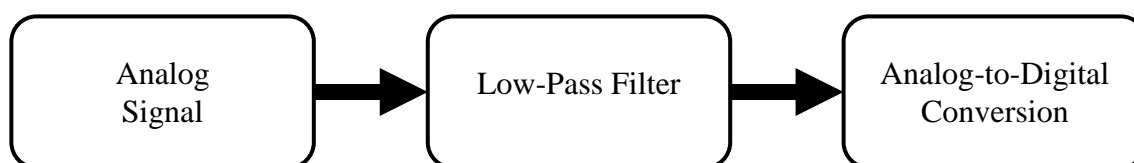


Figure 3-16: Low-Pass Filtering System Overview.

The most popular low-pass filter architectures are the Sallen-Key and the Multiple Feedback (MFB) architectures. The Sallen-Key architecture is non-inverting and it is more accurate in unity-gain configuration [24] while the MFB is inverting and is commonly used when high Qs and high gain are required [26].

3.7 Cleaning of PV Panels

To constantly keep one panel clean, an effective cleaning mechanism must be implemented. The cleaning system needs to be effective enough to remove even sticky dirt like bird droppings. Several existing solar panel cleaning mechanisms have been analysed and summarised by Al-Dhaheeri et al. [27] as listed in Table 3-1.

Table 3-1: Analysis of Cleaning Mechanisms.

Cleaning System	Advantage	Disadvantage
Manual	Cleaning only when required.	Cost varies depending on location and manpower. Time consuming and inefficient.
Transparent Shields	No mechanical movement to scratch the protective surface.	Requires high voltage for good performance. Causes shading when used on a PV panel. Cannot be directly powered from the panel.
Electro-Dynamics Screen (EDS-PV)	Efficient and can be used to remove dust from a variety of surfaces.	Requires 3-phase high voltage amplifier which is a problem in remote locations.
Integrated Electro Dynamic Screens	Efficient with and without use of external power supply.	Requires a Digital Signal Controller (DSC) which is costly. Requires switching devices for converters hence more maintenance is required.
Standing Wave Electric Curtains	Highly efficient at high gas pressure	Removal is difficult when gas pressure is below a certain limit. Dust removal capability depends on the size of the particles deposited.
Solarbrush PV Robot	Automated robot	Heavy weight and high initial cost. Requires human interference.

In deciding on a cleaning mechanism, factors like lack of water, power source accessibility, space availability and maintenance are crucial.

To tackle some of those challenges, the automated cleaning system is preferable, provided it consumes low power and water, and requires minimal maintenance. Such a cleaning mechanism must also be designed in a way that its mechanical parts do not shade the panels during the day.

CHAPTER 4 DESIGN OF THE MPPT BATTERY CHARGER

4.1 Overview

This chapter provides in-depth details about the hardware and software design of the MPPT battery charger as well as the selection of its major components. The theory of operation of the MPPT battery charger is documented in section 3.4.

As mentioned in Chapter 2, commercial MPPTs could not be employed for this project because they all have customisation limitations and they are not research oriented (cost-prohibitive, not reprogrammable, while some have no data logging and communication capabilities).

The developed MPPT battery charger is fully reprogrammable and can be customised to accomplish different research requirements by simply modifying the firmware. In such a way, the researcher (operator) has total control over its functions and limitations. In addition, this MPPT battery charger is equipped with on board data logging functionality and memory as well as a communication interface with the computer and other intelligent devices.

4.2 Hardware Design

This section concentrates on the hardware design processes, decisions and reasoning for component selections made. The designs and selections are done in collaboration with the theories and equations analysed in Chapter 3.

4.2.1 Design Parameters

Prior to embarking upon the design process, numerous design and operating parameters of the MPPT battery charger must be fixed. The main motive behind that is to ensure that the resulting device is compatible with most commercial solar panels and batteries that might be used in this research and in the future.

The parameters selected for the design of the MPPT battery charger are listed in Table 4-1.

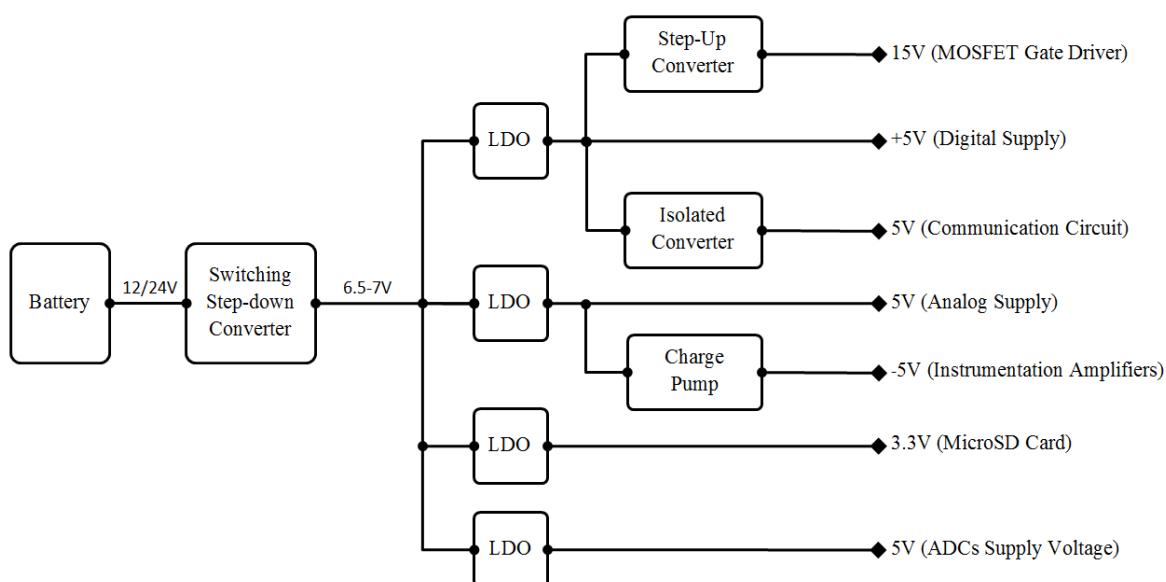
Table 4-1: MPPT Battery Charger Design Parameters.

Parameter	Value
Maximum Input Voltage (V_{in})	100V/5A or 50V/10A
Output Voltage (V_{out})	12V or 24V
Maximum Input Current (I_{in})	5A/100V or 10A/50V
Maximum Load Current (I_{out})	36A/12V
Switching Frequency (f_s)	40kHz
Maximum Output Ripple Voltage (Δv_{out})	1.5V
Maximum Output Ripple Current (Δi_L)	3.6A

The switching frequency was selected in consideration with the inductor sizes as well as the microcontroller capabilities to generate a PWM signal with such a frequency. The ripple values are selected to be ten (10 %) percent of the respective expected average values.

4.2.2 Power Supply

The primary power supply of the MPPT battery charger is a 12 V battery or two 12 V batteries in series as shown in Figure 4-1.

**Figure 4-1:** Simplified MPPT Power Supply Circuit.

The battery voltage is manipulated using switching converters, Low Dropout Regulators (LDO) and isolated converters to produce different voltage levels required for the several applications of MPPT battery charger. See also the power supply schematics in Appendix F.

4.2.3 Current Measurement

The current measurement method selected for the MPPT is the shunt resistor technique. The combination of factors like cost, physical size (PCB space) and accuracy, made this method more preferable at the specified current magnitude in comparison to the other methods.

The simplified current measurement circuit is presented in Figure 4-2 below.

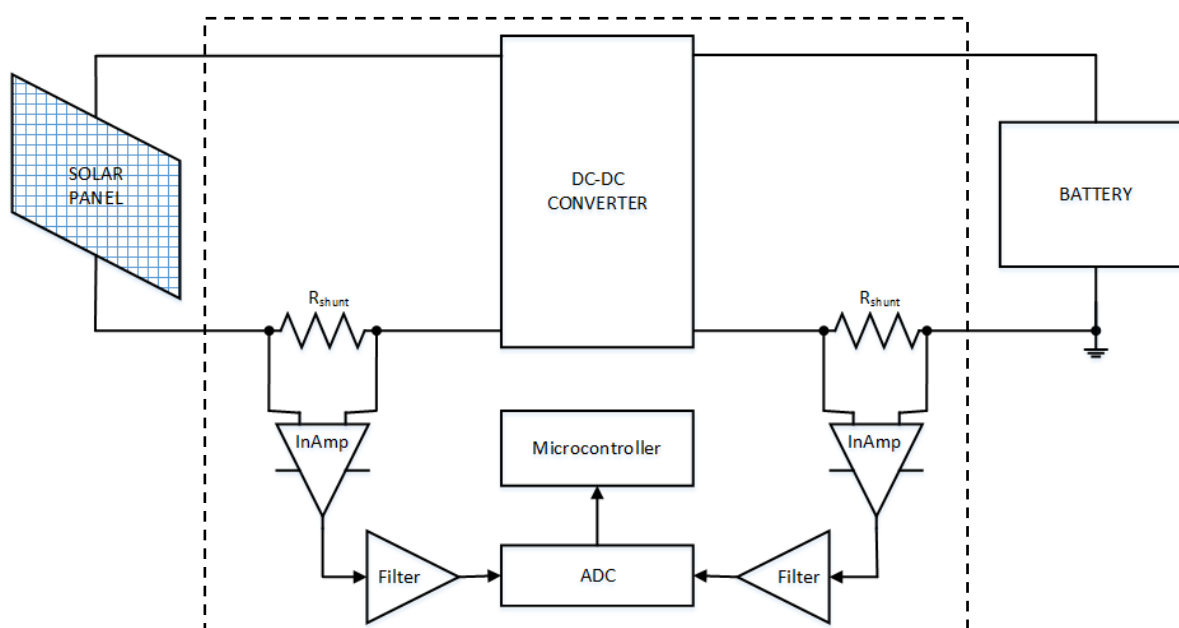


Figure 4-2: MPPT Current Measurement Circuit.

The transducer is a low resistance ($5\text{ m}\Omega$), 5 W , open air resistor. One of these resistors can measure a maximum current of approximately 31 A , producing a maximum voltage drop of 155 mV at that current. Apart from low resistance, this resistor has other benefits like low cost and small physical dimensions ($21.34 \times 1.65 \times 25.4\text{ mm}$).

For measurement of currents higher than 31 A , sensing resistors are connected in parallel.

The signal (voltage drop across the shunt resistor, R_{shunt}) is then buffered and amplified by a high speed, high CMRR instrumentation amplifier (INA111). The INA111 is attractive

because of its low offset voltage and offset voltage drift – thereby providing high DC accuracy.

The MPPT battery charger is designed to measure input currents up to 10 A. One sensing resistor is therefore employed and an appropriate gain is set for its instrumentation amplifier.

The output is capable of measuring currents up to 40 A. Two sensing resistors are therefore employed in parallel and an appropriate gain is set for its instrumentation amplifier that would result in approximately 5V at maximum current flow.

Due to high converter switching frequencies and also because of sensing on the lower side (near the ground rail), electronic noise is inevitable. After amplification, an anti-aliasing Sallen-Key low-pass filter is thus employed. The implementation of the Sallen-Key filter is presented in section 4.2.5.

The filtered signal is then converted into digital form by 16-bit ADCs. After digitisation, the signal can now be processed by the microcontroller for computations, storage or display. The microcontroller's built-in ADCs were not preferred because of their low resolution (10-bit) and low sampling speed (15 ksps).

4.2.4 Voltage Measurement

The voltage sensor is made up of a potential divider resistor network which scales down the measured value to a value within the amplifier's rail limits (5V). The resistor values are determined such that the expected maximum input voltage results into approximately 5V at the output of the potential divider.

Furthermore, the scaled down measurement value is buffered by a unity gain operational amplifier. The simplified voltage measurement circuit is shown in Figure 4-3 below.

Any noise that may still be part of the voltage signal after amplification is then filtered out by a Sallen-Key low-pass filter before it is converted to a digital value.

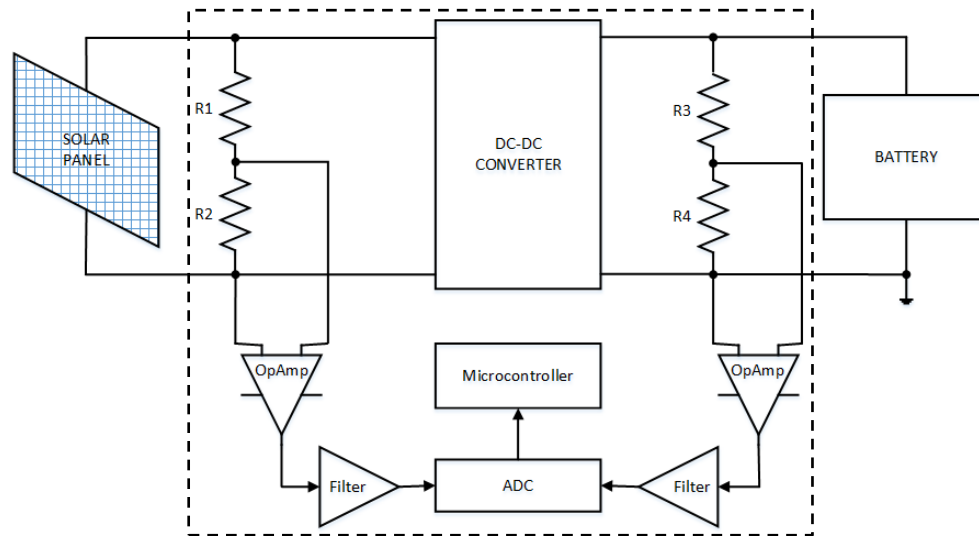


Figure 4-3: MPPT Voltage Measurement Circuit.

4.2.5 Sallen-Key Low-Pass Filter

After analysing other filter topologies, a Sallen-Key low-pass filter topology was selected. Compared to the Multiple Feedback topology, the Sallen-Key low-pass filter topology is advantageous in that it is non-inverting and its implementation requires fewer components. In addition, the Sallen-Key low-pass filter is more accurate in a unity-gain configuration [24] in which it is implemented here.

Figure 4-4 shows the circuit of the Sallen-Key low-pass filter.

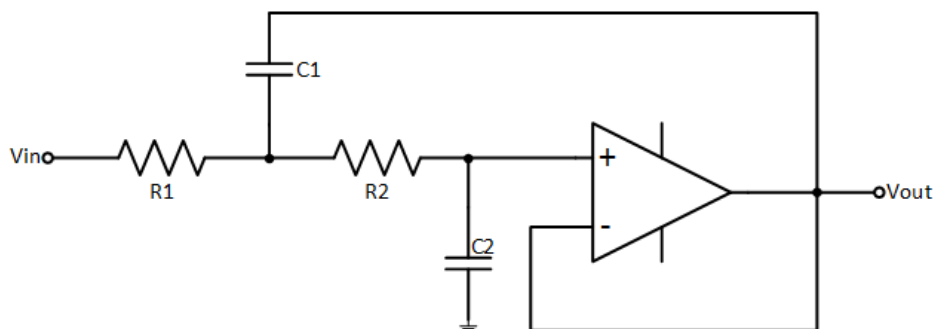


Figure 4-4: Sallen-Key low-pass filter.

The Sallen-Key low-pass is formed up by the operational amplifier (MCP601), and the two resistors and capacitors whose values determine the cut-off frequency of the filter.

4.2.6 The Switching Devices

The switching device selected is the enhancement power MOSFET, IRFB4115. The advantages of this MOSFET are low ON-resistance and high current capacity. Its main parameters are listed in Table 4-2.

Table 4-2: Selected MOSFET specifications.

V_{DS} (V)	ON-Resistance (max) (m Ω)	Drain Current (A)	$V_{GS(max)}$ (V)	Operating Junction Temperature ($^{\circ}$ C)
150	11	104	20	175

Although a synchronous converter is implemented in this MPPT battery charger, a diode is still employed in parallel with the lower MOSFET to ensure continuous current flow during dead time (when both lower and upper MOSFETs are OFF). The diode provides a current path for a very short time (approximately 520ns) and thus its losses cannot significantly influence the efficiency of the MPPT battery charger.

4.2.7 Inductor Design

The inductor is a crucial part of a DC-DC converter. Apart from its inductance, other critical factors must be considered in the inductor design process. However, the end goal is to achieve the required inductance without saturating the inductor's core and to conduct the maximum load current with the minimum winding resistance or copper losses [17].

Several inductor design methods for various applications are proposed in literature. All these methods, however, have their advantages and shortcomings.

The inductor (L1 in Appendix F) was designed using the K_g method. This method starts by calculating a geometric constant K_g using specified initial inductor parameters. After finding K_g a core with a K_g greater than or equal to the calculated K_g value is selected. This method is recommended for applications where winding losses (efficiency) are a major concern [17].

The minimum inductance value is determined by using equation (3-7):

$$L = \frac{V_{in} - V_{out}}{\Delta i_L} D T_s$$

$$L = \frac{100-12}{3.6} \cdot 0.12 \cdot 25 \cdot 10^{-6} = 73.3 \mu\text{H}$$

Where V_{in} , is the maximum input voltage, V_{out} , is the minimum output voltage, Δi_L is peak-peak inductor ripple current value (A) and T_s is the switching period in seconds.

A ferrite core was selected and a saturation flux density (B_{max}) of 0.25 T was cautiously selected. Saturation flux density of ferrite cores falls within a wide range but the actual saturation flux density depends on the specific ferrite material.

Furthermore, to avoid saturation, an air gap is employed in the selected core. The inductor of the MPPT battery charger was designed using the following six steps.

Table 4-3 lists the specifications employed in the design of the inductor of the MPPT battery charger.

Table 4-3: Inductor Design Specifications.

Inductor Design Specifications					
Wire Resistivity (ρ)	Maximum Current (I_{max})	Inductance (L)	Winding Resistance (R)	Winding Fill Factor (K_u)	Maximum Flux Density (B_{max})
$1.724 \times 10^{-6} \text{ m}\Omega$	37.8 A	75 μH	0.01 Ω	0.5	0.25 T

Step 1: The K_g constant is calculated and the core size is determined.

$$K_g \geq \frac{\rho L^2 I_{max}^2}{B_{max}^2 R K_u} 10^8 \quad (4-1)$$

$$K_g \geq \frac{(1.724 \cdot 10^{-6}) \cdot (75 \cdot 10^{-6})^2 \cdot 37.8^2}{0.25^2 \cdot 0.01 \cdot 0.5} 10^8$$

$$K_g \geq 2.944 \text{ m}^5$$

$I_{max} = I_{out} + \frac{1}{2} \Delta i_L$, is the maximum load current (DC component plus ripple current).

The EE65/32/27 core was selected and its parameters are noted in Table 4-4.

Table 4-4: Core Specifications

Core type, Shape & Size	Cross Sectional Area A_c , [cm^2]	Bobbin Winding Area W_a , [cm^2]	Mean Length/ Turn MLT , [cm]
EE65/32/27	2.86	5.40	14.70

Step 2: The air gap length is calculated.

$$l_g = \frac{\mu_0 L I_{max}^2}{B_{max}^2 A_c} 10^4 \quad (4-2)$$

$$l_g = \frac{(4\pi \cdot 10^{-7}) \cdot (75 \cdot 10^{-6}) \cdot 37.8^2}{0.25^2 \cdot 2.86} \cdot 10^4$$

$$l_g = 0.0051 \text{ m}$$

Step 3: The number of turns are determined.

$$n = \frac{L I_{max}}{B_{max} A_c} 10^4 \quad (4-3)$$

$$n = \frac{(75 \cdot 10^{-6}) \cdot 37.8}{0.25 \cdot 2.86} \cdot 10^4$$

$$n = 32$$

Step 4: In this step, the size of the winding wire is calculated.

$$A_w \leq \frac{K_u W_A}{n} \quad (4-4)$$

$$A_w \leq \frac{0.5 \cdot 6.4}{32} = 0.084 \text{ cm}^2$$

$$A_w \leq 0.084 \text{ cm}^2$$

From the American Wire Gauge, a wire size of AWG #9 is selected. This wire has a cross-sectional area $A_w = 0.066 \text{ cm}^2$.

Step 5: The total resistance of the winding wire is determined.

$$R = \frac{\rho n (MLT)}{A_w} \quad (4-5)$$

$$R = \frac{(1.724 \cdot 10^{-6}) \cdot 32 \cdot 14.7}{0.066}$$

$$R = 0.012 \Omega$$

Step 6: Finally, the actual winding losses are determined.

$$P = I_{max}^2 R \quad (4-6)$$

$$P = 37.8^2 \cdot 0.010$$

$$P = 18 \text{ W}$$

The inductor was built and tested, and it met the design requirements in terms of saturation and inductance.

4.2.8 Capacitor Selection

The output capacitor is also a crucial component in the function of the MPPT battery charger. It determines the magnitude of ripples on the output voltage.

The minimum value of the output capacitor (C3 and C4 in Appendix F) is determined by using equation (3-8).

$$C_{out} = \frac{\Delta i_L T_s}{8\Delta v_{out}}$$

$$C_{out} = \frac{3.6 \cdot (25 \cdot 10^{-6})}{8 \cdot 1.5}$$

$$C_{out} = 7.5 \mu\text{F}$$

This calculated value of the output capacitor is merely a minimum value; the actual capacitor must be selected based on its ESR value which determines its ripple current and temperature handling capabilities. Two 250V, 1000 μF electrolytic capacitors with $ESR = 130 \text{ m}\Omega$ are used in parallel to increase their ripple current handling capability.

To minimise the effects of voltage ripples on the input (C1 and C2 in Appendix F) of the MPPT battery charger and to protect the solar panels from voltage surges, an input capacitor is also employed. Two 250V, 1000 μF electrolytic capacitors with $ESR = 40 \text{ m}\Omega$ are used in parallel as well.

4.2.9 Power Dissipation and Thermal Management

The total power dissipated in the switching devices determines the size of the heat sinks required. Losses in the MOSFETs (Q2 and Q3 in Appendix F) are calculated below and an appropriate heat sink was selected.

The rated input conditions for the MPPT battery charger are 100V/5A or 50V/10A. The losses are calculated for the worst case current; when the output and input voltages are lowest i.e. 12 V and 50 V respectively. This combination results in the highest load current of approximately 40 A, and each MOSFET will carry only half (20 A) of this value. The switching losses are calculated separately for each pair of switching devices.

$R_{ds(on)} = 11 \text{ m}\Omega$ is the ON-resistance for each IRFB4115 MOSFET. There are three portions of power dissipation in the operation of each MOSFET.

a) Conduction Losses:

Upper MOSFETs:

$$P_{on1} = I_{max}^2 \cdot R_{ds(on)} \cdot D \quad (4-7)$$

$$P_{on1} = 20^2 \cdot (11 \cdot 10^{-3}) \cdot 0.24$$

$$P_{on1} = 2.112 \text{ W}$$

Lower MOSFETs:

$$P_{on2} = I_{max}^2 \cdot R_{ds(on)} \cdot (1 - D) \quad (4-8)$$

$$P_{on2} = 20^2 \cdot (11 \cdot 10^{-3}) \cdot (1 - 0.24)$$

$$P_{on2} = 2.288 \text{ W}$$

b) Switch-ON Transition Losses:

Upper MOSFETs:

$$P_{tr,on1} = \frac{I_{max} V_{DS} T_r f_s}{2} \quad (4-9)$$

$$P_{tr,on1} = \frac{20 \cdot 50 \cdot (73 \cdot 10^{-9}) \cdot (40 \cdot 10^3)}{2}$$

$$P_{tr,on1} = 1.820 \text{ W}$$

V_{DS} is the maximum drain-source voltage; T_r is the rise time of the MOSFET, and f_s is the switching frequency.

Lower MOSFETs:

$$P_{tr,on2} = \frac{I_{max} V_{DS} T_r f_s}{2}$$

$$P_{tr,on2} = \frac{20 \cdot 50 \cdot (73 \cdot 10^{-9}) \cdot (40 \cdot 10^3)}{2}$$

$$P_{tr,on2} = 1.820 \text{ W}$$

c) Switch-OFF Transition Losses:

Upper MOSFETs:

$$P_{tr,off1} = \frac{I_{max}V_{DS}T_f f_s}{2} \quad (4-10)$$

$$P_{tr,off1} = \frac{20 \cdot 50 \cdot (39 \cdot 10^{-9}) \cdot (40 \cdot 10^3)}{2}$$

$$P_{tr,off1} = 1.600 \text{ W}$$

Where T_f is the fall time of the MOSFET i.e. the time it takes for the MOSFET to transit into the off state.

Lower MOSFETs:

$$P_{tr,off2} = \frac{I_{max}V_{DS}T_f f_s}{2}$$

$$P_{tr,off2} = \frac{20 \cdot 50 \cdot (39 \cdot 10^{-9}) \cdot (40 \cdot 10^3)}{2}$$

$$P_{tr,off2} = 1.600 \text{ W}$$

d) Total Power Dissipation.

The total power dissipated in each upper MOSFET is therefore the sum of the three components.

$$P_{d1} = P_{on1} + P_{tr,on1} + P_{tr,off1} \quad (4-11)$$

$$P_{d1} = 2.112 + 1.820 + 1.600$$

$$P_{d1} = 5.532 \text{ W}$$

And the total power dissipated in the lower MOSFETs is:

$$P_{d2} = P_{on2} + P_{tr,on2} + P_{tr,off2}$$

$$P_{d2} = 2.288 + 1.820 + 1.600$$

$$P_{d2} = 5.708 \text{ W}$$

The switching losses of the MPPT battery charger calculated are summarised in Table **4-5**.

Table 4-5: Summary of the switching losses in the MPPT battery charger.

LOSSES	UPPER MOSFET	LOWER MOSFET
Conduction losses	2 x 2.112 W	2 x 2.288W
ON Transition Losses	2 x 1.820 W	2 x 1.820 W
OFF Transition Losses	2 x 1.600 W	2 x 1.600 W
Total	11.064 W	11.416 W

This means that at maximum load current, approximately 23W is being dissipated as heat through the MOSFETs. This is approximately 4.5% of the MPPT battery charger rated power. These losses bring with them serious concerns, not only that they reduce the overall efficiency of the MPPT battery charger but they also create a problem of overheating in the MOSFET's junction with a potential of inflicting permanent damage.

The junction temperature of the MOSFETs without heat sink is calculated below.

For each upper MOSFET,

$$T_{j1} = T_A + P_{d1}(\theta_{jc} + \theta_{ja}) \quad (4-12)$$

$$T_{j1} = 40 + 5.532(0.40 + 62)$$

$$T_{j1} = 385.197 \text{ } ^\circ\text{C}$$

T_A is the ambient temperature (taken as 40°C), θ_{jc} and θ_{ca} are junction-to-case (0.4 °C/W) and junction-to-ambient (62 °C/W) thermal resistances of the MOSFET, respectively.

For the lower MOSFETs:

$$T_{j2} = T_A + P_{d2}(\theta_{jc} + \theta_{ja})$$

$$T_{j2} = 40 + (5.708 \cdot (0.40 + 62))$$

$$T_{j2} = 396.179 \text{ } ^\circ\text{C}$$

Evidently, the calculated junction temperatures are very high.

Proper heat sinking ensures that heat dissipating components remain operating within their thermal limits. The major constraints to the selection of a heat sink are the PCB space it will occupy and its thermal resistance – with the latter being more critical.

The heat sink design in this case, is based on the total power dissipated by all the MOSFETs to be mounted on that heat sink. The maximum thermal resistance of the required heat sink is calculated from this relationship.

$$\begin{aligned}\theta_{ja} &= 2\theta_{jc} + 2\theta_{cs} + \theta_{sa} = \frac{T_j - T_A}{2(P_{d1} + P_{d2})} \\ \Rightarrow \theta_{sa} &= \frac{T_j - T_A}{2(P_{d1} + P_{d2})} - 2\theta_{jc} - 2\theta_{cs} \\ \theta_{sa} &= \frac{175 - 40}{22.480} - 0.8 - 1 \\ \theta_{sa} &= 4.205 \text{ }^\circ\text{C/W}\end{aligned}\tag{4-13}$$

θ_{jc} , θ_{cs} are the junction-to-case and case-to-sink thermal resistances, respectively. T_j is the maximum junction temperature allowed for that specific MOSFET (175 °C).

The heat sink selected for this application must have a thermal resistance less than or equal to 4.205 °C/W.

The details of the selected heat sink are tabulated below.

Table 4-6: Heat Sink Specifications.

Manufacturer	Part Number	Thermal Resist. (θ_{sa})	Dimensions	Mounting
AAVID Thermalloy	OS517/100/B	2,09 °C/W	100x40x75 mm	Force Clip

With this heat sink being utilised, the MOSFET's junction temperatures are now calculated with equation (4-12) modified to include the heat sinking effect.

For each upper MOSFET:

$$\begin{aligned}T_{j1} &= T_A + P_{d1}(\theta_{jc} + \theta_{cs} + \theta_{sa}) \\ T_{j1} &= 40 + (5.532 \cdot (0.4 + 0.5 + 2.09)) \\ T_{j1} &= 56.541 \text{ }^\circ\text{C}\end{aligned}$$

θ_{sa} and θ_{cs} are the case-to-sink and sink-to-ambient thermal resistances, respectively.

The junction temperature for each lower MOSFET is:

$$T_{j2} = T_A + P_{d2}(\theta_{jc} + \theta_{cs} + \theta_{sa})$$

$$T_{j2} = 40 + (5.708 \cdot (0.4 + 0.5 + 2.09))$$

$$T_{j1} = 57.067 \text{ } ^\circ\text{C}$$

By using this heat sink, it is evident that the junction temperatures of both MOSFET pairs are now maintained well within the IRFB4115 MOSFET's operating temperature range.

4.2.10 PCB Design

Schematics and the PCB Layout of the MPPT are attached as appendix F.

Figure 4-5 shows a picture of the MPPT battery charger PCB board with its major circuitries indicated in red numbered rectangles.

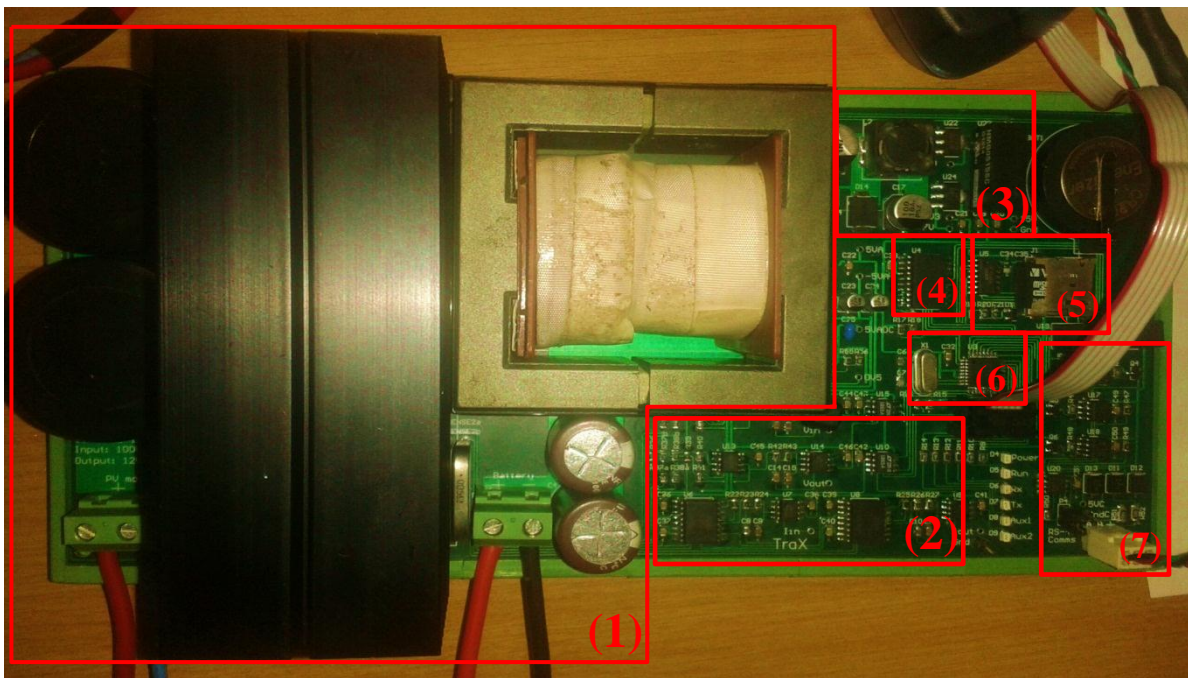


Figure 4-5: Picture of the MPPT battery charger.

The outlined circuits are: (1) Buck Converter circuitry (input capacitors, heatsink, inductor and output capacitors), (2) measurement circuitry, (3) power supply circuitry, (4) Real Time Clock, (5) Micro SD card, (6) microcontroller circuitry, and (7) the communication circuitry.

4.3 Software Design

This section details the development of the MPPT battery charger firmware. The microcontroller was programmed for the several peripherals and functions as explained further in detail.

4.3.1 PWM and Switching Frequency

Pulse Width Modulation (PWM) is a popular technique for power control. To keep the MPPT battery charger operating at MPP, the switching MOSFETs must be driven by a PWM signal of a specific frequency and a controllable (varying) duty cycle. The PWM signal is generated inside the microcontroller and it is outputted through a dedicated GPIO pin connected to the MOSFET's gate driver.

The process of PWM generation inside the microcontroller is based on timers/counter and it is well explained in the AVR's datasheet. Therefore, this section only discusses how to initialise the microcontroller for PWM generation i.e. setting up a timer(s) in PWM mode with the desired frequency and resolution.

Below is a flow diagram of the timer initiation and switching frequency selection.

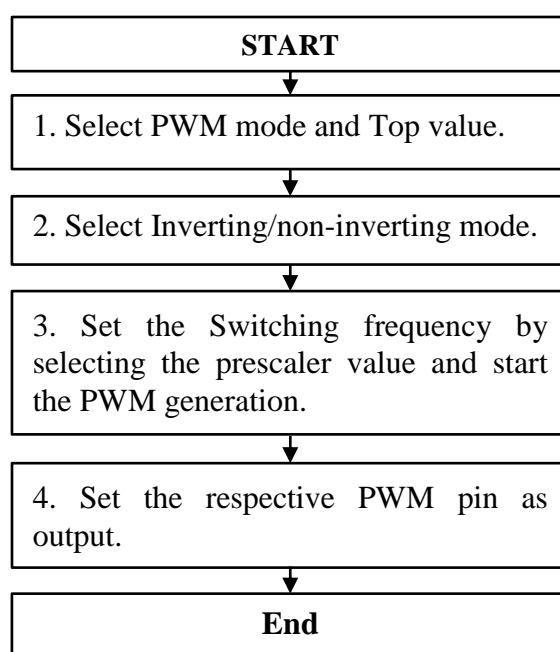


Figure 4-6: Flow diagram for PWM generation and switching frequency selection.

4.3.2 Communication (USART)

The communication (data and control commands) interface between the microcontroller in the MPPT battery charger and the outside world is realised through the Universal Synchronous/Asynchronous Receiver/Transmitter (USART).

The USART is a built-in peripheral for the Atmega328 and it only needs to be setup (initiated). The theory of operation of the USART is also adequately documented in the AVR datasheet. For that reason, only its initialisation and implementation is briefly discussed in this work.

Figure 4-7 shows a flow diagram for the USART settings.

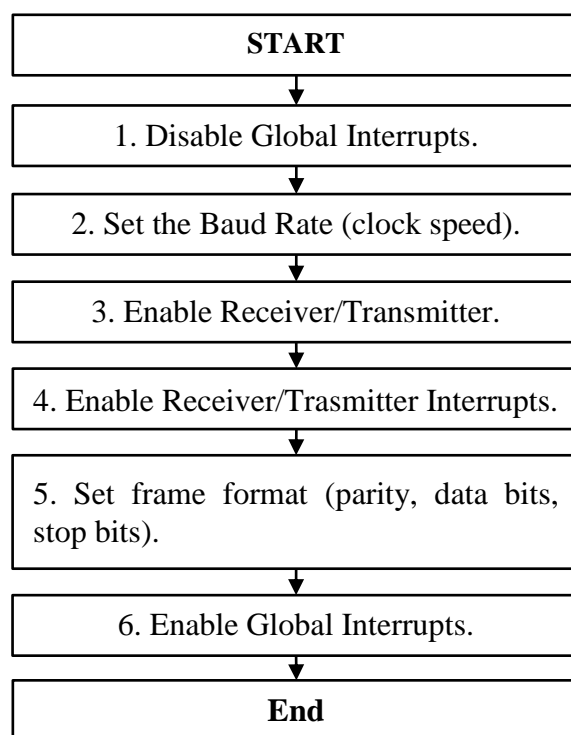


Figure 4-7: Flow Diagram for USART settings.

The communication is interrupt driven which eliminates the need to constantly check for data reception and it prevents missing data. Interrupt driven USART allows the firmware to deal only with communication whenever new information has been received via the USART thereby saving computation power and availing time to executing other equally important tasks. See Appendix A for the full flow diagrams of the USART communication settings.

4.3.3 ADCs and their Calibration

This section aims to explain the calibration process which is implemented to maintain measurement accuracy. As pointed out in section 4.2.3, external ADCs (LTC1865) are used. Each channel of the LTC1865 is accessed by sending the relevant 2-bit data word to the ADC and the measurement data is transmitted through the SPI to the microcontroller.

Calibration is performed to correct two ADC parameters which can adversely affect the accuracy of its conversion results. The offset and gain errors, amongst others, have a serious effect on the readings of the ADC.

An offset error is the constant deviation between the actual output value and the ideal output value of the ADC reading. Offset error is removed by subtracting the offset value from the ADC digital value. A gain error is defined as the difference between the slope of the actual output values and the slope of the ideal output values of the ADC.

The calibration process and its effect on the measurement results are demonstrated in Figure 4-8 below.

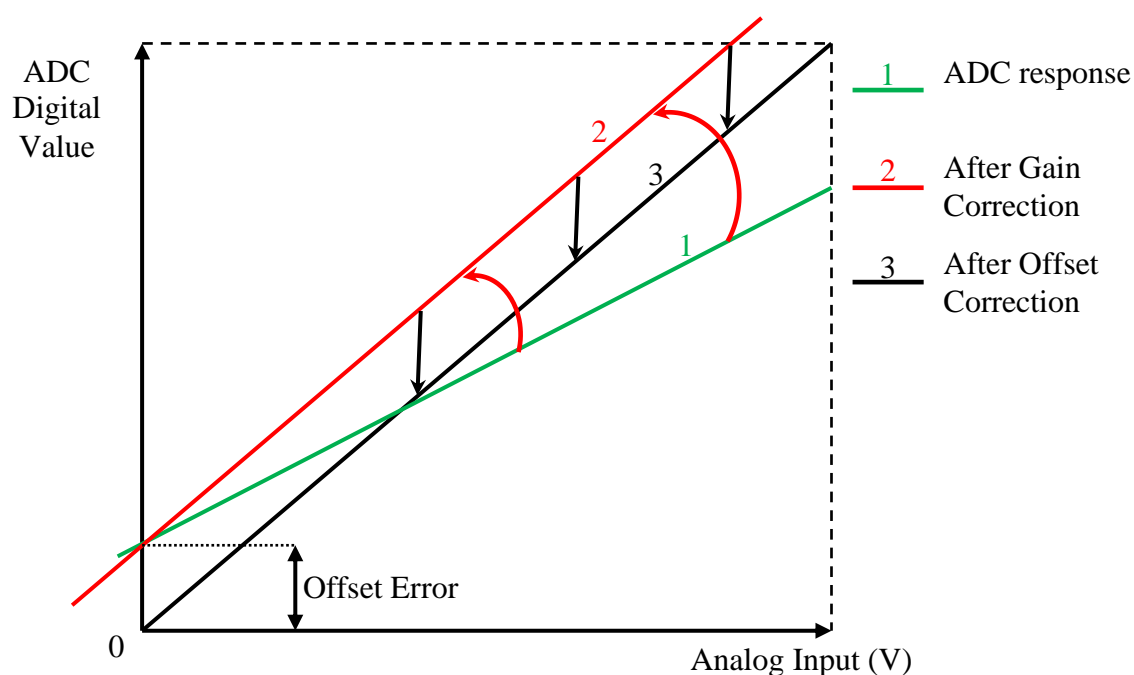


Figure 4-8: ADC calibration effects illustrated.

The relationship between the gain and the offset is linear and it can therefore reasonably be approximated for calibration purpose using the generic linear equation, $y = mx + c$.

$$ADC\ Digital\ value = (Gain \times Measurement) + Offset \quad (4-14)$$

$$\Rightarrow Measurement = \frac{ADC\ Digital\ Value - Offset}{Gain}$$

To calculate the gain and offset values, two input values and their corresponding raw ADC digital values are required; preferably one at the low end of the measurement range and the other at the high end of the range.

To realise accurate results after calibration, the input values must be measured with a highly accurate meter. The gain and the Offset value are then calculated as follow:

$$Gain = \frac{\Delta y}{\Delta x} = \frac{Raw\ code(k+1) - Raw\ code(k)}{Input(k+1) - Input(k)} \quad (4-15)$$

$$Offset = Raw\ code(k) - (Gain \times Input(k)) \quad (4-16)$$

The gain and offsets are unique for each ADC channel, for this reason calibration needs to be done for individual channels.

The calculated values are then sent to the device using the respective Modbus Command (see Appendix B - Modbus commands documentation) and they are stored in the non-volatile memory of the microcontroller. As a result calibration only needs to be done once for each channel and device or when the need arises for whatever reason. Detailed calibration procedures are attached in Appendix A.

4.3.4 Real Time Clock (RTC)

The RTC is necessary for accurate time keeping and to stamp data with real time and date at which it was measured during data logging.

The RTC chip used here is the DS3234. It is a highly accurate and it has low-power consumption. The RTC can be set and read using respective Modbus commands. It has a battery-backed memory that enables it to maintain its time settings accurately for a long time even in the absence of the main power supply.

See Appendix A for the RTC setting and reading flow diagrams.

4.3.5 Operating and Control Modes

The MPPT battery charger has two operating modes, namely charging and idle mode. The modes are subsequently comprised of several control modes as indicated by the flow diagram in Figure 4-9.

Whenever the MPPT battery charger is powered on, it can either be in the battery charging mode or in idle mode. The operation mode is determined by the operator through setting a flag with idle mode being the default mode.

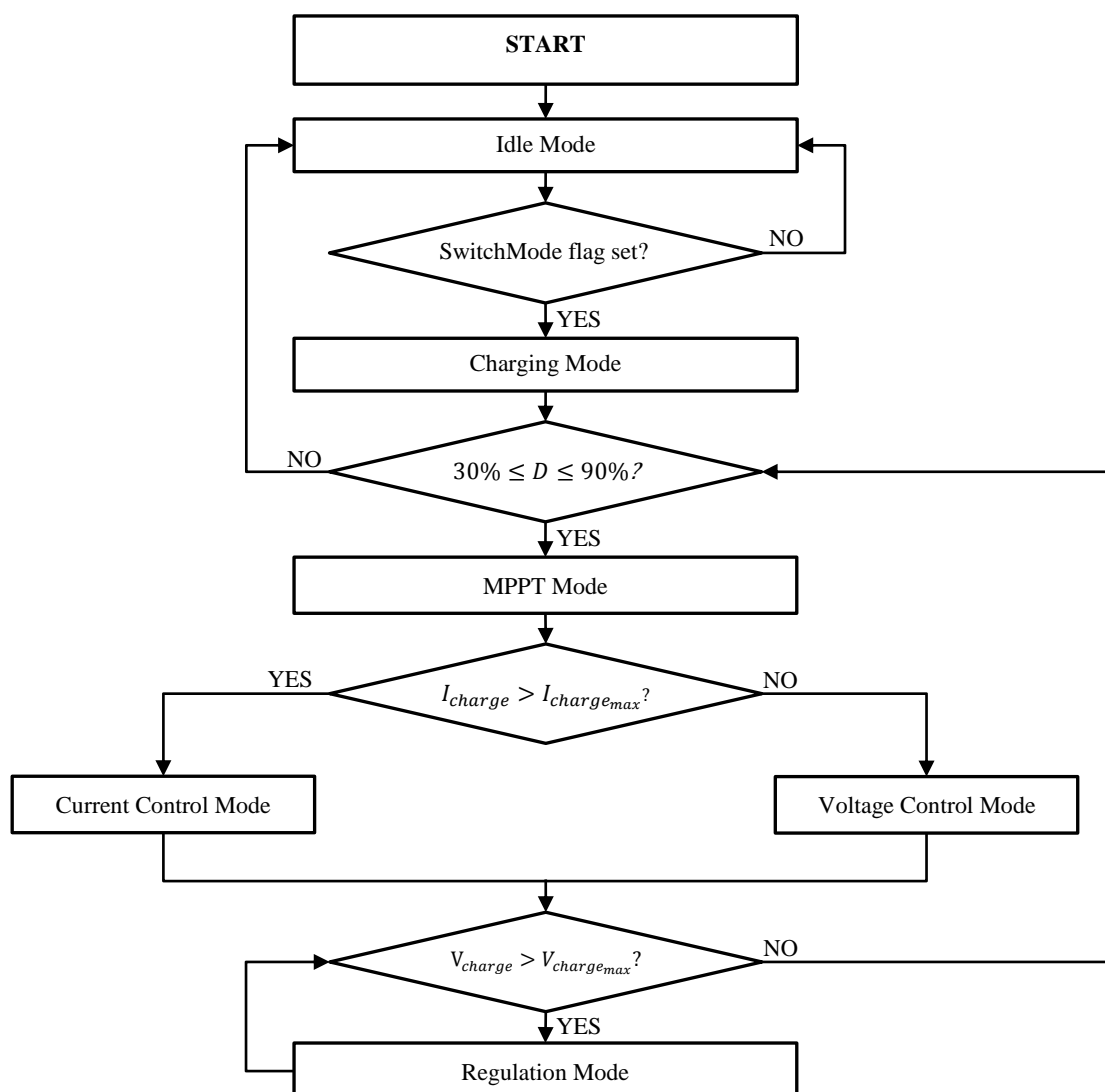


Figure 4-9: MPPT Operation and Control modes flow chart.

In idle mode, the MPPT battery charger is in monitor and evaluate state and its power consumption is very low (<100 mW). With this power consumption, the MPPT battery

charger can remain on for several days (cloudy days, for instance) without completely discharging the battery while constantly monitoring the PV panel's characteristics and availing data to the operator.

The charging mode is triggered by the operator setting the flag through the Modbus command. In this mode, P&O and battery charging control algorithms are executed. This mode is further divided into two control modes depending on the battery's state of charge; the MPPT mode (tracks the maximum power point) and the regulation mode.

In MPPT mode, voltage control algorithm is run until when the charge current has exceeded the set maximum charge current. If the charge current exceeds the set value, current control algorithm is employed. If there are no limit violations, the MPPT continues to operate in MPPT mode until the battery is fully charged or the operating mode is changed by the operator.

If the battery is fully charged, the MPPT battery charger moves into regulation mode. In regulation mode, the MPPT battery charger keeps the battery voltage floating at a set value until the battery voltage drops below that set value. The battery charging control modes are elaborated in section 4.4.2.

On the other hand, if the solar panel voltage has fallen below the minimum input threshold or the operation mode is changed, the MPPT battery charger transits into idle mode. If the PV panel's voltage rises above the battery voltage while the battery is not full, charging starts automatically if the charging mode flag is still set.

4.3.6 P&O Algorithm Implementation

As stated earlier, the algorithm selected for the MPPT battery charger is the Perturb and Observe technique. The principle of operation of this algorithm is discussed in detail in section 3.4.6. A detailed flow diagram of the P&O algorithm implementation is presented in Appendix A.

MPP tracking is triggered through a Modbus command, after which the MPPT battery goes into charging mode where a start-up routine is performed. The start-up duty cycle is calculated using the PV panel's open-circuit voltage and the battery voltage $\left[D_{start} = \frac{V_{Bat}}{V_{PV}} \right]$.

The MPPT battery charger transits into MPPT mode if the calculated starting duty cycle (D_{start}) satisfies the prescribed boundary conditions. In this mode perturbation starts until the MPP is reached. How fast the MPP is reached depends on the perturbation frequency and step size. The optimum perturbation speed and steps were determined through an iteration process. A perturbation frequency of 5 Hz was found to be more stable and accurate as compared to higher perturbation frequencies.

4.4 Testing and Results

The MPPT battery charger was built and tested with two Solara 55W panels mounted on the roof of the Electrical Electronic Department and two 12V lead acid batteries at its output in both 12V and 24V combinations.

The size of the connected battery is automatically detected and the right starting duty cycle is calculated. The battery size also determines the MPPT's minimum and maximum operating duty cycles.

The characteristics (STC) of the solar panels used to test the MPPT battery charger are shown in Table 4-7.

Table 4-7: Characteristics (STC) of the test panels.

Open Circuit Voltage (V_{oc})	Short Circuit Current (I_{sc})	Maximum Power Voltage (V_{MP})	Maximum Power Current (I_{MP})	Maximum Power Point (P_{MPP})
21.25V	3.40A	17.55V	3.13A	55W

Two panels were connected in series to increase their operating voltage which enables testing of both 12V and 24V battery charging operations. The operating characteristics of the series combination of the panels are shown next in Table 4-8.

Table 4-8: Operating characteristics (STC) of two test panels in series.

Open Circuit Voltage (V_{oc})	Short Circuit Current (I_{sc})	Maximum Power Voltage (V_{MP})	Maximum Power Current (I_{MP})	Maximum Power Point (P_{MPP})
42.50V	3.40A	35.10V	3.13A	110W

At MPP, the available power is more than what the test battery can absorb. Therefore, to test the operation of the MPPT battery charger at higher currents than what these particularly small batteries would allow, the battery was loaded with a variable resistor.

The circuit used to test the MPPT battery charger is indicated in Figure 4-10 below.

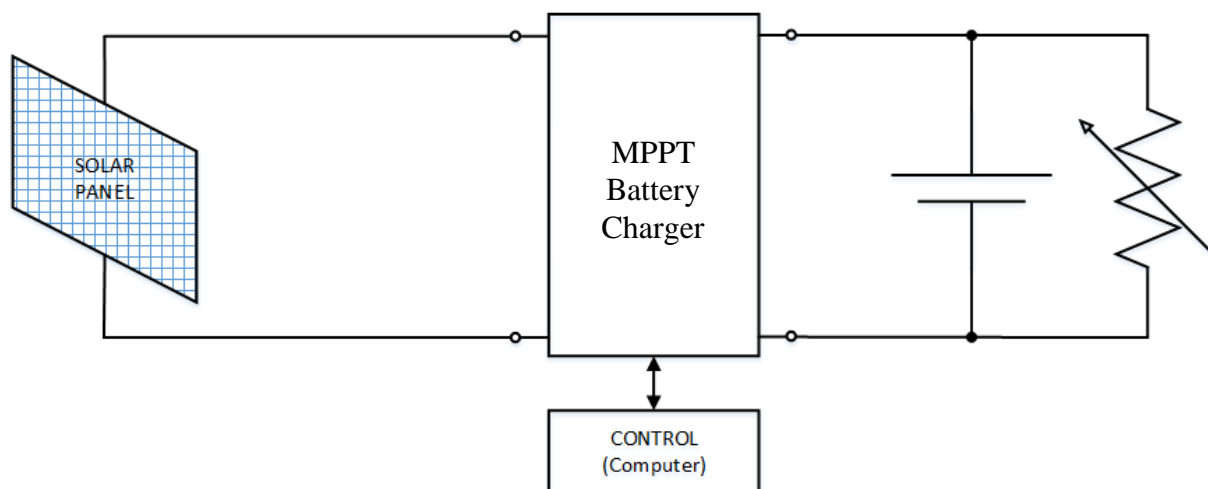


Figure 4-10: Test Circuit of the MPPT battery charger.

Test results are presented in the next sections.

4.4.1 Algorithm Performance

Test results of the MPPT battery are presented in the figures below. In this first experiment, the MPPT battery charger was operated to charge a battery loaded with an external resistor to ensure that the maximum power generated by the panels can be consumed and 50 samples were recorded. For this test, the MPPT's output voltage was fixed at 15V while charging a 12V battery.

As can be seen on the next figures, the MPPT has managed to operate the panels at MPP stably. The MPP was reached quickly within few seconds, and the oscillations observed around the MPP are quite minimal.

Test data for this experiment is attached as Appendix D.

Figure 4-11 shows the output voltage of the panel changing from V_{OC} to V_{MP} and when the MPPT battery charger is switched on.

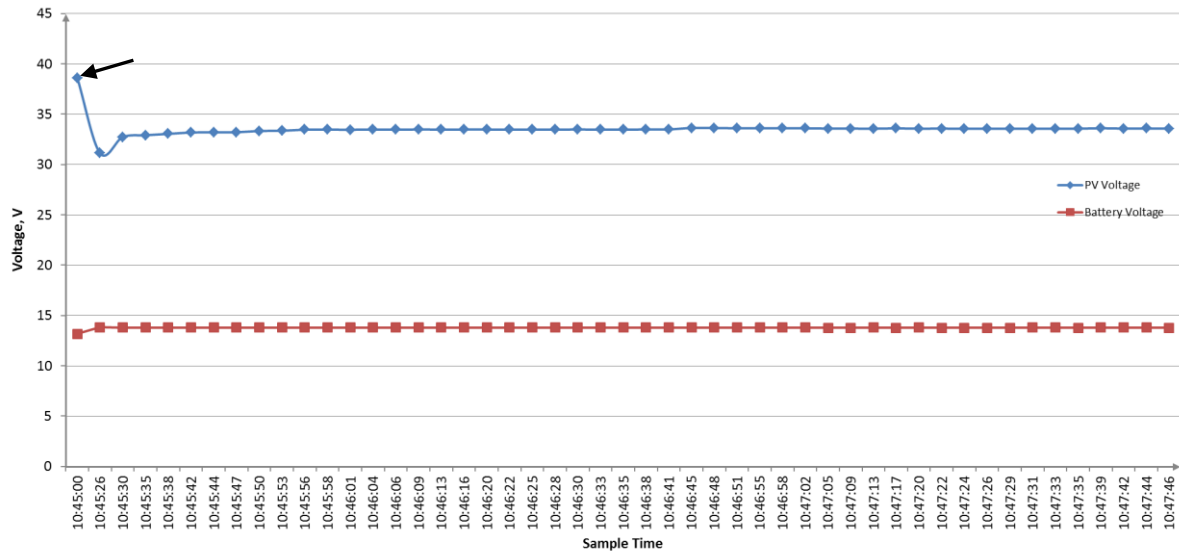


Figure 4-11: PV and Battery voltages before and after switching on the MPPT battery charger.

More operating characteristics of the MPPT battery charger are shown in Figure 4-12 below. This figure is particularly demonstrating that the operating duty cycle stayed fairly constant as soon as the MPP is reached – a sign of stable tracking.

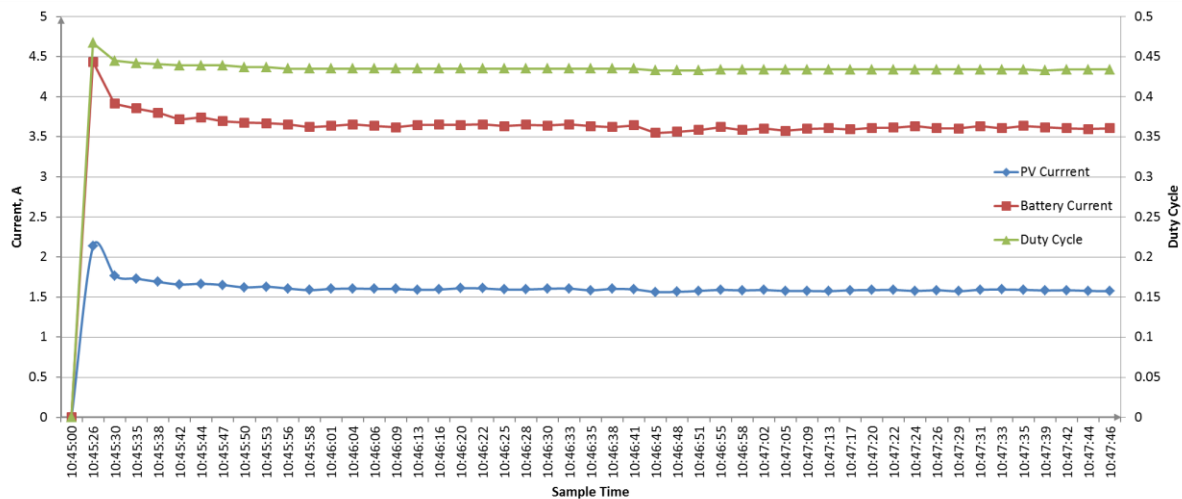


Figure 4-12: Change in PV Current, output current and the duty cycle.

Next, the dynamic response of the MPPT battery charger to loading is demonstrated in Figure 4-13 and Figure 4-14 below. The MPPT battery charger was operated in the same manner as in the previous test, and then the external resistor was disconnected from the battery (load reduced) while the MPPT battery charger is still tracking the MPP.

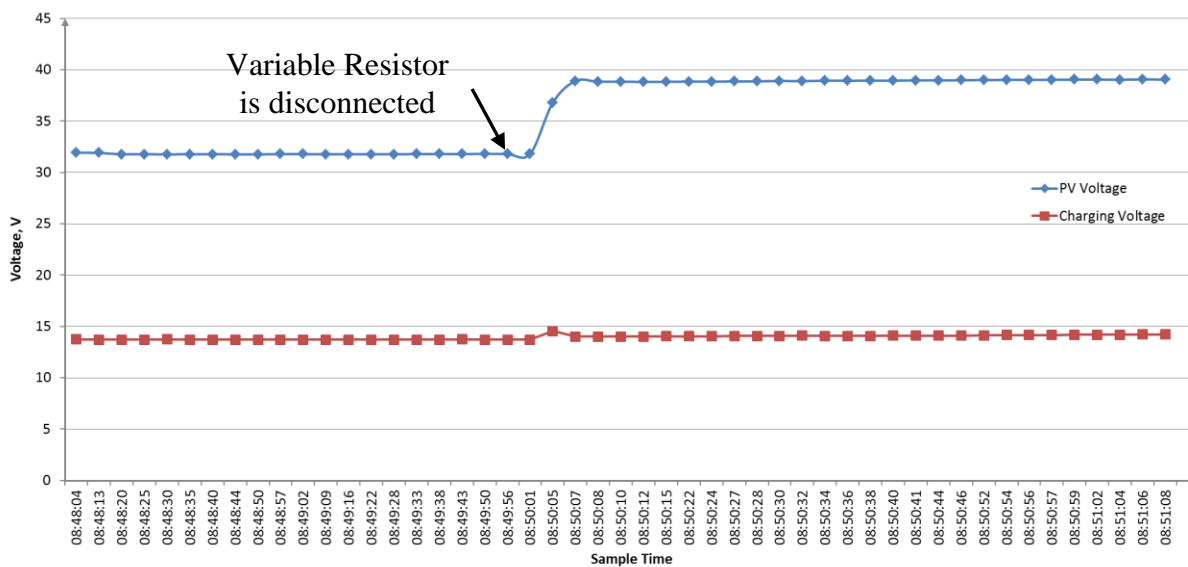


Figure 4-13: Test Results: MPPT’s dynamic response to loading (Voltages).

The response due to the reduction of the load on the output of the MPPT battery charger is also reflected on both the input and currents, and the duty cycle as shown in Figure 4-14.

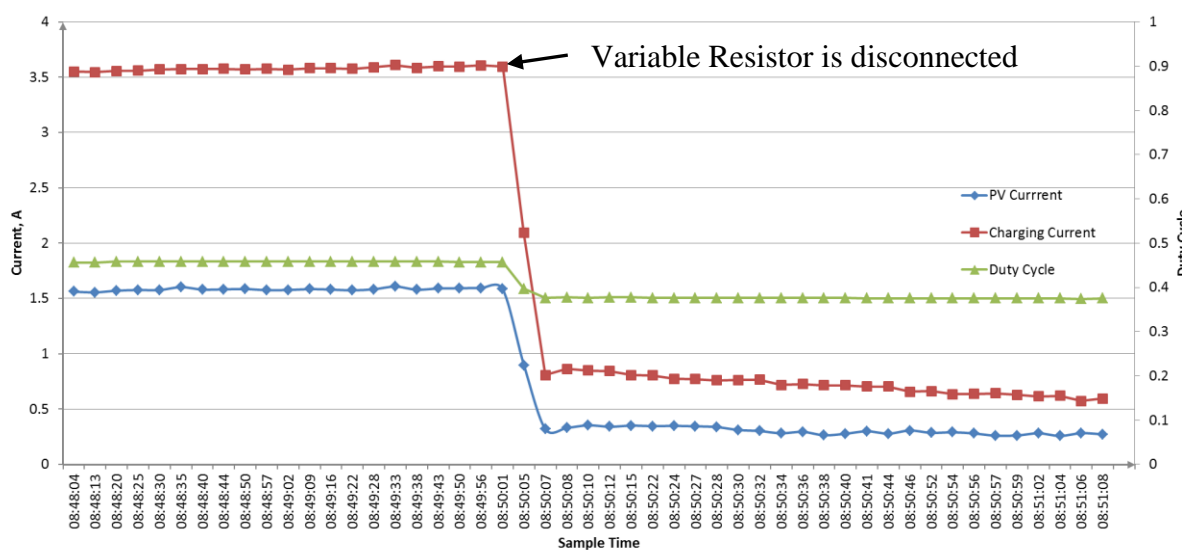


Figure 4-14: Test Results: MPPT’s dynamic response to loading (Currents and Duty Cycle).

This experiment demonstrates how the MPPT battery charger can accurately adjust its operating conditions when the load is reduced (variable resistor removed from the battery). The output voltage remained at the set value while the MPPT battery charger has adjusted its duty cycle and subsequently the output current to match the new power demand. This demonstrates the ability of the MPPT battery charger to charge the battery depending on its state of charge, until the charge voltage reaches the set value.

4.4.2 Battery Charging Algorithm

There are several algorithms for battery charging recommended in different literature, however the method proposed by Koutroulis and Kalaitzakis [28] was found to be easier to implement. It also performed stably and charged the battery faster.

This battery charging algorithm consists of two stages or modes shown in Figure 4-15 below. The first stage involves keeping output voltage (charge voltage) of the MPPT battery charger 1V higher than the measured battery voltage. The MPPT battery charger operates in this mode until the battery voltage rises to a set voltage level (14.4V for 12V battery or 29V for the 24V battery), after which the operation of the MPPT battery charger moves to stage two where the charge voltage is fixed at a specific value, floating voltage.

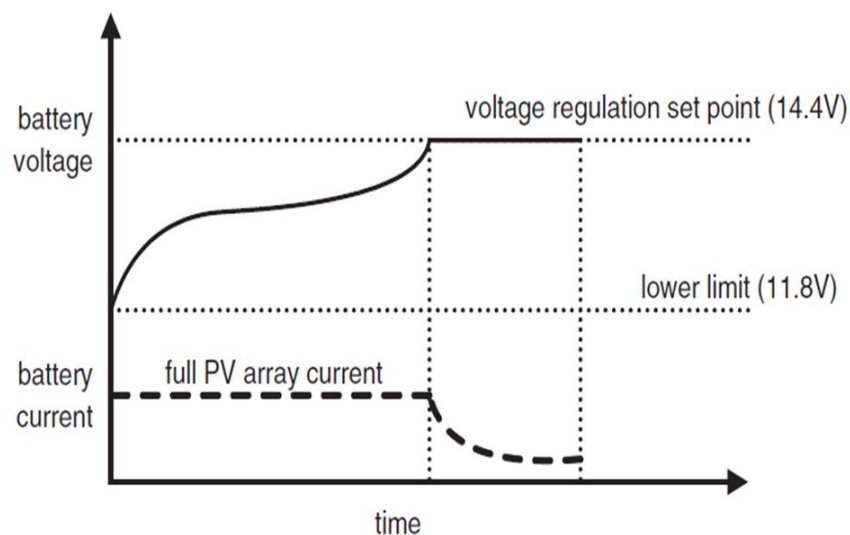


Figure 4-15: Battery charging and control method [28].

In stage two, the charge current reduces as the battery approaches a full state of charge and the MPPT battery charger transits into trickle mode to maintain the battery fully charged. It continues to operate in that mode until the battery voltage has dropped below the regulation value again.

The batteries used for testing have a capacity ($C = 12\text{Ah}$) and the maximum charge current recommended by the manufacturer is $0.30C$, which is equivalent to 3.6A .

The battery charging algorithm was implemented and the performance of the MPPT battery charger is demonstrated in the Figure 4-16.

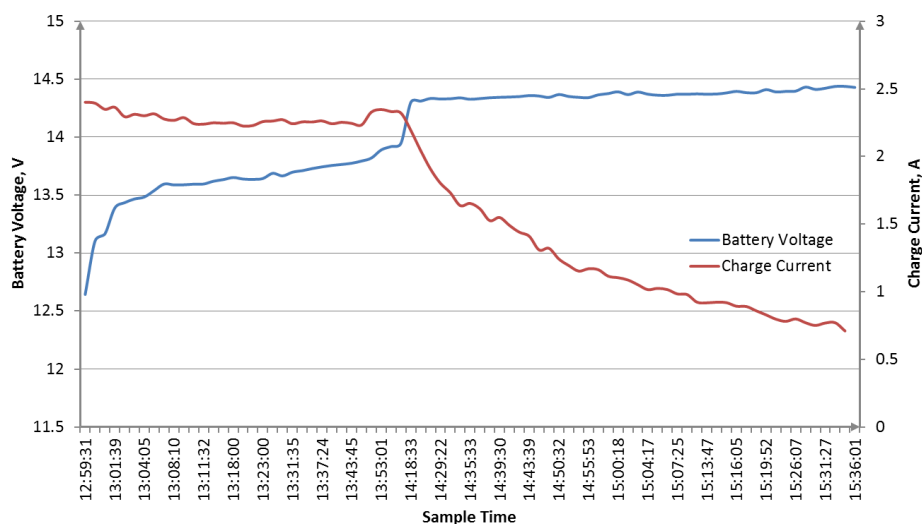


Figure 4-16: Battery Charging and Control results.

The battery charging curve in Figure 4-16 is very close to the theoretical one in Figure 4-15. Small fluctuations are observed which can be attributed to the change in irradiance and the logging frequency.

4.4.3 Measurements Accuracy

The MPPT battery charger is capable of measuring its input characteristics (voltage and current of the solar panel) as well as the output characteristics (battery voltage and charge current).

The operating duty cycle is calculated directly using the measured voltages and currents. Therefore, accurate measurements are crucial for accurate MPP tracking. Due to switching noise, single measurements were not reliable enough as they caused large fluctuations which led to unstable tracking. This challenge was overcome by taking multiple measurements and averaging. The averaged measurements were then used to calculate the operating duty cycle which resulted in a more accurate and stable tracking.

The multiple measurements (10) approach has increased the measurement time which also resulted in more computation time. Nonetheless, this compromise is worth the achieved results.

4.4.4 Communication Effectiveness

The MPPT battery charger was operated through the respective Modbus commands (see Modbus documentation in Appendix B) and all test data was recorded using the Modbus commands. The communication was fairly effective, no errors or lost data were encountered. In fact, all the Modbus commands tested have performed as expected.

The communication speed was tested across the entire baud rate spectrum (2400-115200) and no errors were experienced.

4.4.5 Efficiency

The efficiency of the MPPT battery charger varies depending on the operating duty cycle and consequently operating voltages and currents. The duty cycle was manually changed from 32-80% with a 12V battery connected on the output and the operating characteristics were recorded to calculate the efficiency.

The efficiency of the MPPT battery charger at different duty cycles is shown in Figure 4-17, while the test data can be seen in Appendix D.

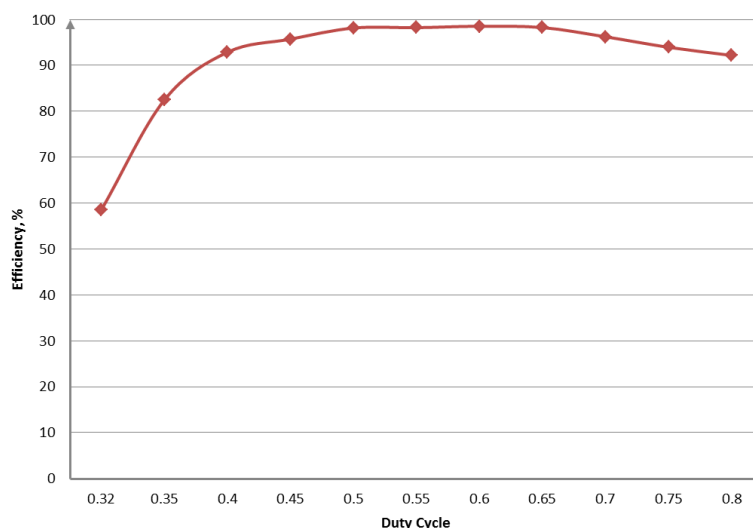


Figure 4-17: MPPT Efficiency vs Duty Cycle.

The MPPT battery charger was found to be more efficient at duty cycles of 50-65% when the efficiency of around 98% was recorded. The lowest efficiency recorded was 58% at the duty

cycle of 32% which is the lowest possible operating duty cycle for this particular combination of test panels and battery.

The efficiency is expected to be slightly lower at the same duty cycles but for higher currents as the inductor and MOSFETs conduction losses would increase with the increase of load current.

4.4.6 Conclusion

The MPPT battery charger has achieved its major design objectives. It accurately and quickly tracked the MPP and maintained its operating point at MPP with minimum oscillations. It accurately executed the charging algorithm and control routines, and it has charged the battery depending on its state of charge.

The MPPT battery charger demonstrated effective communication capabilities. It handled all the Modbus requests as expected, where data sizes of up to 100 bytes were successfully transmitted.

The tracking instability discussed earlier was resolved by reducing the tracking frequency to 5 Hz and by using averaged measurements to calculate the duty cycle. This solution is a compromise between reaching the MPP faster and achieving higher measurement accuracy. However, a frequency of 5 Hz is still fast enough for MPP tracking. On the other hand, low tracking frequency has allowed sufficient time for measurements and computation of the algorithm routine to complete without interruptions.

Stable tracking also reduced the effect of switching noise on measurement accuracy especially the noise due to fluctuations around the MPP.

It is evident from the test results that this MPPT battery charger can achieve high efficiency (up to 98 percent) depending on its operating duty cycle.

The developed MPPT battery charger is equipped with LEDs for easy debugging and to indicate its different operating status; including presence of power, charging status and communication LEDs to indicate when data transmission is in progress.

All of these features and capabilities make this MPPT battery charger suitable for our research objective.

CHAPTER 5 ACTIVE LOAD DESIGN

5.1 Overview

The purpose of the Active Loads is to ensure that the two test solar panels are operated at their respective MPP all the time. The Active Load is an intelligent device that varies its input resistance depending on the available power.

The power generated by the solar panels at any time is either used to charge the battery through the MPPT battery charger or dumped through the Active Loads. For that purpose, there is an Active Load connected on each solar panel as shown in Figure 5-1.

The principle of operation of the Active Load is discussed in section 5.2.

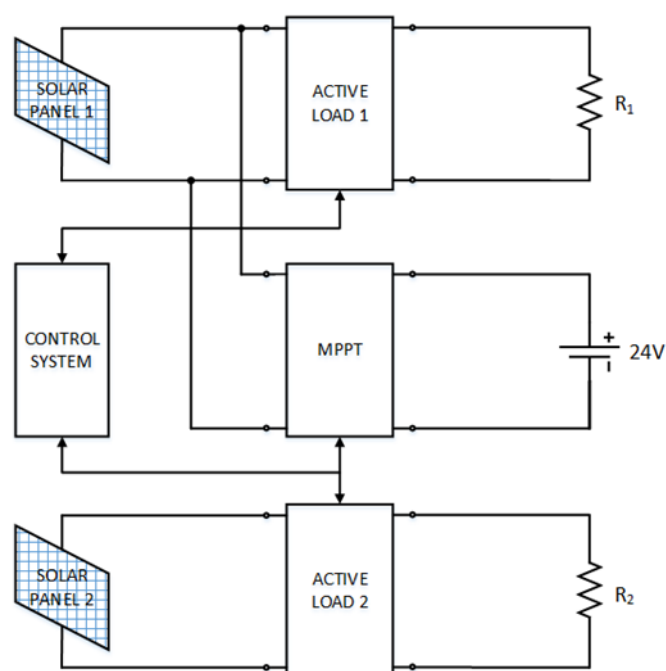


Figure 5-1: Block diagram of the station with two Active Loads included.

The Active Load circuit is shown in Figure 5-2. Its main components are the two filter inductors (L1, L2) and two filter capacitors (C1 and C2), a short-circuiting switch (Q1), synchronised switching MOSFETs (Q2 and Q3), a freewheeling diode, a single channel gate driver (IR2117), a dual channel gate driver (IRS2104), and the microcontroller (Atmega328).

The Active Load PCB also houses other circuits not indicated in this figure, namely the power supply, measurement circuitry, RTC, Micro SD card and communication circuitry. See Appendix G for the detailed schematics and PCB layout of the Active Load.

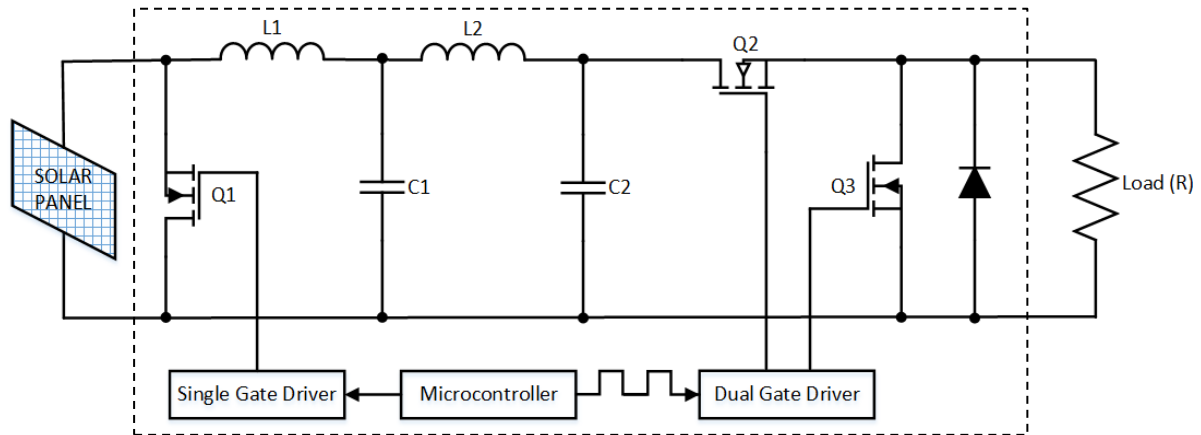


Figure 5-2: Active Load Simplified Circuit.

5.2 Principle of Operation

The Active Load is designed based on the principle of a DC-DC switch mode converter for power control. By controlling the duty cycle, the power delivered to the fixed dumping resistor (R_{out}) can be varied. This results in a virtual variable load as explained with the equations below.

The output voltage (V_{out}) and input voltage (V_{in}) of the Active load are related as:

$$V_{out} = DV_{in} \quad (5-1)$$

The output power of the Active Load can then be expressed using the relationship:

$$P_{out} = V_{out}I_{out} = DV_{in}I_{out} \quad (5-2)$$

If the power losses in the Active Load are neglected, $P_{in} = V_{in}I_{in} = P_{out}$, so the average output current can be expressed as a function of the duty cycle:

$$I_{out} = \frac{I_{in}}{D} \quad (5-3)$$

The output resistance of the Active Load as seen from the source therefore has a variable value expressed as:

$$R_{out} = \frac{V_{out}}{I_{out}} = \frac{D \cdot V_{in}}{\left(\frac{I_{in}}{D}\right)} \quad (5-4)$$

$$= D^2 \frac{V_{in}}{I_{in}} = D^2 R_{in}$$

$$\Rightarrow R_{in} = \frac{1}{D^2} R_{out} \quad (5-5)$$

It is evident from equation (5-5) that by controlling the value of the duty cycle (D), the load seen by the source can be increased or decreased depending on the amount of energy that needs to be dumped. The amount of power supplied to the dumping resistor is controlled automatically by the microcontroller in the Active Load using an algorithm to vary the switching duty cycle.

5.3 Active Load Hardware Design

This section looks into the design of the Active Load's PCB and all major component selections are clarified where necessary.

5.3.1 Design Parameters

Like in the design process of the MPPT battery charger, numerous design and operating parameters have to be fixed based on the operation requirements. The main function of the Active Load is to operate the panel(s) at MPP at any specific moment by dumping the power to the dumping resistor.

Secondly, the Active Load is also used to derive the I - V curve of the panel at any moment when required. The I - V curve derivation process is discussed in section 5.3.5.

The Active Load design parameters are listed in Table 5-1.

Table 5-1: Active Load Design Parameters.

Parameter	Value
Maximum Input Voltage (V_{in})	100 V or 50V
Maximum Input Current (I_{in})	5A/100V or 10A/50V
Switching Frequency (f_s)	40 kHz
Dumping Resistor	1 Ω , 350W

5.3.2 Current Measurement

The shunt resistor method is used for the current measurement in exactly the same manner as it was implemented in the MPPT battery charger. See section 3.5.1 for more details on this method, its advantages and its implementation.

The Active Load is designed to measure currents up to 10 A and an appropriate gain is set for the instrumentation amplifier (INA111) that would produce about 5 V at the output of the amplifier during maximum current flow.

5.3.3 Voltage Measurement

The potential divider method which was employed in the MPPT battery charger for voltage measurement is also applied here in the same manner as explained in section 4.2.4. Refer to the mentioned section for elaboration on this method and its implementation.

5.3.4 Capacitor and Inductor Selection

To determine the inductance and capacitance values for the Active Load, different combinations were selected and simulated in SIMPLORER Simulation Center. Different inductor and capacitor values (based on availability) were simulated at different duty cycles until practically desired results were achieved.

The circuit used to simulate the Active Load in SIMPLORER Simulation Center is presented in Figure 5-3.

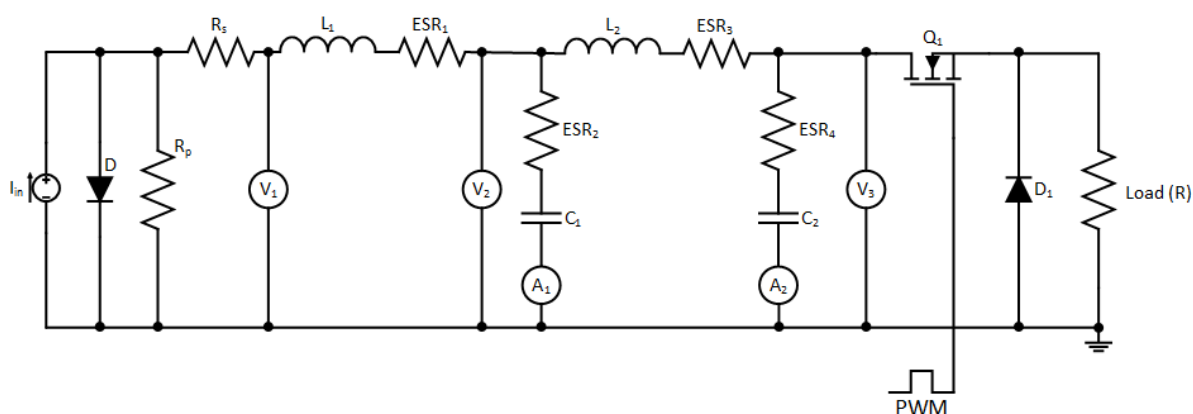


Figure 5-3: Active Load Simulation Circuit.

Based on simulation results, the desired results can only be achieved with a double LC filter stage. The first filter stage is made up of a ferrite core inductor (EE30) with the inductance

value of $10\mu\text{H}$ (L_1) and two $470\mu\text{F}$ (C_1) electrolytic capacitors in parallel. The second stage is made up of the same inductor (make and inductance value) (L_2) and four polyester film capacitors (C_2) in parallel of $10\mu\text{F}$ each.

The polyester film capacitors were selected due to their much lower equivalent series resistance (ESR) and therefore high ripple current handling capability (about three times compared to electrolytic capacitors).

The simulation results are presented in figures below. Figure 5-4 shows the input characteristics (voltage and current) of the Active Load. This figure shows that the ripple voltage and currents are smoothed out by the filters and they are not affecting the solar panel.

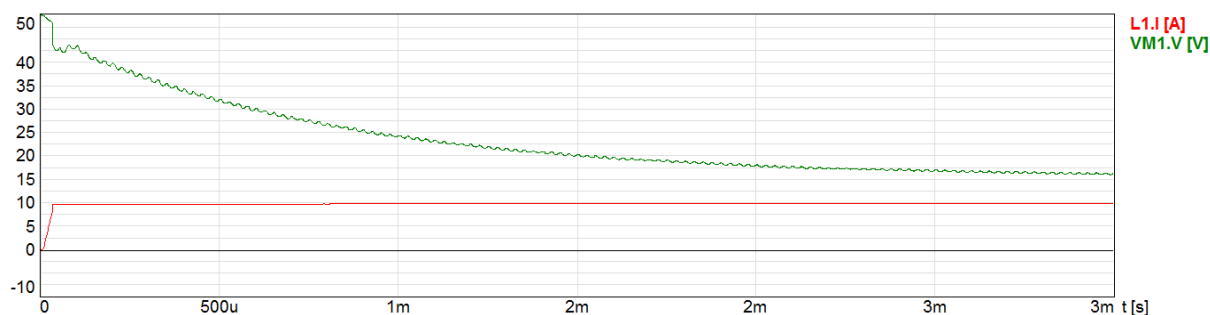


Figure 5-4: Input current and voltage of the Active Load.

Voltage and current waveforms after the first filter stage are shown in Figure 5-5. At this stage small current and voltage ripples are still present.

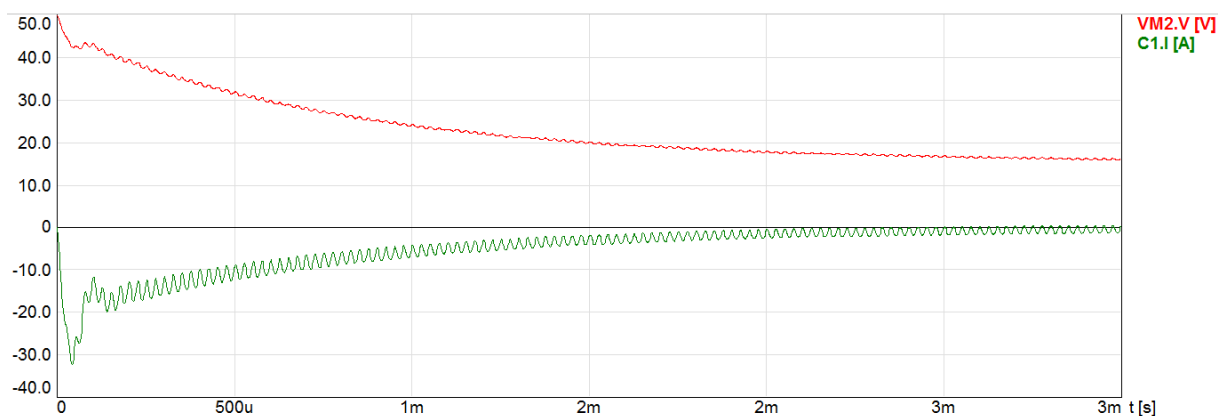


Figure 5-5: Voltage and current after the first filter stage.

The voltage and current after the second filter stage are shown next in Figure 5-6. At this stage, high ripple currents are observed. The polyester filter capacitors (C_2) have to handle the ripple currents of about 35 A peak-to-peak. For this reason, four parallel polyester capacitors have to be employed.

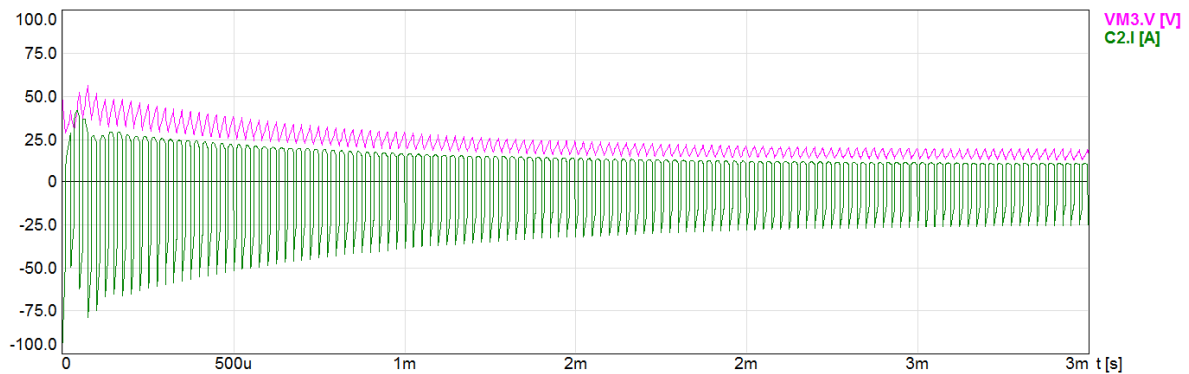


Figure 5-6: Voltage and Current after the second filter stage.

In Figure 5-7, switching waves of the maximum load current is shown. This is the worst case current, when the input voltage is 50 V and the input current of 10 A.

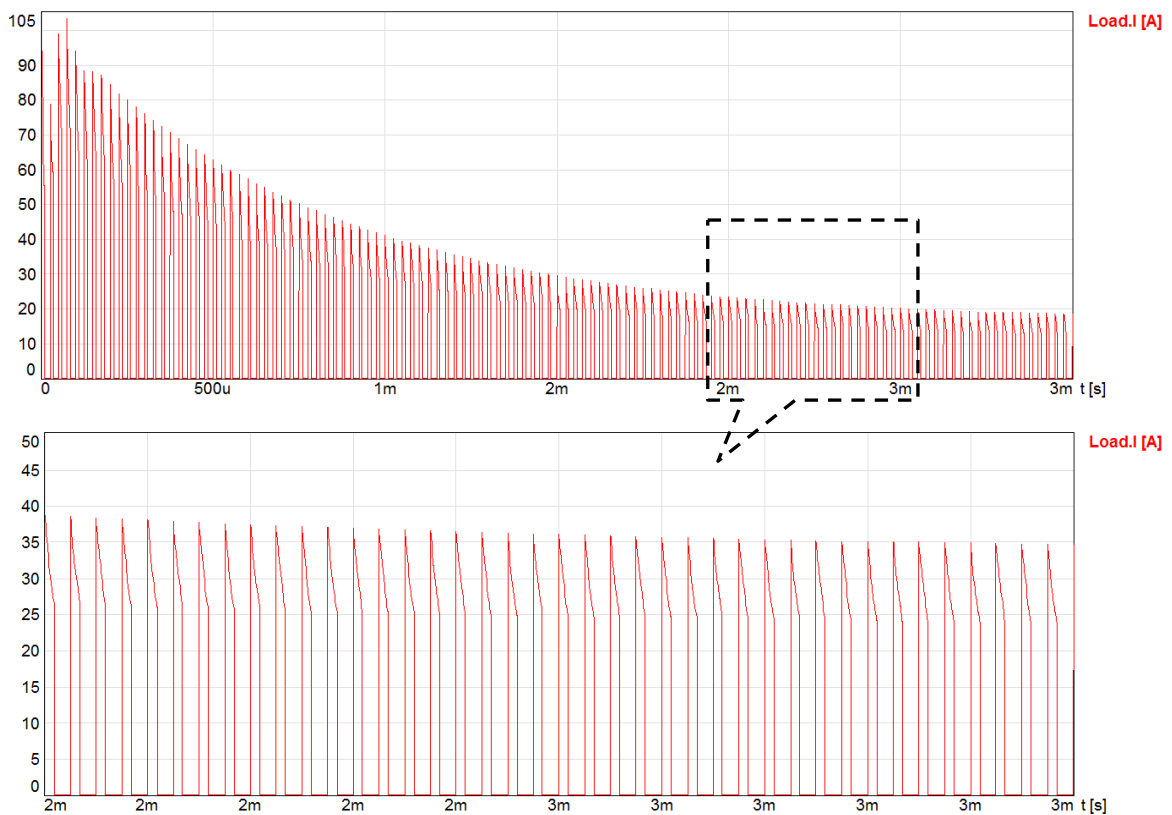


Figure 5-7: Active Load simulation results showing maximum load current switching waves.

5.3.5 Dumping Resistor

The Active Load dissipates the power from the solar panel through the dumping resistor connected on its output. The selected dumping resistor is a high power wire wound resistor with a resistance of 1Ω and up to 350W power dissipation capability as shown in Figure 5-8.

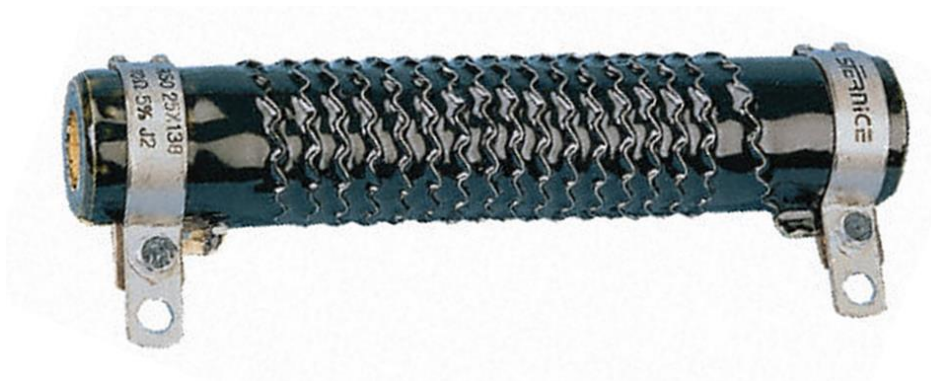


Figure 5-8: Selected dumping resistor, 1Ω 350W [RS Components].

For the prototype, one resistor is used for each Active Load. Two or more dumping resistors can be connected in parallel when monitoring panels with power greater than 350W.

5.3.6 Power Supply

The power supply of the Active Load is also from the 12V/24V battery (batteries). The power supply approach for this device is similar to the approach employed in the MPPT battery charger.

For more details, see the Active Load schematics attached as Appendix G.

5.3.7 PCB Design

A picture of the Active Load is shown in Figure 5-9.

The outlined circuitries are: (1) Buck Converter (input capacitors, heatsink, inductors and output capacitors), (2) the measurement circuitry, (3) power supply circuitry, (4) Real Time Clock, (5) Micro SD card, (6) microcontroller circuitry, and (7) the communication circuitry.

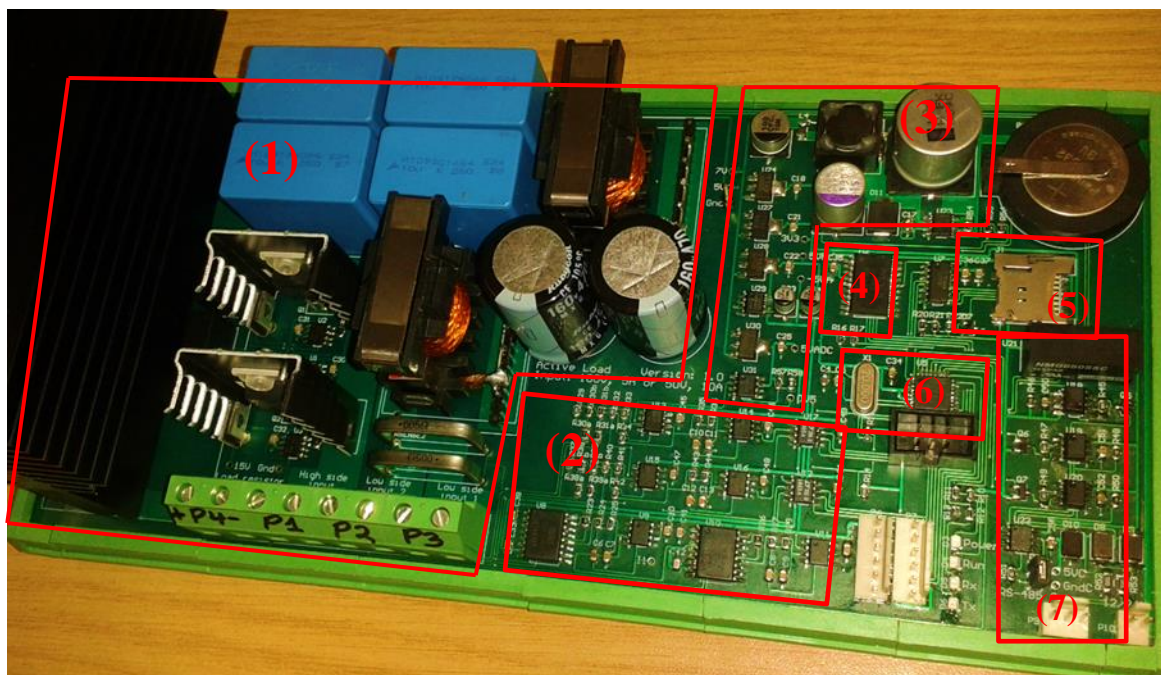


Figure 5-9: The picture of the Active Load.

5.4 Software Design

The firmware was developed for the peripherals of the microcontroller and/or functions (PWM generation, communication, RTC, and ADC calibrations). Most of the programming is also applicable to the MPPT battery charger, with few exceptions as discussed in the next sections.

Parts of the firmware development (RTC reading and setting, PWM generation process and switching frequency settings) were implemented exactly as in the MPPT battery charger. The USART communication software settings were also implemented in the same manner although Modbus commands have been developed for each specific device.

5.4.1 Calibration

As explained earlier, calibration needs to be done at least once for each device and for each measurement channel before a device can be operated.

The flow diagram of the calibration procedures is presented in Figure 5-10 and briefly explained thereafter.

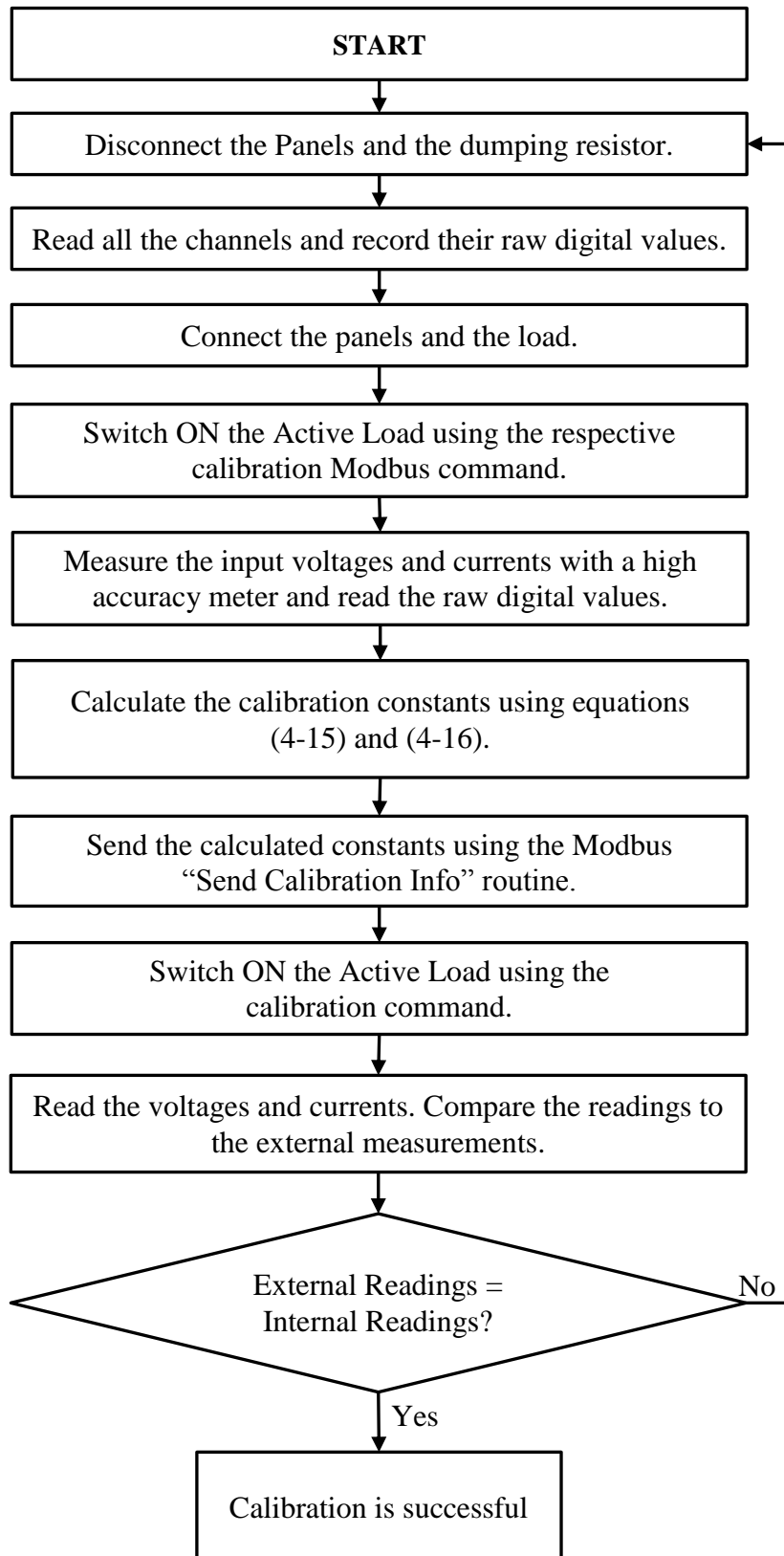


Figure 5-10: Active Load Calibration procedures.

Calibration starts with reading the raw offset digital values of all channels before the PV panels and the dumping resistor are connected. In the next step, the panel(s) and the dumping resistor are connected on their respective ports, and the Active Load is switched on through a calibration Modbus command with a fixed duty cycle. The fixed duty cycle must be used because the Active Load cannot run the algorithm before calibration.

When the Active Load is in calibration mode, voltage and current values are measured externally while their respective raw digital values are recorded using the device. After that, the respective constants are calculated using equations (4-15) and (4-16).

The calculated constants are then sent to the device using the respective calibration command and they are stored in the non-volatile memory of the microcontroller. The next calibration step involves further measurement samples to verify whether the calibration was successful.

5.4.2 P&O Algorithm

After successful calibration, the device can now run in MPPT mode executing the P&O algorithm. The algorithm was implemented according to the flow chart in Appendix C. The duty cycle step and tracking frequency were also determined through trial and error until optimum values were achieved.

Testing and implementation results are presented in the next sections.

5.5 Testing and Results

As with the MPPT battery charger, operation of the Active Load was tested with two Solara 55W panels in different configurations (series and parallel) and a variable dumping resistor set at 1Ω . The test results are discussed below.

5.5.1 Experiment Setup

Each Active Load can accommodate up to two solar panels connected either in series or parallel, provided that such a combination does not exceed the rated operating conditions of the devices.

The active load can therefore be operated in three configurations as outlined below.

1. One panel is connected on port P1 (Refer to Appendix G) while port P2 is short-circuited and port P3 is left open. In this configuration the voltage and current are measured for that specific panel.
2. Two panels are connected in series on port P1 and port P2 while port P3 is left open. In this configuration, two voltages (for each panel) and their common current are measured.
3. The third configuration is when two panels are connected in parallel on port P2 and port P3 while port P1 is short-circuited. In this configuration, the current generated by each panel is measured as well as their common voltage.

In this experiment the two test solar panels were externally connected in series before being connected to a specific port for different tests and calibrations.

The circuit used to test the operations of the Active Load is shown in Figure 5-11.

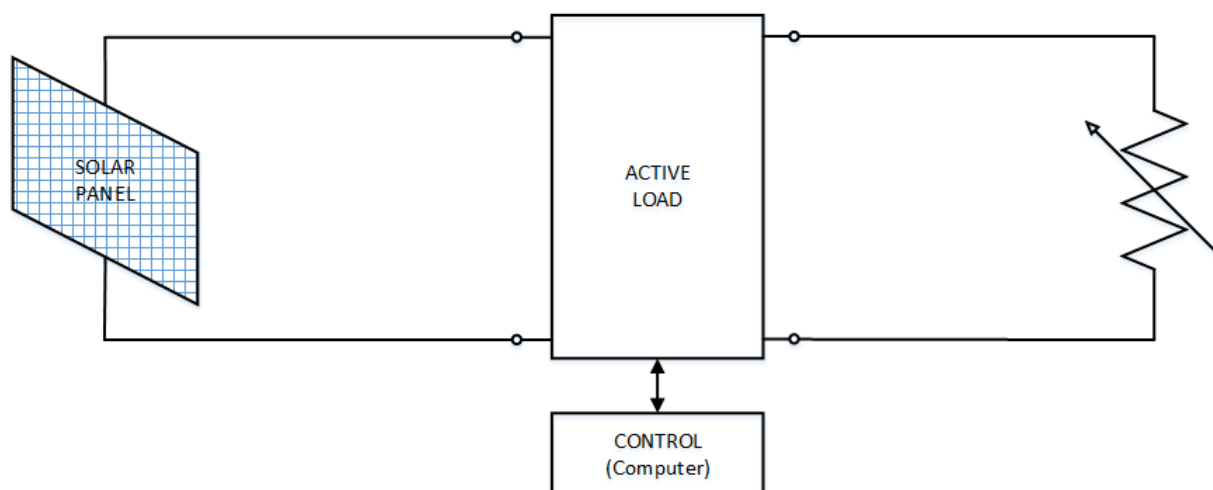


Figure 5-11: Active Load Test Circuit.

5.5.2 Algorithm Performance

Test results recorded on the 8th of October 2014 are presented in the figures. The weather on that particular day was good for the dynamic response test because it was partly cloudy.

The graph shown Figure 5-12 demonstrates a fairly stable tracking and a reasonable dynamic response as the Active Load accurately reacted to a change in PV input characteristics due to cloud cover. The device adjusted its duty cycle and successfully found the new MPP. It also quickly recovered to the new MPP when it was no longer covered.

Duty cycle fluctuations are also observed after the cloud cover as the algorithm attempts to stabilise at the new MPP.

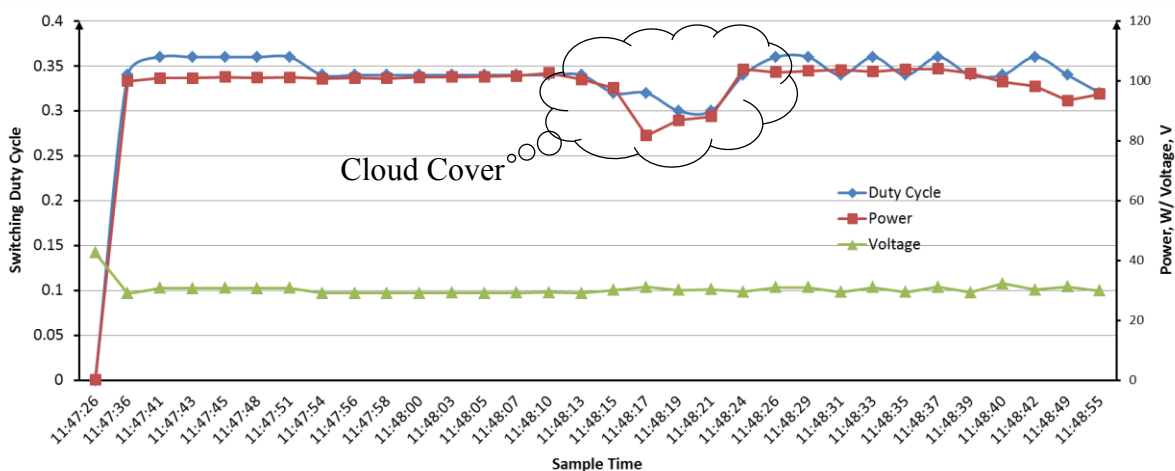


Figure 5-12: Active Load Test Results – PV Power, PV Voltage and Switching Duty Cycle.

The influence of the cloud cover on the PV current and consequently on the power is presented next in Figure 5-13.

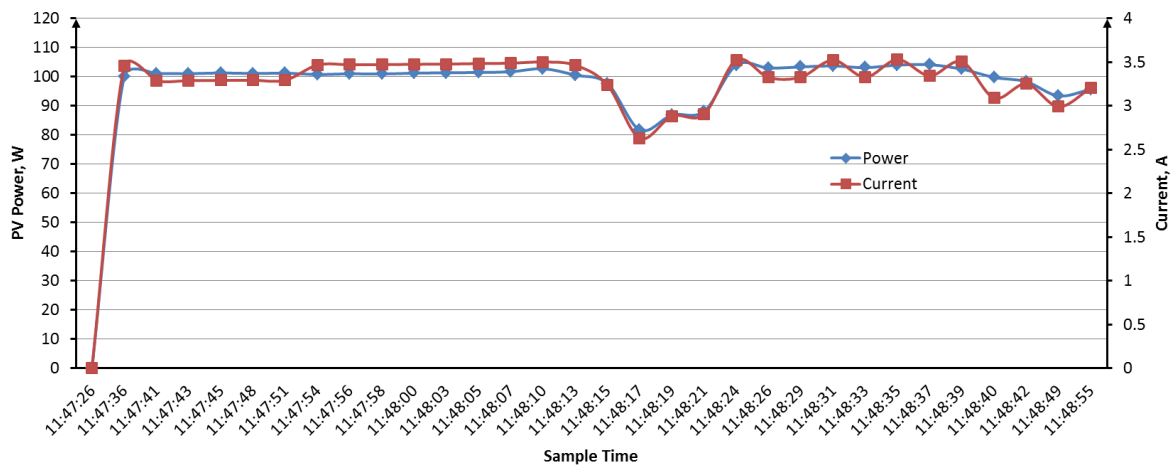


Figure 5-13: Active Load Test Results – PV Current and PV Power.

The graph above shows a sharp drop in input (PV) current and consequently power as a result of low irradiance reception caused by the cloud cover. Furthermore, the fluctuations are observed on the current which can be, as mentioned earlier, due to the algorithm recovery and stability around the MPP during fast irradiance changes.

The Active Load was also tested on a sunny and clear sky afternoon on 10 November 2014 and 50 samples were recorded over a period of about one hour. The results for that particular day are indicated in Figure 5-14.

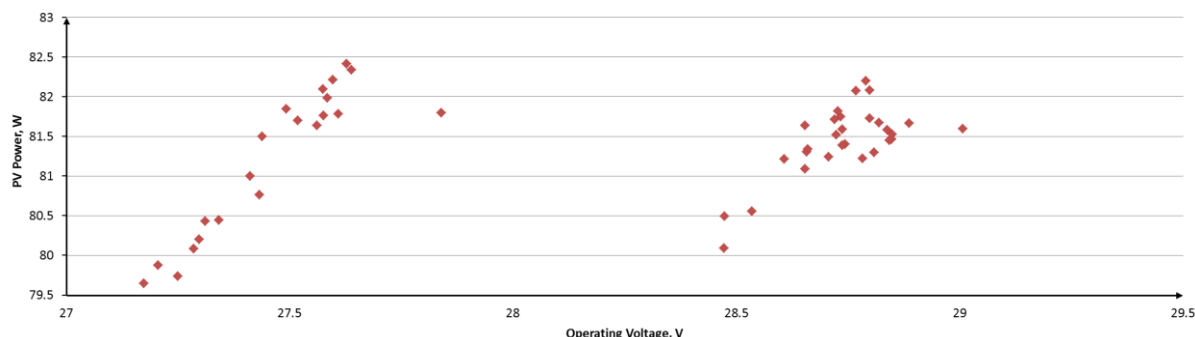


Figure 5-14: Active Load test results showing fluctuations of the operating voltage.

Figure 5-14 shows the distribution of the Active Load’s operating point after stabilisation. The operating voltage is fluctuating around the MPP within about 1V margin, between 29-30V, while power only fluctuated within a 2W margin between 76-78W.

It can also be seen in the next figure (Figure 5-15) that the duty cycle fluctuated only between 0.252-0.258 over the observation period. This fluctuation is negligibly small when compared to the fluctuations observed in the previous test. It can as well be observed that the duty cycle remained unchanged for most part of the sampling time, which is a sign of stable MPP tracking as expected during clear sky days.

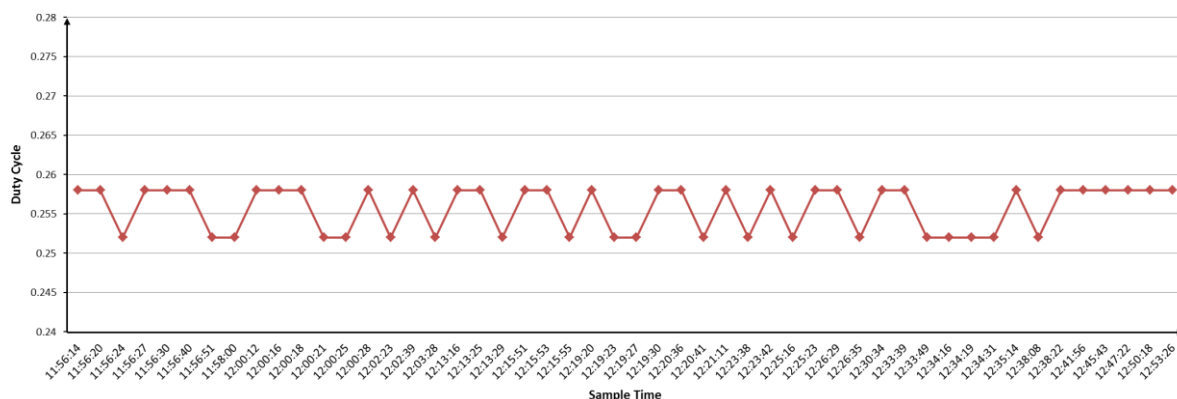


Figure 5-15: Active Load Test Results showing Duty Cycle fluctuations.

It is, however, difficult to conclude without doubt whether the fluctuations in both of these experiments are only a result of the change in irradiance levels. Irradiance measurement is recommended to understand this issue further.

5.5.3 IV Curve Derivation

The $I - V$ curve can be derived for each configuration (refer to section 5.5.1) by executing a routine that varies the duty cycle over a certain range starting with the open circuit characteristics. For each duty cycle change, the voltage and current are measured and recorded for transmission to the Control System. This data can then be used to draw the $I - V$ curve of the test panel.

Figure 5-16 below shows an $I - V$ curve that was derived using the Active Load on 12 November 2014. See the actual data received from the device in Appendix H.

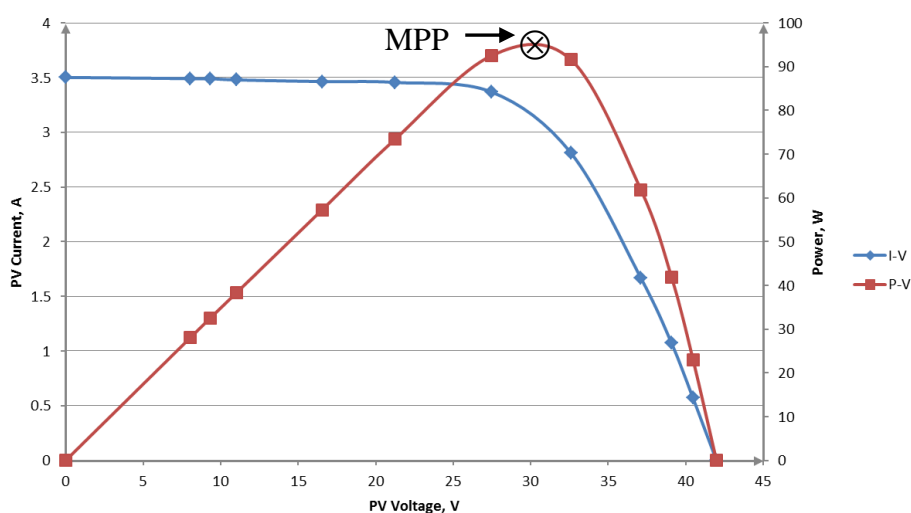


Figure 5-16: Active Load test results showing the derived $I - V$ curve.

The roughness seen on the $I - V$ curve is caused by large step changes (0.05) in the duty cycle. For a smoother curve (more accurate), smaller steps can be used (0.01, for instance) but they would demand more quick successive measurements to be done and more data (bytes) to transmit. The above curve is plotted out of 12 points which are a result of 24 measurements and 149 bytes had to be transmitted.

5.5.4 Measurement Accuracy

The Active Load achieved better measurement accuracy as compared to the MPPT battery charger, which can be due to a combination of several reasons.

First, the influence of switching noise was reduced as a result of improved PCB layout and the implementation of a double L-C filter. Second, the Active Load's calibration process is

much easier since it has a separate power supply point; supply voltage and current are not included in the measured value, which is not applicable to the MPPT battery charger.

For high tracking reliability, averaged measurements were used to perform the tracking algorithm.

5.5.5 Communication Effectiveness

The communication was tested with various Modbus commands. The Active Load demonstrated effective communication; no errors or data losses were experienced. All the Modbus commands (see Modbus documentation in Appendix E) were tested and they performed according to expectations.

The Active Load was operated through the respective Modbus commands and all the test data was successfully recorded using Modbus commands. The communication was also tested over a wide range of baudrates (2400-115200 bits per second (bps)) and no issues were noticed.

5.5.6 Conclusion

The Active Load has accurately operated the test panels at MPP throughout the test period as expected. It instantly and stably tracked the MPP and it dynamically responded well to any change on its input conditions.

The Active Load's communication was tested with several Modbus commands. All the Modbus requests were handled well and no errors were detected.

After implementing a tracking frequency of 5 Hz, minor oscillations were still being observed around the MPP. This should be expected from this algorithm. During sunny days, the size of fluctuations is however negligible to the extent that it did not cause large swings in the PV output power.

The Active Load successfully derived the $I - V$ curve indicated in Figure 5-16 through a Modbus Command. More accurate $I - V$ curves can be derived by using smaller step changes in the duty cycle. That will however demand more measurements to be made and eventually more data to transmit. On the other hand, too many successive measurements can overload the microcontroller, so a compromise is necessary.

The Active Load automatically detects how the panels are connected (series or parallel) and subsequently which measurement channels to employ for tracking. The connection type can only be detected when there are panels connected and switched on. Otherwise a 'no panels connected' error is reported.

The Active Load is also equipped with status LEDs to indicate presence of power and other functions like data transmission and tracking process.

This Active Load is therefore suitable enough for our research purpose.

CHAPTER 6 THE STATION

6.1 Overview

This chapter discusses the mechanical structure of the station and the assembling of its different components into a functioning unit. The organization of all the devices in the station is also presented.

The station consists of the two solar panels. Each solar panel is connected to the dumping resistor through an Active Load. The cleaned panel is shared by the Active Load and the MPPT battery charger. The three (two Active Loads and the MPPT battery charger) are all connected to the control system. The operation of the station is explained in detail in the next sections.

The simplified architecture of the station is shown in Figure 6-1 below.

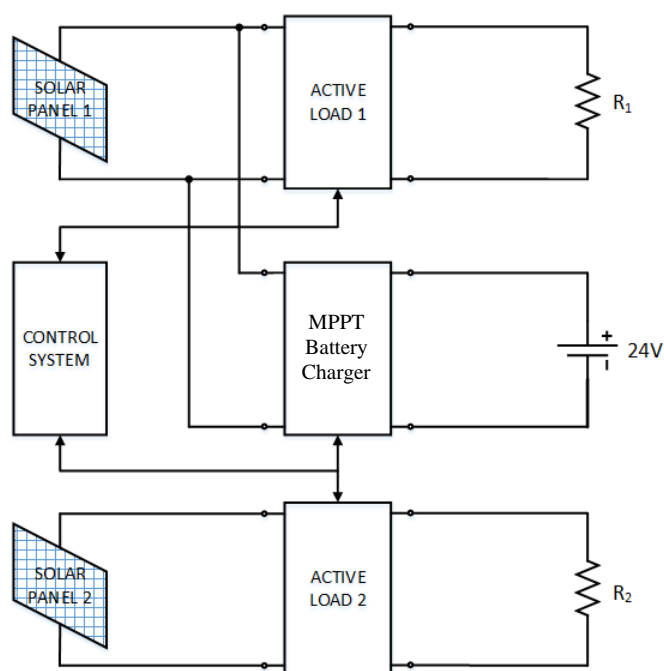


Figure 6-1: Figurative Architecture of the Station.

6.2 The Layout

The station's physical layout is made up of a mechanical structure which holds the two panels and the component's enclosure in place. The station was assembled and connected according to the circuit configuration presented earlier in Figure 6-1.

The panels are mounted two meters above the ground (height of the mechanical structure) as shown in Figure 6-2. The mechanical structure allows for easy and precise adjustment of the panel's tilt angle which provides an opportunity for easy panel orientation and monitoring at different tilt angles when necessary.

Batteries and all the electronic equipment are housed in a weatherproof enclosure. The enclosure of the components is located under the panels which provides shading for most part of the day and protect the electronic equipment from direct sunlight exposure and high ambient temperatures.



Figure 6-2: The picture of the station as mounted on the roof (Front View).

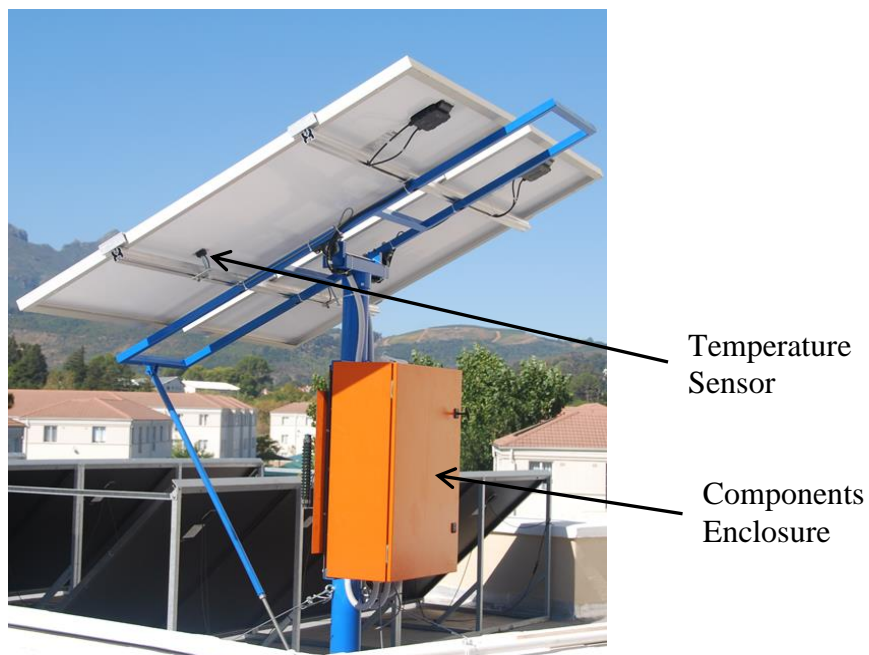


Figure 6-3: The picture of the station as mounted on the roof (Back View).

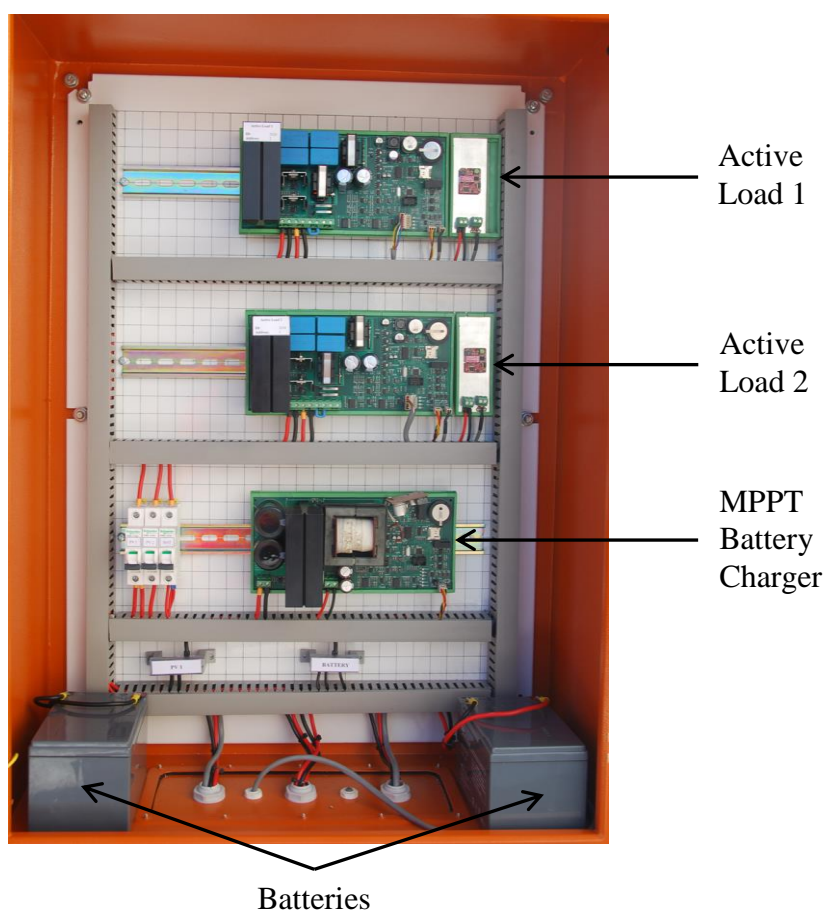


Figure 6-4: Inside the enclosure.

6.3 Preliminary Settings

This section describes the initial settings and preparations before the station can be operated. These include setting the time, giving all the devices appropriate addresses or identification numbers, doing all the calibrations and setting the communication baudrates.

6.3.1 Device Address and Baud Rate

The first thing necessary for the station to operate is proper communication between the Control System and all other devices. Every communication starts with the address of the device that is being addressed and the communicating devices must do so at the same baudrate.

All the devices are programmed with a specific device address. The device address for each device must be verified and noted during programming. The address of any device can however be changed anytime when necessary using the respective Modbus Command. Careful consideration must be made to ensure that no devices are sharing the same address, to prevent communication errors caused by two devices responding to the same request.

All the devices are programmed with the default baudrate of 9600 bps. However the operator can set any baudrate if there is a need for that. Each device has a specific Modbus command for setting either the baudrate, device address or both.

6.3.2 Time

Both the MPPT battery charger and Active Load are equipped with RTCs. The time of the respective device is set by sending the time settings using the dedicated Modbus Command. The Modbus Commands documentations for the two devices are attached as Appendix B and E. Once the time has been set, RTC ICs keep their time settings accurately over a long period of time.

6.4 User Interface

The Control System serves as the interaction tool between the user and all other devices of the station. The user or operator utilises the Control System to perform all the settings and operations of the station.

The Control System runs/executes python scripts to communicate with the devices and to interpret the received data. A more friendly and interactive graphical user interface is recommended in the future.

6.5 Operation Schedule and Coordination

Although the initial plan was to use the power generated by the panels only to charge the batteries through the MPPT battery charger, it emerged that the batteries used in the station do not have the capacity to consume all the power generated by the panels throughout the day. It is therefore much better to employ the Active Loads to always keep the panels loaded and operating at MPP while the MPPT battery charger will only be used to charge the batteries.

One important aspect is that, the MPPT battery charger and the Active Load connected on the same solar panel should not be switched on at the same time. This will avoid a conflict that could happen when each device attempts to operate that solar panel at the MPP dictated by the load connected on its output (battery or dumping resistor).

The current daily operation schedule starts by running the MPPT battery charger in the morning for one hour (07h00-07h59) and thereafter the Active Loads will be switched on from 08h00-18h00. Due to the smaller size of the batteries as well as the power rating of the panels, an hour daily allocated to charging the batteries is sufficient to keep the batteries adequately charged up.

The battery charging time can be increased if deemed necessary, especially during the rainy season.

6.6 Data Management

Data exchange is always started by the Control System (master) querying a particular device (slave) for specific information or sending instructions for that device to execute. Depending on the command, the data received from the device will either simply be displayed or logged.

6.6.1 Data Logging

When the data needs to be logged, the control system stores the received data in CSV format with its respective date and time of measurement. The operator can access the logged data for analysis and interpretation.

The data from both devices (MPPT and Active Load) is logged periodically following an automated schedule.

A micro SD card is provided on both devices as an additional and removable storage facility. The micro SD card platform is provided in the hardware for future expansion of the station's capability to log data without requests from the Control System.

6.6.2 Error Handling

Several routines are implemented to detect and handle errors or exceptions on both ends of the communication. The error detection starts by checking whether the information (raw data) was received correctly as it was sent. This is done using Cyclic Redundancy Check (CRC). A 16-bit CRC was implemented.

After CRC verification, each slave unpacks the received message to check if the address in the message corresponds to its own address or other broadcasting addresses. If the address is not recognised, no further message processing is carried out. Otherwise the message is further unpacked to check the command and prepare for the response transmission or report an error if the command is unknown or invalid.

If an error was encountered during the communication, the addressed device returns an error code that indicates the type of error encountered.

6.7 Cleaning Schedule

The purpose of the cleaning schedule is to keep the 'cleaned reference panel' always clean in reference to the other panel. The cleaning schedule depends on the research methodology or type of investigation being carried out. It is recommended that the "cleaned" panel be cleaned at least every second day throughout the investigation period. Cleaning after 18h00 is more preferable to avoid interrupting the station operation.

Any dirt or deposition on the 'cleaned panel' would lead to inaccurate results since monitoring is based on the comparison of the outputs of the two panels over a long time. To rule out all other factors, it is highly recommended to operate the two panels under exactly the same conditions with the only difference being their cleanness.

CHAPTER 7 RESULTS AND DISCUSSIONS

7.1 Overview

This chapter presents the analysis and discussions of the operation data obtained from the station during its commissioning. Unexpected challenges experienced along the project timeline are also discussed here.

7.2 Results

The station was assembled on the roof of the Electrical and Electronic Engineering Department building and it was tested for two days. Operating characteristics of the station were recorded accordingly. The first test was carried out in the afternoon of day 1 (05 March 2015, from 15h00 to 18h00) while the second one was performed in the morning of day 2 (06 March 2015, from 07h00 to 12h00).

The voltage and current of the panels were measured and recorded every 5 minutes both on day 1 and day 2 whereas their temperatures were recorded every 15 minutes on day 2 only.

7.2.1 Operation Data: Day 1

The output power of the panels on day 1 is presented in Figure 7-1. The power curves show that the algorithm has struggled to operate the panels at the MPP all the time.

The weather on this day was partly cloudy and windy which has caused instantaneous changes in the irradiance levels and eventually led to the poor performance of this algorithm especially during the first hour of the test.

The Active Loads however later managed to stabilise after 16h00 when the weather got better and they continued to operate the panels at MPP thereafter.

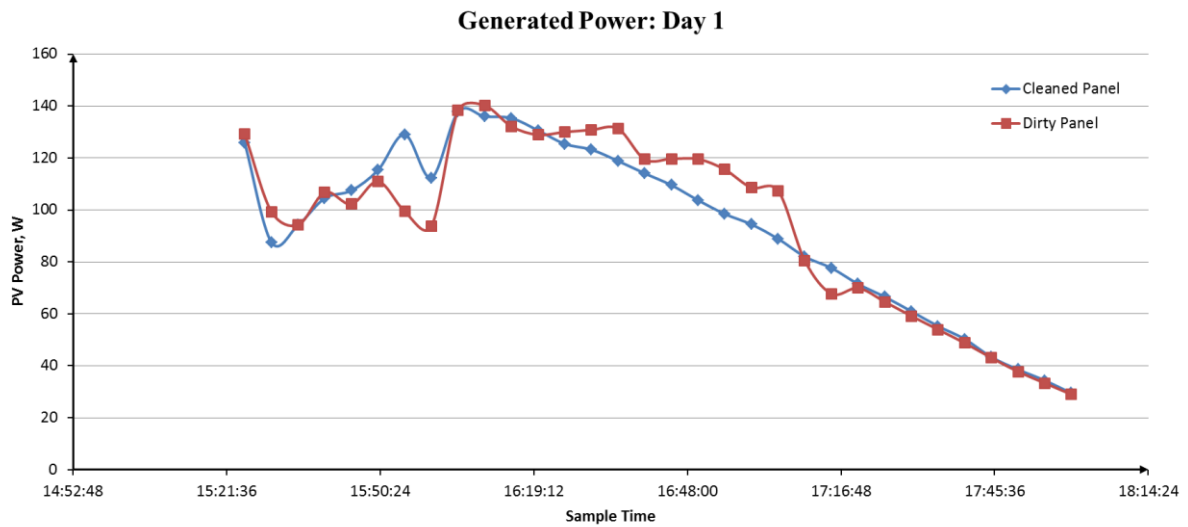


Figure 7-1: Power generated over time by both panels on day 1.

7.2.2 Operation Data: Day 2

The data recorded on day 2 of the station operation are presented in Figure 7-2 below. In this experiment, the algorithm performed quite well for about 30 minutes until the irradiance started changing (due to clouds) resulting in fluctuations and unstable tracking of the MPP. This day was also partly cloudy.

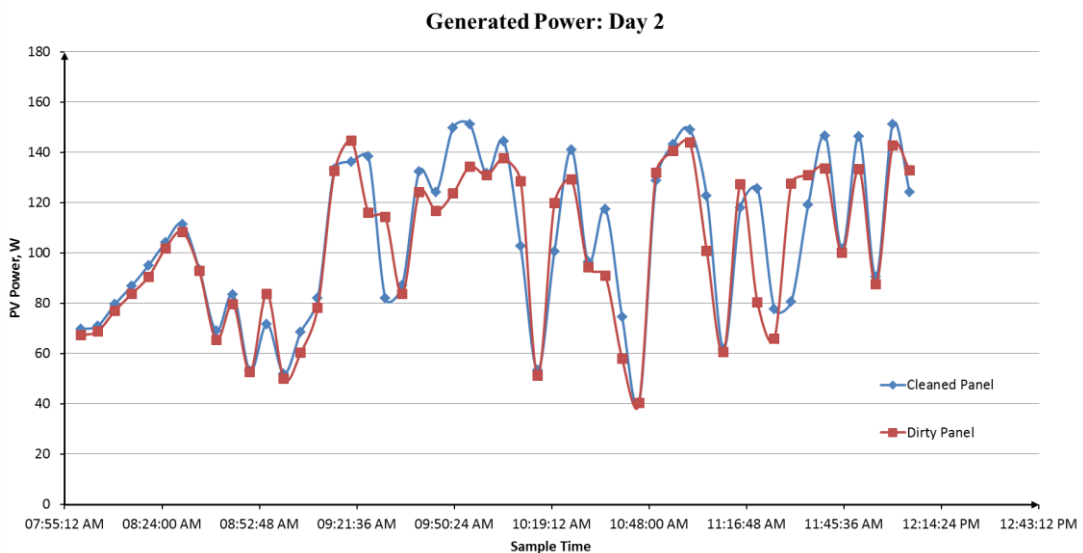


Figure 7-2: Power generated over time by both panels on day 2.

It can also be seen here, like before, that the algorithm got confused about the real MPP at some points and thus the difference in the power recorded from the two panels.

The difference in power can however also be caused by other factors. For instance, the two panels might not be covered equally by a cloud at a specific time. Additional data, like the image of the panels taken at every sampling time, might add more insight and lead to more informed conclusions.

7.2.3 Panel Temperature

The temperature of each panel was measured and recorded every 15 minutes on day 2 and they are indicated in Figure 7-4. As expected, the temperature of both panels has increased as the sun rose higher.

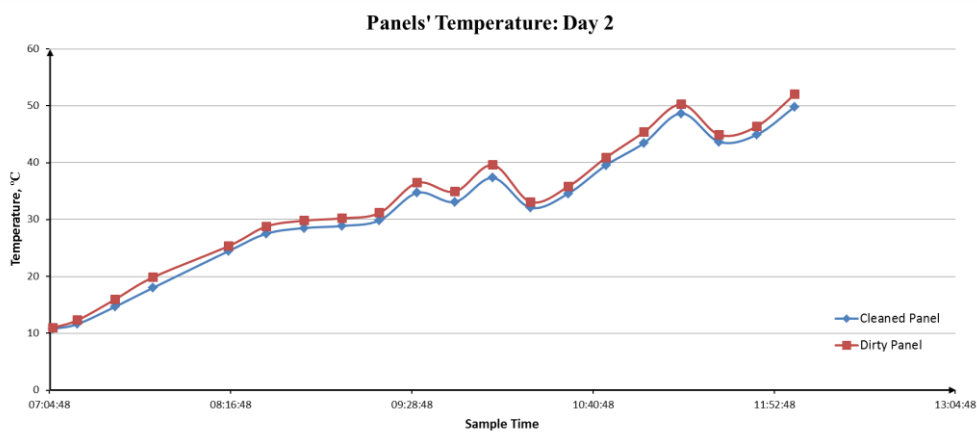


Figure 7-3: Temperatures of the panels recorded on day 2.

The effect of wind and cloud cover can also be observed on the temperatures of the panels as they caused cooling at some points as shown in Figure 7-4.

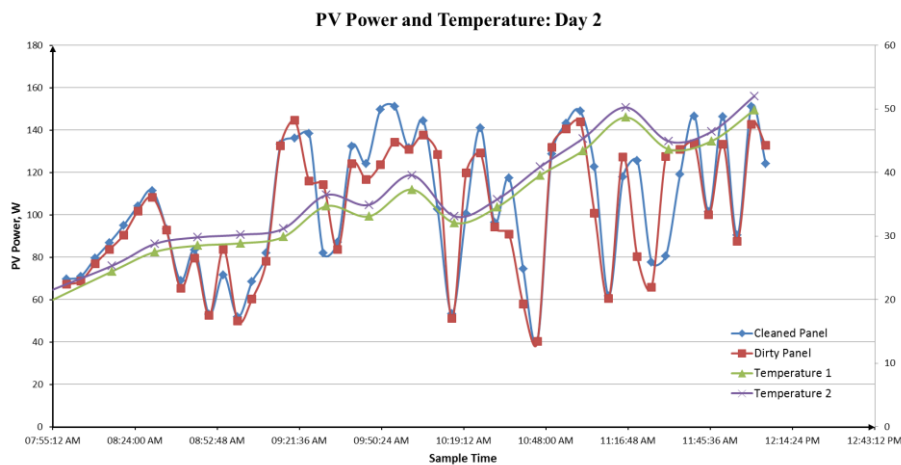


Figure 7-4: Effect of clouds on generated power and panels temperatures.

Temperatures have changed significantly at the same intervals where huge oscillations are also being observed on the power curves as seen above.

7.2.4 Battery Charging

The MPPT was operated for one hour (07h00-08h00) to charge the batteries. During this operation, the battery voltage has gone up from 24.192V to 27.125V as shown in Figure 7-5.

Charging current is also indicated in Figure 7-5. Although the charging current is expected to drop as the battery gets charged up, it is seen increasing here because the available power itself is increasing as the sun is rising and shining brighter.

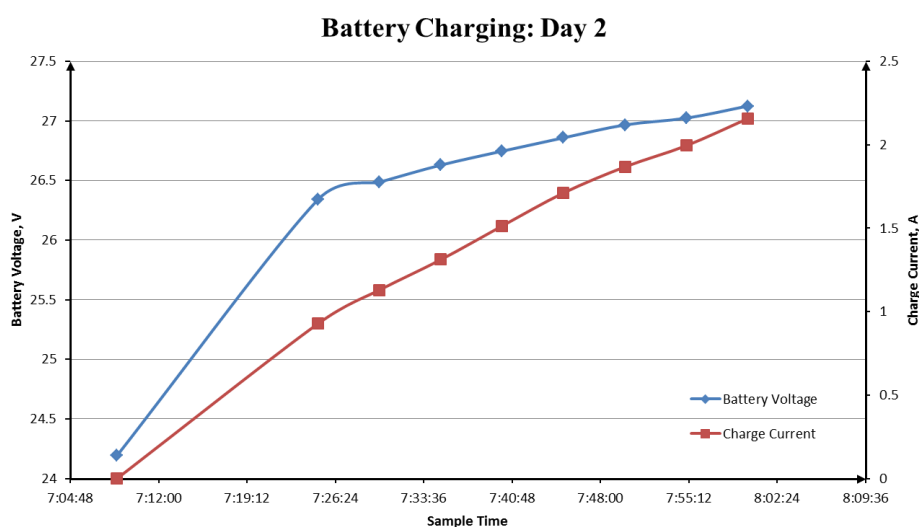


Figure 7-5: Battery Voltage and charge current on day 2.

This demonstrates that batteries will always remain charged up, since they could be charged to that level on a partly cloudy day. It also shows that one hour of charging per day is sufficient. Another charging hour could be implemented in the evening during rainy season, if found necessary.

7.3 Unexpected Challenges

The project did not run as smooth as expected both in terms of design timeline and outcomes in general. Several issues that have been experienced during the project are discussed below.

7.3.1 Microcontroller Size

The selected 8-bit AVR microcontroller was not powerful and efficient enough for the task at hand. Because of its resolution, this microcontroller is inefficient in executing the algorithms and their long mathematical computations.

Furthermore, internal ADCs of this microcontroller have a low resolution (10-bit) for this application which has necessitated the use of external ADCs. It is however inefficient for this microcontroller to read 16-bit ADCs as they have to be read as two instructions and then merge the two readings to get the actual reading. That is three instructions whereas it could be done as a single instruction in bigger microcontrollers.

A bigger and faster microcontroller (32-bit for example), with higher resolution internal ADCs, is recommended for the future versions of both devices. Numerous trade-offs can be expected from this recommendation. Microcontroller cost will be compensated by the cost of external ADCs and the power consumption will be compensated by the reduced number of computation instructions or operations.

7.3.2 Switching Noise and Measurement Accuracy

The noise generated in the switching circuits (both in the power supply circuit and the main converter) has a serious effect on the accuracy of the measurements as it affects the reference voltage of the ADCs.

Although several measures have been taken, this issue could not be completely eliminated in the hardware.

7.3.3 Components Availability Issues

The hardware development of the MPPT battery charger and the Active Load were both hampered by unavailability of components in SA.

This challenge has led to using alternative and second choice components. In some cases, even alternative components were not available resulting in long waiting periods.

CHAPTER 8 CONCLUSIONS AND RECOMMENDATIONS

8.1 Overview

This chapter provides closing remarks of this work. The chapter also highlights the recommendations that can be made to improve the station in the future.

8.2 Conclusion

A reliable platform for monitoring the effect of dust pollution on the performance of PV panels has been developed and commissioned. The prototype is based on polycrystalline PV panels, but the station can be used to monitor the effect of dust on the performance of any panel regardless of technology type.

The main role of this station is to gather data ($I - V$ Curve and other operating characteristics) in real time from the panels. The station has excelled in this primary objective. The operating characteristics of the two panels operating under the same conditions are logged at the same time. Since the panels are the same and they are operated under the same conditions, by comparing their output characteristics, we can rule out the effects of other factors and any difference can be attributed to dust accumulation.

The station will make long term data available. The analysis of such data will lead to data based conclusions regarding dust pollution. The station was tested on this capability as revealed by the results in the previous chapter.

The station is portable, easy to assemble, can operate autonomously with only cleaning required. The frequency of cleaning depends on the operator and the area in which the station is used.

All the measurement devices have micro SD card storage capability which enables the station to log data even in the absence of the Control System.

Because of the performance of the algorithm, it would be difficult to make a reasonable conclusion from the power differences alone. The IV curve can however give a better picture of the condition of the panels at any time. Daily averages of the generated power can also be used for better comparison.

To make the station more effective, further field tests are being carried out to find all deficiencies and improvements will be implemented together with some of the recommendations below in the future versions of the station.

8.3 Recommendations

The following recommendations should be considered to improve the station in the future:

- Automatic cleaning of solar panels.
- Microcontroller with higher resolution for higher computational power and better accuracy.
- Sensing other meteorological data like irradiance, rainfall, and wind speed.
- Field camera for easy detection of depositions and for remote visual inspections.
- Expansion of the communication of the station to include data access via GPRS to ease remote monitoring.
- Additional solar panel dedicated to battery charging to avoid operational conflict that that may arise if both the MPPT and the Active Load are switched on at the same.
- A more friendly and interactive user interface for the Control System that would interpret data and show reports in graphic view.

Bibliography

- [1] H. Wirth, "Recent Facts about Photovoltaics in Germany," Fraunhofer Institute for Solar Energy Systems, Freiburg, 2014.
- [2] S. Mekhilef, R. Saidur and M. Kamalisarvestani, "Effect of dust, humidity and air velocity on efficiency of photovoltaic cells," *Renewable and Sustainable Energy Reviews*, no. 16, pp. 2920-2925, 2012.
- [3] M. Mani and R. Pillai, "Impact of dust on solar photovoltaic (PV) performance: Research status, challenges and recommendations," *Renewable and Sustainable Energy Reviews*, vol. 14, pp. 3124-3131, 2010.
- [4] S. A. Sulaiman, H. H. Hussain, N. S. H. Nik Leh and M. S. I. Razali, "Effects of Dust on the Performance of PV Panels," *World Academy of Science, Engineering and Technology*, vol. 58, pp. 588-593, 2011.
- [5] M. S. Abd-Elhady, S. I. M. Zayed and C. C. M. Rindt, "Removal of dust particles from the surface of solar cells and solar collectors using surfactants," in *International conference on Heat Exchanger Fouling and Cleaning*, Crete Island, 2011.
- [6] M. Moon, "Google Studies How Dirt Affects Solar Panel Efficiency," PC Magazine, 03 August 2009. [Online]. Available: <http://goodcleantech.pcmag.com/solar-energy/279277-google-studies-how-dirt-affects-solar-panel-efficiency>. [Accessed 17 April 2013].
- [7] J. K. Kaldellis and A. Kokala, "Quantifying the decrease of the photovoltaic panels' energy yield due to phenomena of natural air pollution disposal," *Energy*, vol. 35, pp. 4862-4869, 2010.
- [8] R. Frey, D. Grafham and T. Mackewicz, "New 500V Linear MOSFETs for a 120 kW Active Load," Advanced Power Technology, Oregon, June 2000.
- [9] A. Sattar and V. Tsukanov, "MOSFETs withstand stress of linear-mode operation," Power Electronics Technology, Santa Clara, 2007.
- [10] Modbus-IDA. ORG, "MODBUS over Serial Line Specification and Implementation Guide V1.02," Modbus.org, 2006.
- [11] S. Kalogirou, *Solar Energy Engineering: Processes and Systems*, California: Academic Press, 2009.
- [12] G. M. Masters, *Renewable and Efficient Electric Power Systems*, New Jersey: John Wiley and Sons, Inc, 2004.
- [13] F. Ju and X. Fu, "Research on Impact of Dust on Solar Photovoltaic (PV) Performance," in *International Conference on Electrical and Control Engineering*, Yichang, 2011.
- [14] R. Ramabadran and B. Mathur, "Effect of Shading on Series and Parallel Connected Solar PV Modules," *Modern Applied Science*, vol. 3, pp. 32-41, 2009.

- [15] L. Dorobantu, M. O. Popescu, C. Popescu and M. Cucu, “Depositions effects and losses caused by shading on photovoltaic panels,” in *Energetics (IYCE)*, Leiria, 2011.
- [16] B. A. L. Gwandu and D. J. Creasey, “Humidity: A factor in the appropriate positioning of a photovoltaic power station.,” *Renewable Energy*, vol. 6, no. 3, pp. 313-316, 1995.
- [17] D. Goosens and E. Van Kerschaever, “Aeolian dust deposition on photovoltaic solar cells: the effects of wind velocity and airborne dust concentration on cell performance,” *Solar Energy*, vol. 66, no. 4, pp. 277-289, 1999.
- [18] J. Cano, “Photovoltaic Modules: Effect of Tilt Angle on Soiling. MSc. Thesis,” Arizona State University, Arizona, 2011.
- [19] J. H. R. Enslin, M. S. Wolf, D. B. Snyman and W. Swiegers, “Integrated Photovoltaic Maximum Power Point Tracking Converter,” *IEEE Transactions on Industrial Electronics*, vol. 44, no. 6, pp. 769-773, 1997.
- [20] M. S. Rahman, “Masters Thesis: Buck Converter Design Issues.,” Linköping Institute of Technology, Linköping, 2007.
- [21] I. Glasner and J. Appelbaum, “Advantage of boost vs. buck topology for maximum power point tracker in photovoltaic systems,” in *Nineteenth Convention of Electrical and Electronics Engineers in Israel*, Jerusalem, 1996.
- [22] N. Mohan, T. M. Undeland and W. P. Robbins, *Power Electronics: Converters, Applications, and Design*, New York: John Wiley & Sons, Inc, 1995.
- [23] Fairchild Semiconductor, *Application Bulletin AB-9: Suppressing MOSFET Gate Ringing in Converters: Selection of a Gate Resistor*, Fairchild Semiconductor, Rev 1.0.2.
- [24] D. Schelle and J. Castorena, “Buck-Converter Design Demystified,” Power Electronics, Sunnyvale, 2006.
- [25] R. W. Erickson, *Fundamentals of Power Electronics*, Boston: Kluwer Academic Publishers, 1997.
- [26] T. Eswam and P. . L. Chapman, “Comparison of Photovoltaic Array Maximum Power Point Tracking Techniques,” *Transactions on Energy Conversion*, vol. 22, no. 2, pp. 439- 449, JUNE 2007.
- [27] A. Dolara, R. Faranda and S. Leva, “Energy Comparison of Seven MPPT Techniques for PV Systems,” *J. Electromagnetic Analysis & Applications*, vol. 3, pp. 152-162, 2009.
- [28] D. Sera, R. Teodorescu, J. Hantschel and M. Knoll, “Optimized Maximum Power Point Tracker for Fast-Changing Environmental Conditions,” *IEEE Transactions on Industrial Electronics*, vol. 55, no. 7, pp. 2629-2637, JULY 2008.

- [29] T. Regan, *Application Note 105: Current Sense Circuit Collection*, Linear Technology, December 2009.
- [30] Infineon Technologies AG, *Application Note: Current Sensing Using Linear Hall Sensors*, Munich, Germany: Infineon Technologies AG, February, 2009.
- [31] S. Ziegler, H. H. C. Iu, R. C. Woodward and L. J. Borle, "Theoretical and practical analysis of a current sensing principle that exploits the resistance of the copper trace," in *IEEE Power Electronics Specialists Conference*, Rhodes, 2008.
- [32] L. Spaziani, "Design Note: Using Copper PCB Etch for Low Value Resistance," UNITRODE Corporation, Merrimack, 1997.
- [33] P. Sinha, "Hardware Conditioning of Sensor Signals," Microchip Technology, USA, 2008.
- [34] C. Kitchin and L. Counts, *Designer's Guide to Instrumentation Amplifiers 3rd Edition*, USA: Analog Devices, Inc., 2006.
- [35] C. A. Larsen, "Signal Conditioning Circuitry Design For Instrumentation Systems," Sandia National Laboratories, California, 2012.
- [36] T. Kugelstadt, *Chapter 16: Active Filter Design Techniques (SLOA088)*, Texas Instruments.
- [37] S. M. Al-Dhaheri, L. A. Lamont, L. El-Chaar and O. A. Al-Ameri, "Automated design for boosting offshore Photovoltaic (PV) performance," in *IEEE PES, Transmission and Distribution Conference and Exposition*, New Orleans, 2010.
- [38] E. Koutroulis and K. Kalaitzakis, "Novel Battery Charging Regulation System for Photovoltaic Applications," *IEE Proceedings-Electric Power Applications*, vol. 151, no. 2, pp. 191-197, 2004.

Appendices

A. MPPT PROGRAM FLOW DIAGRAMS

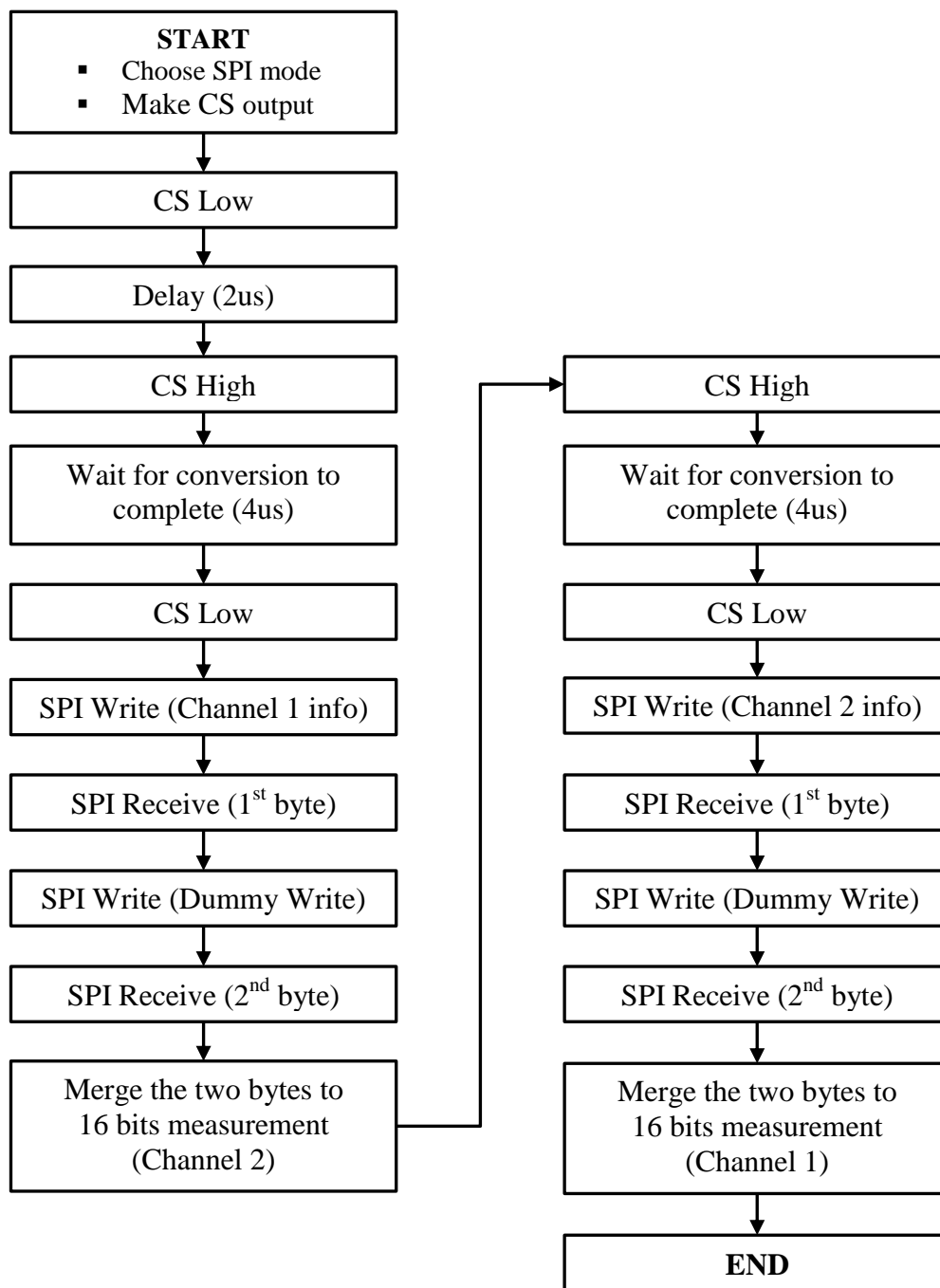


Figure A-1: Voltage & Current Measurement Flow Diagram

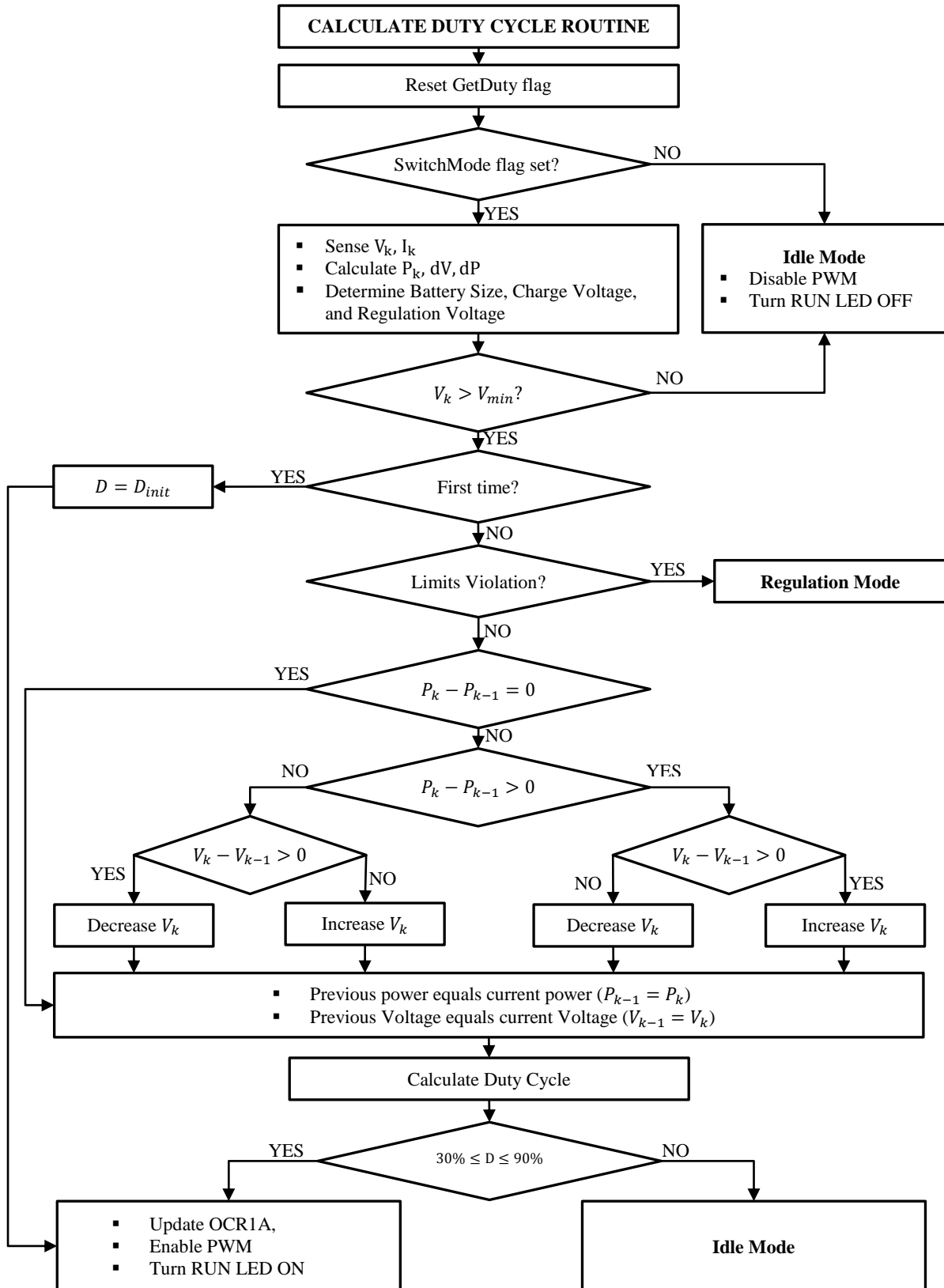


Figure A-2: MPPT P&O Flow Diagram

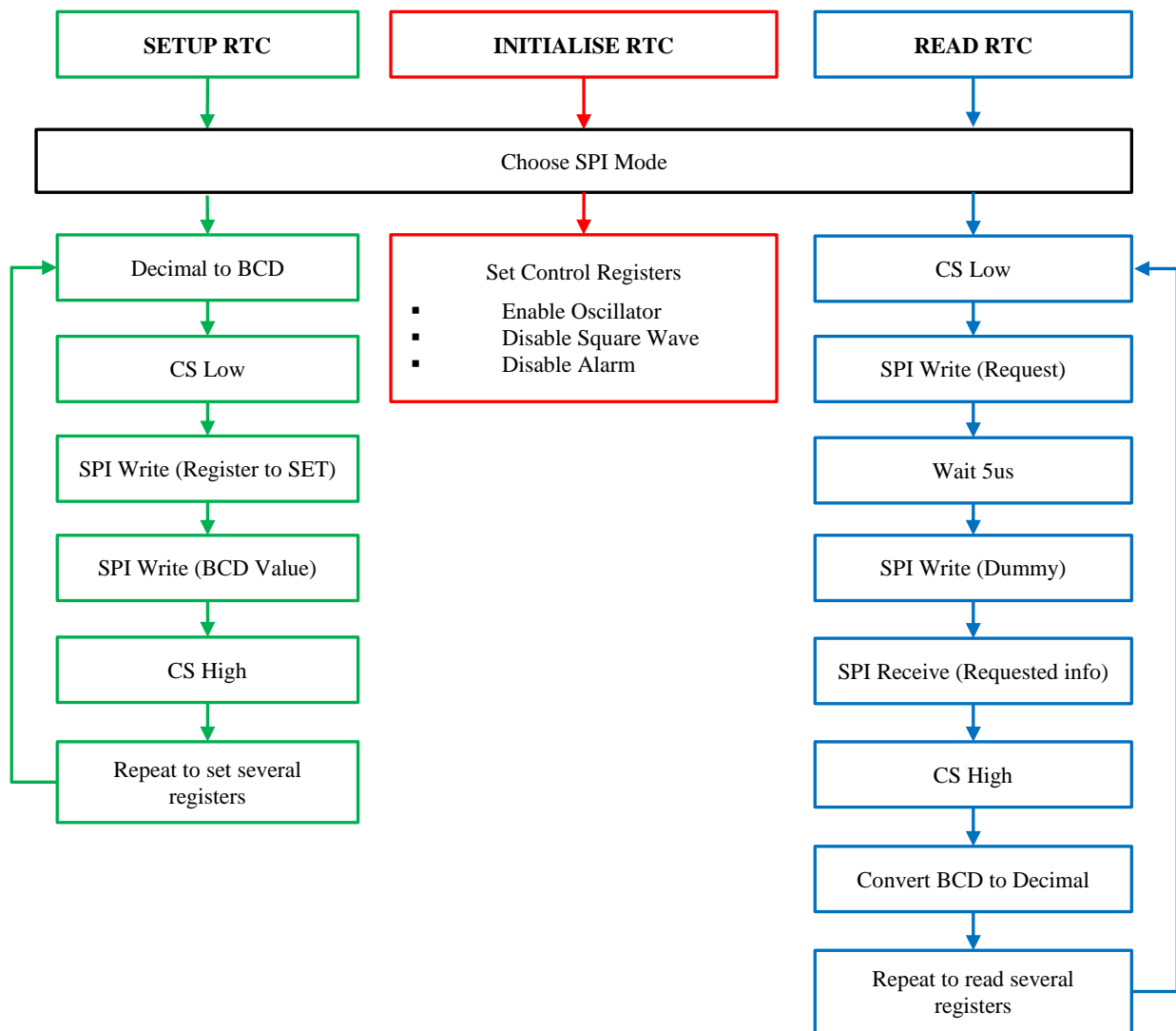


Figure A-3: RTC Setting & Reading Flow Diagram

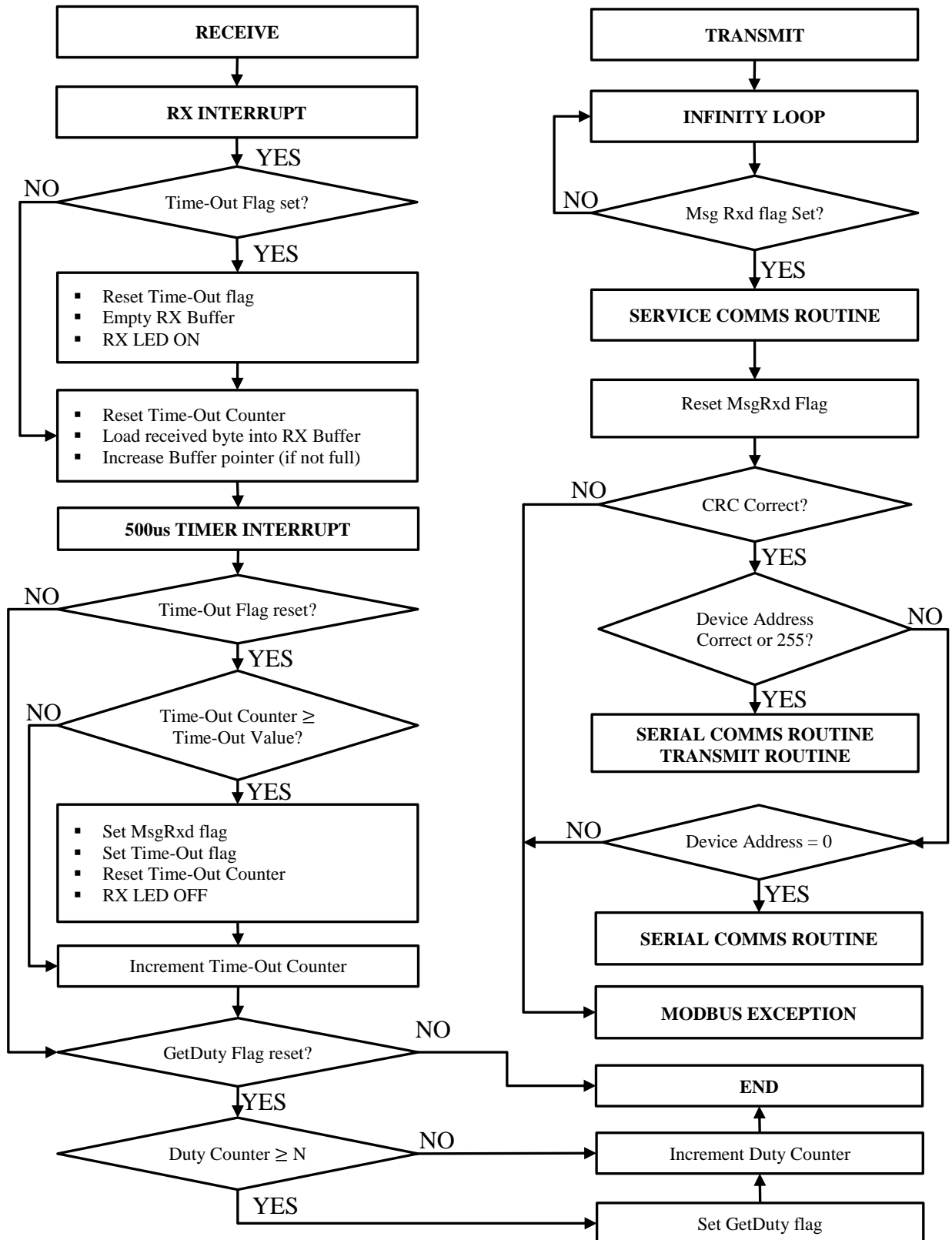


Figure A-4: USART Communication Flow Diagram

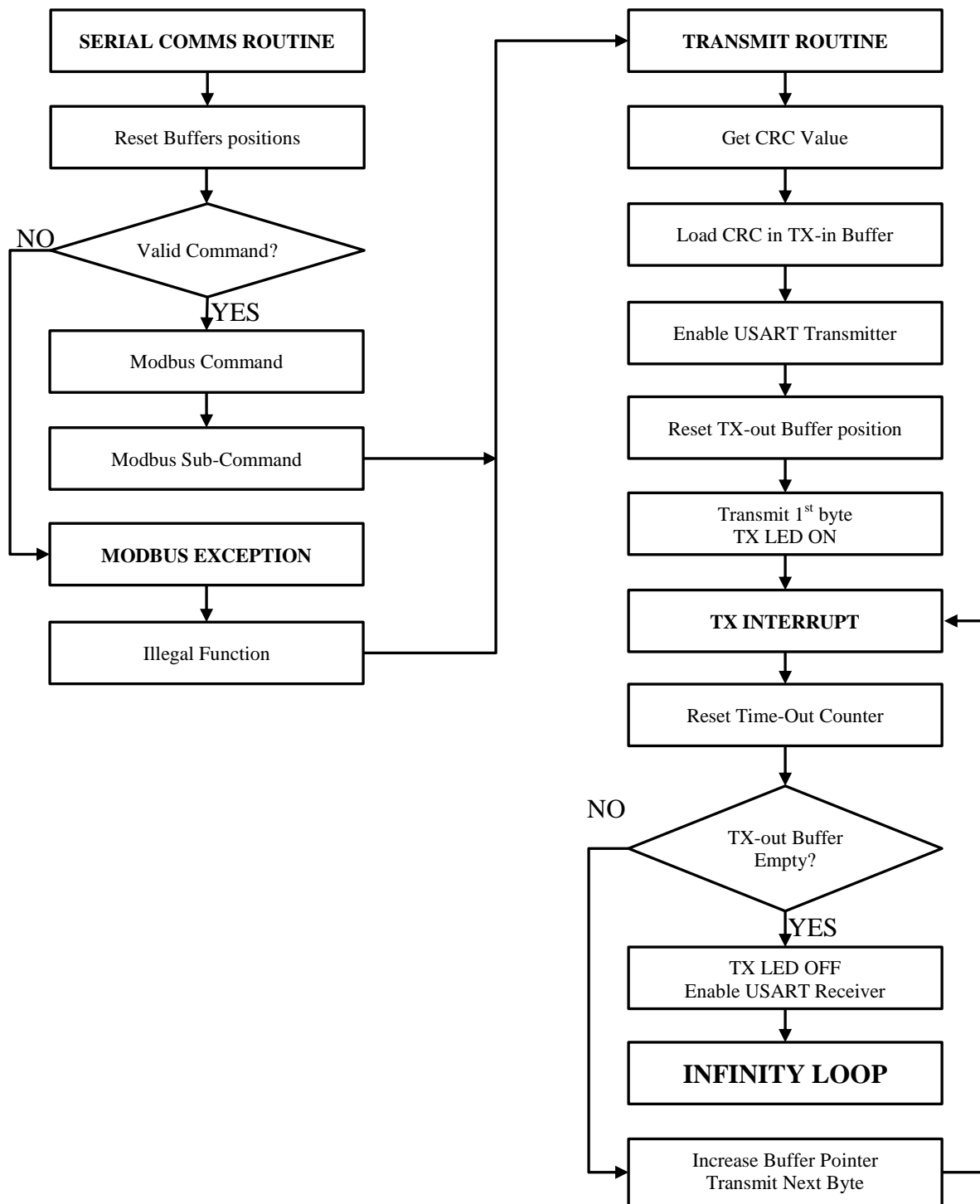


Figure A-5: USART Communication Flow Diagram

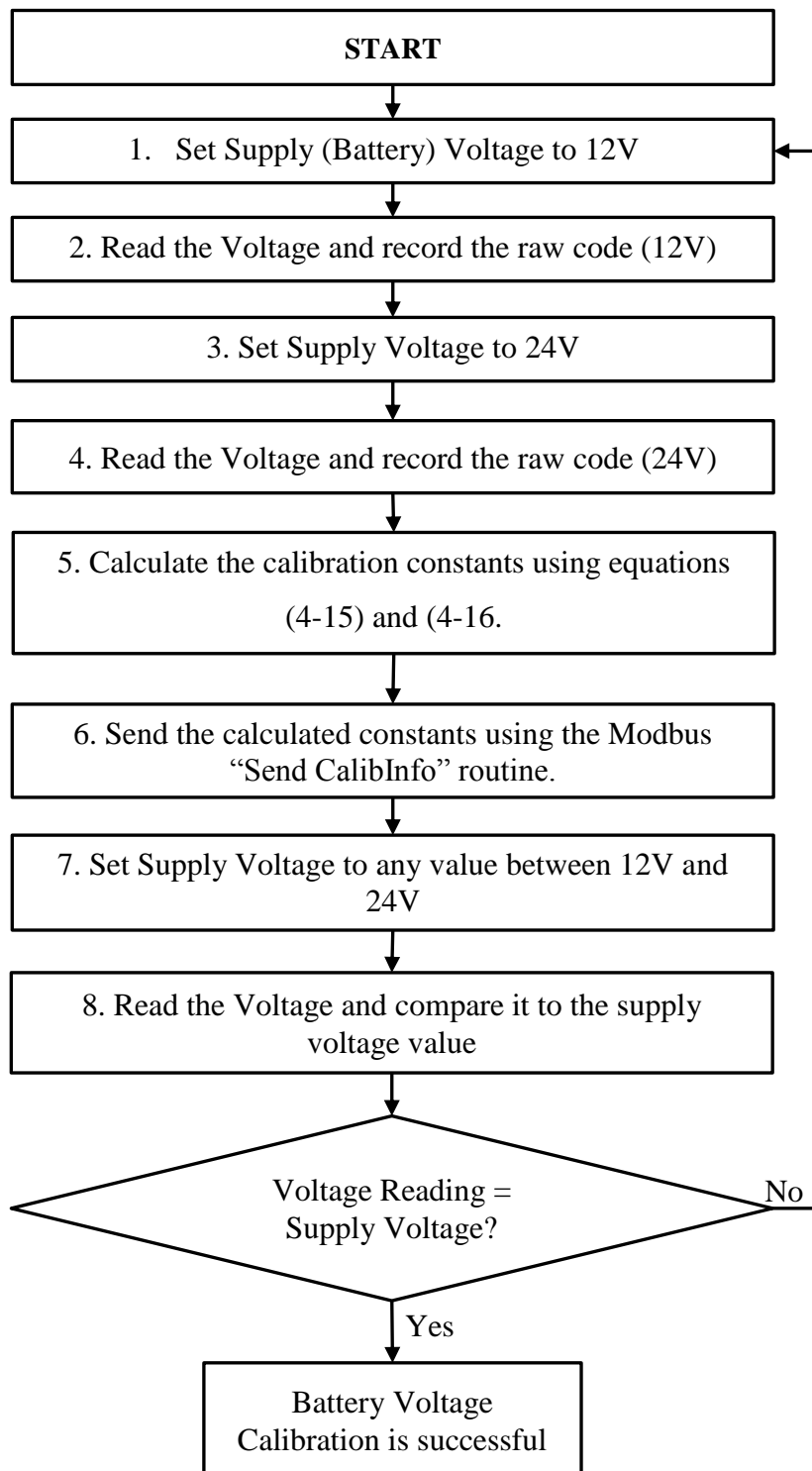


Figure A-6: MPPT Battery Voltage Calibration Flow Diagram

B. MPPT MODBUS COMMANDS DOCUMENTATION

- **Send Device Information**

Command 41H, Sub-Command 1H. This command sends the device information upon request by the master device. The device information includes the Device ID, Software Version and device description.

- **Get Device Information**

Command 41H, Sub-Command 2H. This is the command through which the MPPT receives the device information changes when necessary.

- **Return RX Buffer (Echo)**

Command 41H, Sub-Command 3H. This command is for diagnostic purposes. It returns whatever information that the MPPT has received.

- **Send RTC**

Command 41H, Sub-Command 4H. This is the command through which the MPPT sends RTC data. The RTC data is sent altogether in one batch of 8-bit characters in following order: Year, Month, Day, Day of Week, Hour, Minute, and Second.

- **Get RTC**

Command 41H, Sub-Command 5H. This is the command through which the MPPT receives the RTC settings data in the same order as above.

- **Set Device Address & Baud Rate**

Command 41H, Sub-Command 6H. Through this command the device address can be changed from its default value. This command is also used to change the Baud Rate by sending the respective index:

Table B-1: Baud Rate Indices

Index	0	1	2	3	4	5	6	7
Baud Rate	2400	4800	9600	14400	19200	38400	57600	115200

- **Send Calibration Information**

Command 42H, Sub-Command 3H, 4H and 5H. This command is used to get the calibration information from the device.

- **Get Calibration Information**

Command 42H, Sub-Command 6H. This command is for sending the calibration to the device. The calibration information will automatically be updated to the microcontroller EEPROM when this command is run.

- **Send Measurement**

Command 42H, Sub-Command 7H. This is the command through which the measurement data is requested from the device. The data consists of five floats packed in the following order: PV voltage, PV Current, Battery Voltage, Battery Current, and the Duty Cycle.

- **Switch Device ON**

Command 0x42, Sub-Command 0x09. This command is for switching ON the MPPT. The MPPT is OFF when the power is first switched on. If this command is run, the MPPT checks whether the PV voltage is higher than the battery voltage and make a decision whether to start charging the battery or to go in idle mode where it continues to monitor the PV voltage.

- **Switch Device OFF**

Command 0x42, Sub-Command 0x0A. This command instructs the MPPT to switch OFF.

C. ACTIVE LOAD FLOW DIAGRAMS

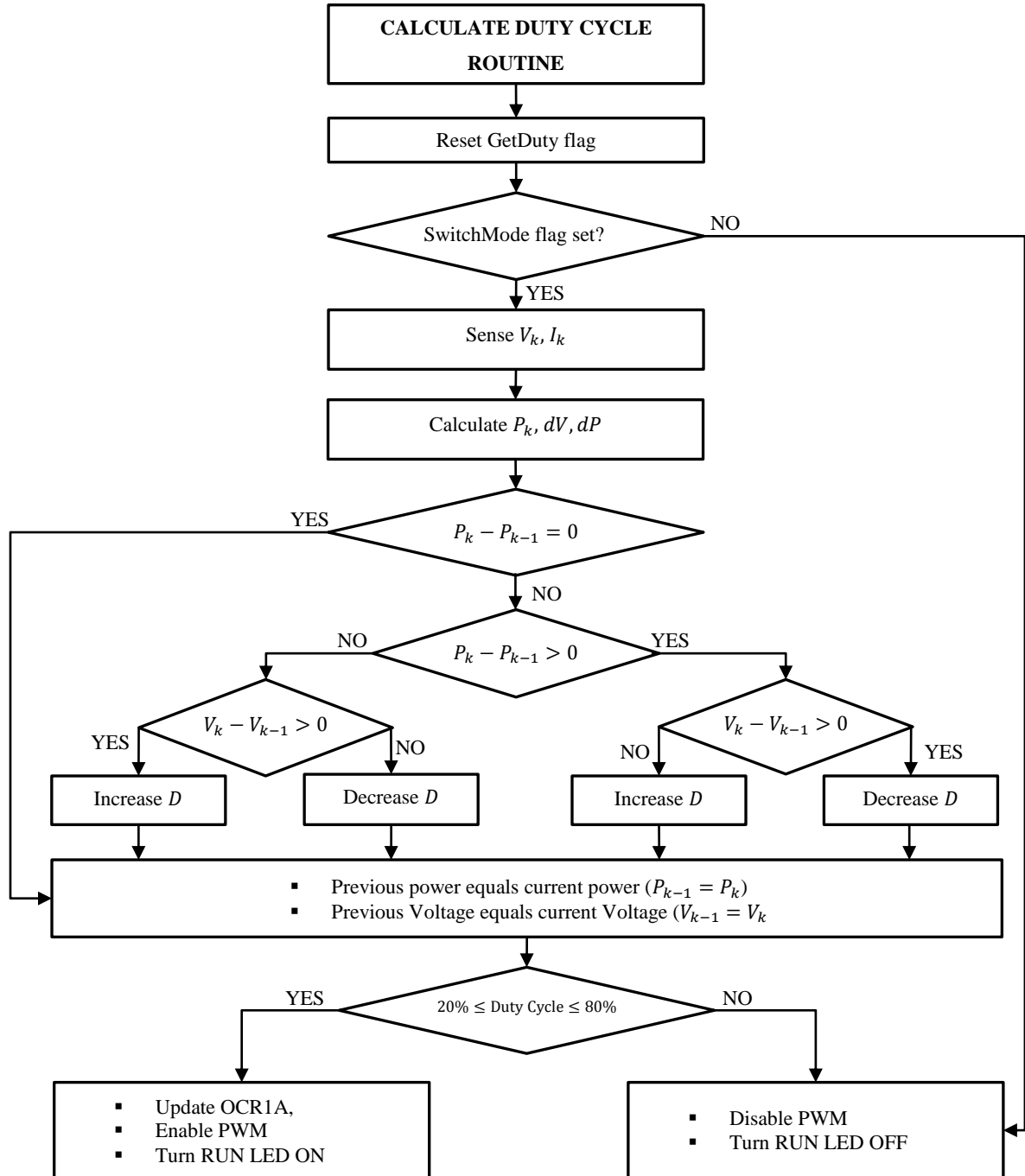


Figure C-1: Active Load P&O Flow Diagram

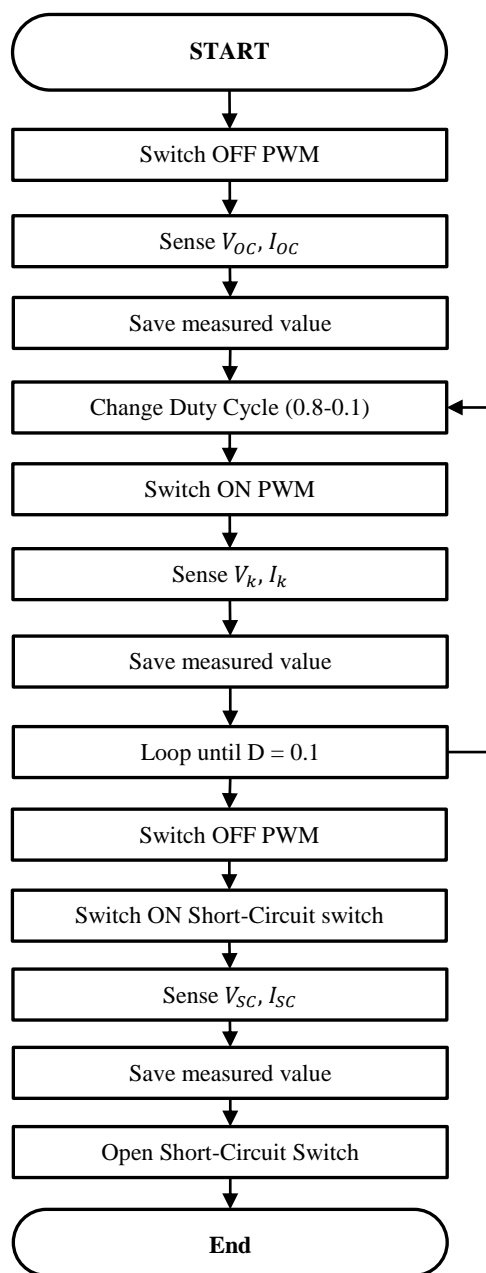


Figure C-2: I-V Curve Derivation Flow Diagram

D. MPPT TEST RESULTS

Table D-1: MPPT test results (20.10.2014)

Sample Time	PV Voltage (V)	PV Current (A)	Bat Voltage (V)	Bat Current (A)	Duty Cycle
10:45:00	38.620	0.000	13.164	0.000	0.000
10:45:26	31.126	2.134	13.829	4.436	0.467
10:45:30	32.730	1.768	13.790	3.915	0.445
10:45:35	32.912	1.730	13.800	3.856	0.442
10:45:38	33.047	1.690	13.806	3.799	0.441
10:45:42	33.185	1.657	13.800	3.715	0.439
10:45:44	33.195	1.666	13.805	3.742	0.439
10:45:47	33.206	1.651	13.808	3.695	0.439
10:45:50	33.335	1.621	13.806	3.675	0.437
10:45:53	33.355	1.630	13.805	3.669	0.437
10:45:56	33.465	1.607	13.806	3.655	0.435
10:45:58	33.465	1.587	13.810	3.623	0.435
10:46:01	33.458	1.602	13.807	3.635	0.435
10:46:04	33.473	1.606	13.807	3.655	0.435
10:46:06	33.468	1.603	13.810	3.637	0.435
10:46:09	33.483	1.601	13.806	3.619	0.435
10:46:13	33.473	1.590	13.808	3.646	0.435
10:46:16	33.479	1.594	13.803	3.652	0.435
10:46:20	33.477	1.610	13.808	3.648	0.435
10:46:22	33.467	1.609	13.810	3.656	0.435
10:46:25	33.474	1.594	13.807	3.631	0.435
10:46:28	33.470	1.594	13.807	3.650	0.435
10:46:30	33.480	1.604	13.803	3.639	0.435
10:46:33	33.470	1.606	13.809	3.655	0.435
10:46:35	33.462	1.585	13.807	3.631	0.435
10:46:38	33.486	1.602	13.807	3.622	0.435
10:46:41	33.494	1.596	13.803	3.644	0.435
10:46:45	33.630	1.564	13.808	3.549	0.433
10:46:48	33.624	1.565	13.795	3.565	0.433
10:46:51	33.605	1.577	13.791	3.586	0.433
10:46:55	33.597	1.590	13.790	3.623	0.434
10:46:58	33.598	1.583	13.790	3.587	0.434
10:47:02	33.600	1.588	13.782	3.604	0.434

10:47:05	33.577	1.576	13.781	3.576	0.434
10:47:09	33.570	1.577	13.776	3.601	0.434
10:47:13	33.561	1.573	13.782	3.608	0.434
10:47:17	33.594	1.586	13.777	3.593	0.434
10:47:20	33.564	1.587	13.787	3.610	0.434
10:47:22	33.570	1.589	13.775	3.615	0.434
10:47:24	33.558	1.577	13.780	3.632	0.434
10:47:26	33.568	1.585	13.774	3.606	0.434
10:47:29	33.565	1.573	13.777	3.604	0.434
10:47:31	33.559	1.592	13.790	3.632	0.434
10:47:33	33.552	1.594	13.786	3.609	0.434
10:47:35	33.562	1.519	13.776	3.637	0.434
10:47:37	33.232	1.660	13.951	3.724	0.438
10:47:39	33.605	1.582	13.800	3.620	0.433
10:47:42	33.573	1.586	13.782	3.606	0.434
10:47:44	33.582	1.577	13.786	3.596	0.434
10:47:46	33.570	1.573	13.779	3.609	0.434

Table D-2: MPPT Loading Response test results (21.10.2014)

Sample Time	PV Voltage (V)	PV Current (A)	Bat Voltage (V)	Bat Current (A)	Duty Cycle
08:48:04	31.929	1.561	13.722	3.55	0.456
08:48:13	31.902	1.555	13.721	3.544	0.456
08:48:20	31.774	1.570	13.712	3.556	0.458
08:48:25	31.774	1.576	13.719	3.559	0.458
08:48:30	31.762	1.576	13.724	3.569	0.458
08:48:35	31.780	1.602	13.711	3.574	0.458
08:48:40	31.774	1.580	13.711	3.574	0.458
08:48:44	31.764	1.582	13.712	3.576	0.458
08:48:50	31.761	1.585	13.710	3.571	0.458
08:48:57	31.782	1.575	13.712	3.575	0.458
08:49:02	31.782	1.576	13.707	3.566	0.458
08:49:09	31.78	1.584	13.710	3.582	0.458
08:49:16	31.779	1.580	13.710	3.582	0.458
08:49:22	31.774	1.573	13.717	3.575	0.458
08:49:28	31.777	1.583	13.720	3.589	0.458
08:49:33	31.785	1.607	13.717	3.609	0.458
08:49:38	31.782	1.579	13.718	3.585	0.458
08:49:43	31.782	1.590	13.722	3.598	0.458
08:49:50	31.815	1.592	13.713	3.595	0.457
08:49:56	31.800	1.594	13.719	3.606	0.457

08:50:01	31.812	1.585	13.717	3.595	0.457
08:50:05	36.791	0.896	14.540	2.093	0.397
08:50:07	38.917	0.318	14.010	0.806	0.376
08:50:08	38.838	0.330	14.012	0.863	0.377
08:50:10	38.853	0.353	14.012	0.849	0.376
08:50:12	38.823	0.340	14.019	0.844	0.377
08:50:15	38.832	0.35	14.032	0.806	0.377
08:50:22	38.855	0.345	14.040	0.803	0.376
08:50:24	38.855	0.348	14.049	0.773	0.376
08:50:27	38.867	0.344	14.060	0.769	0.376
08:50:28	38.874	0.337	14.065	0.758	0.376
08:50:30	38.917	0.311	14.073	0.763	0.376
08:50:32	38.892	0.301	14.087	0.766	0.376
08:50:34	38.944	0.281	14.060	0.717	0.376
08:50:36	38.933	0.294	14.060	0.727	0.376
08:50:38	38.944	0.263	14.066	0.715	0.376
08:50:40	38.944	0.277	14.088	0.715	0.376
08:50:41	38.974	0.299	14.095	0.704	0.375
08:50:44	38.971	0.278	14.098	0.704	0.375
08:50:46	38.985	0.306	14.111	0.657	0.375
08:50:52	39.006	0.285	14.138	0.661	0.375
08:50:54	39.018	0.290	14.151	0.633	0.375
08:50:56	39.017	0.279	14.162	0.637	0.375
08:50:57	39.032	0.259	14.165	0.642	0.375
08:50:59	39.044	0.261	14.175	0.627	0.375
08:51:02	39.045	0.281	14.180	0.615	0.375
08:51:04	39.035	0.257	14.197	0.619	0.375
08:51:06	39.064	0.282	14.202	0.573	0.374
08:51:08	39.048	0.271	14.213	0.595	0.375

Table D-3: MPPT Efficiency test data (17.10.2014)

PV Voltage (V)	PV Current (A)	Battery Voltage (V)	Battery Current (A)	Duty Cycle	Power In (W)	Power Out (W)	Efficiency (%)
40.226	0.000	12.92	0.000	0.000	0.000	0.000	0.000
40.902	0.079	12.941	0.146	0.320	3.231	1.889	58.472
39.929	0.390	13.293	0.966	0.350	15.572	12.841	82.461
39.176	0.570	14.995	1.383	0.400	22.330	20.738	92.870
37.091	1.087	15.845	2.436	0.450	40.318	38.598	95.735
34.065	1.624	16.218	3.348	0.500	55.322	54.297	98.150
31.317	1.764	16.379	3.313	0.550	55.243	54.263	98.227

28.695	1.845	16.380	3.185	0.600	52.942	52.170	98.542
26.662	1.851	16.481	2.942	0.650	49.351	48.487	98.249
24.795	1.920	16.504	2.776	0.700	47.606	45.815	96.237
23.183	1.939	16.549	2.552	0.750	44.951	42.233	93.952
21.835	1.931	16.596	2.342	0.800	42.163	38.868	92.184

Table D-4: MPPT Battery Charging Data (30.11.2014)

Sample Time	PV Voltage (V)	PV Current (A)	Battery Voltage (V)	Battery Current (A)	Duty Cycle
12:59:31	36.785	0	12.643	0	0
12:59:50	33.530	1.038	13.104	2.401	0.411
13:00:02	33.664	1.021	13.166	2.394	0.411
13:01:39	34.167	0.902	13.389	2.349	0.412
13:02:19	34.226	0.873	13.435	2.364	0.412
13:03:09	34.318	0.852	13.467	2.294	0.412
13:04:05	34.374	0.871	13.484	2.312	0.412
13:06:12	34.547	0.915	13.540	2.301	0.412
13:07:41	34.526	1.008	13.596	2.315	0.413
13:08:10	34.662	0.986	13.588	2.277	0.412
13:09:17	34.679	0.977	13.589	2.267	0.412
13:10:35	34.692	0.994	13.595	2.287	0.412
13:11:32	34.68	0.982	13.596	2.243	0.412
13:13:52	34.765	0.973	13.620	2.239	0.411
13:14:55	34.774	1.006	13.634	2.249	0.412
13:18:00	34.986	0.977	13.652	2.246	0.410
13:19:55	34.944	0.955	13.639	2.249	0.410
13:21:07	34.952	0.923	13.636	2.225	0.410
13:23:00	34.967	0.930	13.643	2.229	0.410
13:24:09	34.933	0.972	13.688	2.258	0.411
13:25:23	34.892	0.979	13.666	2.262	0.411
13:31:35	35.092	0.940	13.698	2.272	0.410
13:33:13	35.126	0.966	13.711	2.242	0.410
13:35:35	35.183	0.977	13.729	2.256	0.410
13:37:24	35.215	0.967	13.744	2.255	0.41
13:39:11	35.280	0.982	13.756	2.263	0.409
13:40:42	35.273	0.965	13.765	2.242	0.410
13:43:45	35.329	0.949	13.775	2.253	0.409
13:47:10	35.329	0.929	13.794	2.245	0.410
13:49:11	35.389	0.938	13.820	2.233	0.410
13:53:01	35.583	1.000	13.890	2.328	0.410
13:56:21	35.673	0.994	13.919	2.347	0.409
13:59:30	35.748	0.994	13.947	2.332	0.409

14:18:33	35.420	1.043	14.301	2.321	0.423
14:21:21	35.405	0.972	14.311	2.192	0.424
14:25:50	35.614	0.914	14.334	2.043	0.421
14:29:22	35.929	0.867	14.329	1.906	0.417
14:31:41	36.262	0.812	14.331	1.802	0.414
14:33:57	36.271	0.783	14.339	1.732	0.414
14:35:33	36.412	0.769	14.327	1.637	0.412
14:36:34	36.433	0.749	14.333	1.653	0.412
14:38:06	36.441	0.727	14.340	1.613	0.412
14:39:30	36.592	0.713	14.344	1.526	0.410
14:41:04	36.629	0.711	14.346	1.549	0.410
14:42:34	36.792	0.688	14.350	1.490	0.408
14:43:39	36.791	0.658	14.359	1.440	0.408
14:45:40	36.776	0.649	14.355	1.410	0.408
14:49:38	36.930	0.561	14.343	1.309	0.406
14:50:32	36.979	0.587	14.368	1.321	0.406
14:51:31	37.127	0.546	14.351	1.242	0.404
14:54:19	37.274	0.512	14.344	1.194	0.402
14:55:53	37.105	0.520	14.341	1.153	0.404
14:57:05	37.136	0.518	14.365	1.170	0.404
14:58:45	37.164	0.503	14.376	1.163	0.404
15:00:18	37.174	0.480	14.391	1.115	0.404
15:01:34	37.336	0.422	14.367	1.104	0.402
15:03:28	37.345	0.464	14.389	1.087	0.402
15:04:17	37.321	0.407	14.371	1.052	0.402
15:05:39	37.305	0.398	14.362	1.016	0.402
15:06:41	37.283	0.409	14.361	1.025	0.402
15:07:25	37.321	0.392	14.371	1.016	0.402
15:09:03	37.317	0.406	14.370	0.984	0.402
15:10:24	37.306	0.389	14.373	0.979	0.402
15:13:47	37.453	0.355	14.370	0.923	0.401
15:14:33	37.474	0.355	14.372	0.918	0.400
15:15:14	37.476	0.361	14.382	0.923	0.400
15:16:05	37.509	0.364	14.395	0.919	0.400
15:17:21	37.486	0.340	14.384	0.893	0.400
15:18:13	37.47	0.341	14.383	0.891	0.400
15:19:52	37.533	0.353	14.410	0.859	0.400
15:21:58	37.465	0.318	14.390	0.829	0.400
15:24:01	37.458	0.351	14.395	0.797	0.400
15:26:07	37.447	0.326	14.397	0.781	0.401
15:28:07	37.533	0.322	14.432	0.799	0.400
15:30:06	37.655	0.300	14.412	0.771	0.398
15:31:27	37.648	0.304	14.422	0.751	0.398
15:32:52	37.673	0.278	14.438	0.769	0.398

E. ACTIVE LOAD MODBUS COMMANDS DOCUMENTATION

The Modbus Commands are named in relation to the slave device.

- **Send Device Information**

Command 0x41, Sub-Command 0x01. This command sends the device information upon request by the master device. The device information includes the Device ID, Software Version and device description.

- **Get Device Information**

Command 0x41, Sub-Command 0x02. This is the command through which the Active Load receives the device information changes when necessary.

- **Return RX Buffer (Echo)**

Command 0x41, Sub-Command 0x03. This command is for debugging and diagnostic purposes. It transmits back whatever information that was received by the device.

- **Send RTC**

Command 0x41, Sub-Command 0x04. This is the command through which the Active Load sends RTC data. The RTC data is sent altogether in one batch of 8-bit characters in the following order: Year, Month, Day, Day of Week, Hour, Minute, and Second.

- **Get RTC**

Command 0x41, Sub-Command 0x05. This is the command through which the MPPT receives the RTC settings data in the same order as above.

- **Set Device Address & Baud Rate**

Command 0x41, Sub-Command 0x06. Through this command the device address can be changed from its default value. This command is also used to change the Baud Rate by sending the respective index:

Table E-1: Baud Rate Indices

Index	0	1	2	3	4	5	6	7
Baud	2400	4800	9600	14400	19200	38400	57600	115200

- **Connection Mode**

Command 0x41, Sub-Command 0x07. This command requests the device to do measurements and determine how the panels are connected on the ports. When there is only panel connected on P1 while either P2 or P3 is shorted, this command returns 0. The device returns 1 when two panels are connected in series on P1 and P2 while P3 is open. If two panels are connected in parallel on P2 and P3 while P1 is shorted, the device returns 2. If none of the known connection combinations was detected or it is night time, the device returns 3.

- **Send Temperatures**

Command 0x41, Sub-Command 0x08, 0x09. These commands are used to read the temperature sensors and send the temperature data.

- **Send Calibration Information**

Command 0x42, Sub-Command 0x03, 0x04 and 0x05. These commands are used to get the calibration information from the device. These commands are also used to run the Active Load in calibration mode with a fixed duty cycle.

- **Get Calibration Information**

Command 0x42, Sub-Command 0x06. This command is for sending the calibration to the device. The calibration information will automatically be updated to the microcontroller EEPROM when this command is run.

- **Send Measurements**

Command 0x42, Sub-Command 0x07. This is the command through which the measurement data is requested from the device. The data consists of three floats packed in the following order: PV voltage, PV Current, and the Duty Cycle.

- **Derive I-V Curve**

Command 0x42, Sub-Command 0x08. This command instructs the Active Load to swipe through a series of duty cycle and record measurements for each duty cycle. The measured data is returned as PV voltage, PV Current, and the Duty Cycle. The $I - V$ curve can then be plotted using the data returned by this command.

- **Switch Device ON**

Command 0x42, Sub-Command 0x09. This command instructs the Active Load to go into switch mode. By default, the Active Load is idle mode, it changes to switching mode when this command is run where it checks the PV voltage and starts switching if the PV voltage is above a set value.

- **Switch Device OFF**

Command 0x42, Sub-Command 0x0A. This command instructs the Active Load to switch OFF.

F. MPPT BATTERY CHARGER SCHEMATICS AND PCB LAYOUT

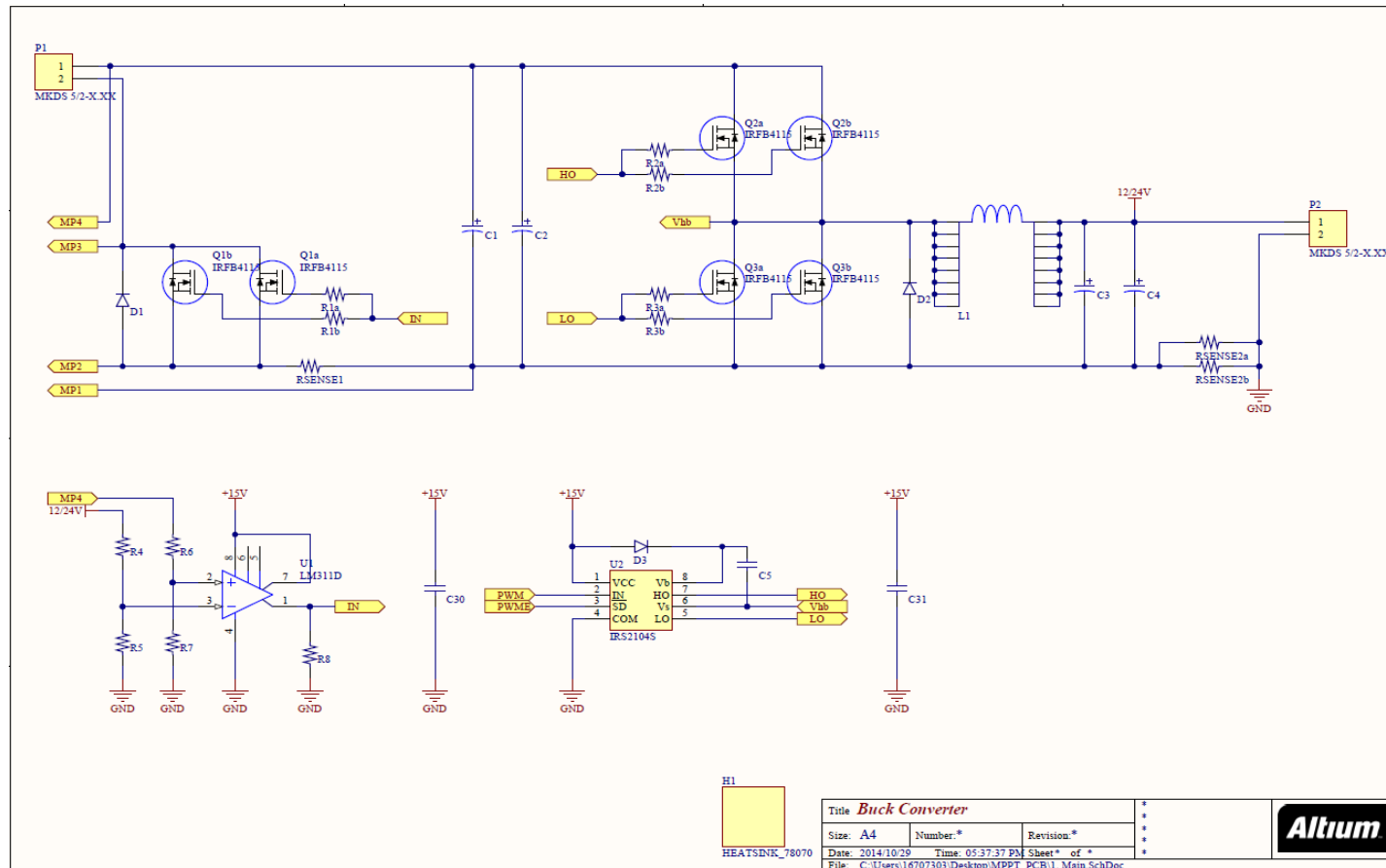


Figure F-1: MPPT Buck Converter

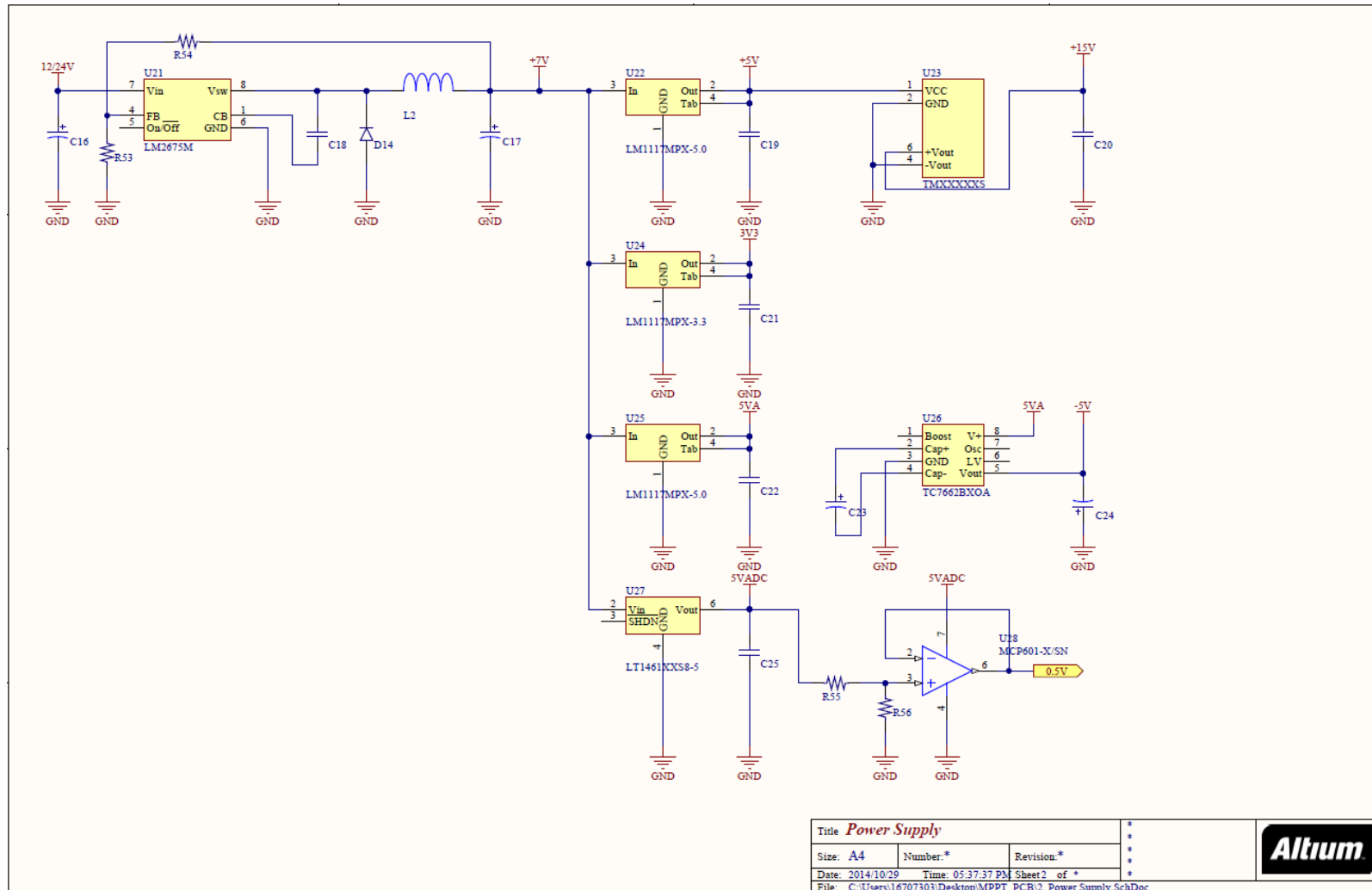


Figure F-2: MPPT Power Supply Circuit

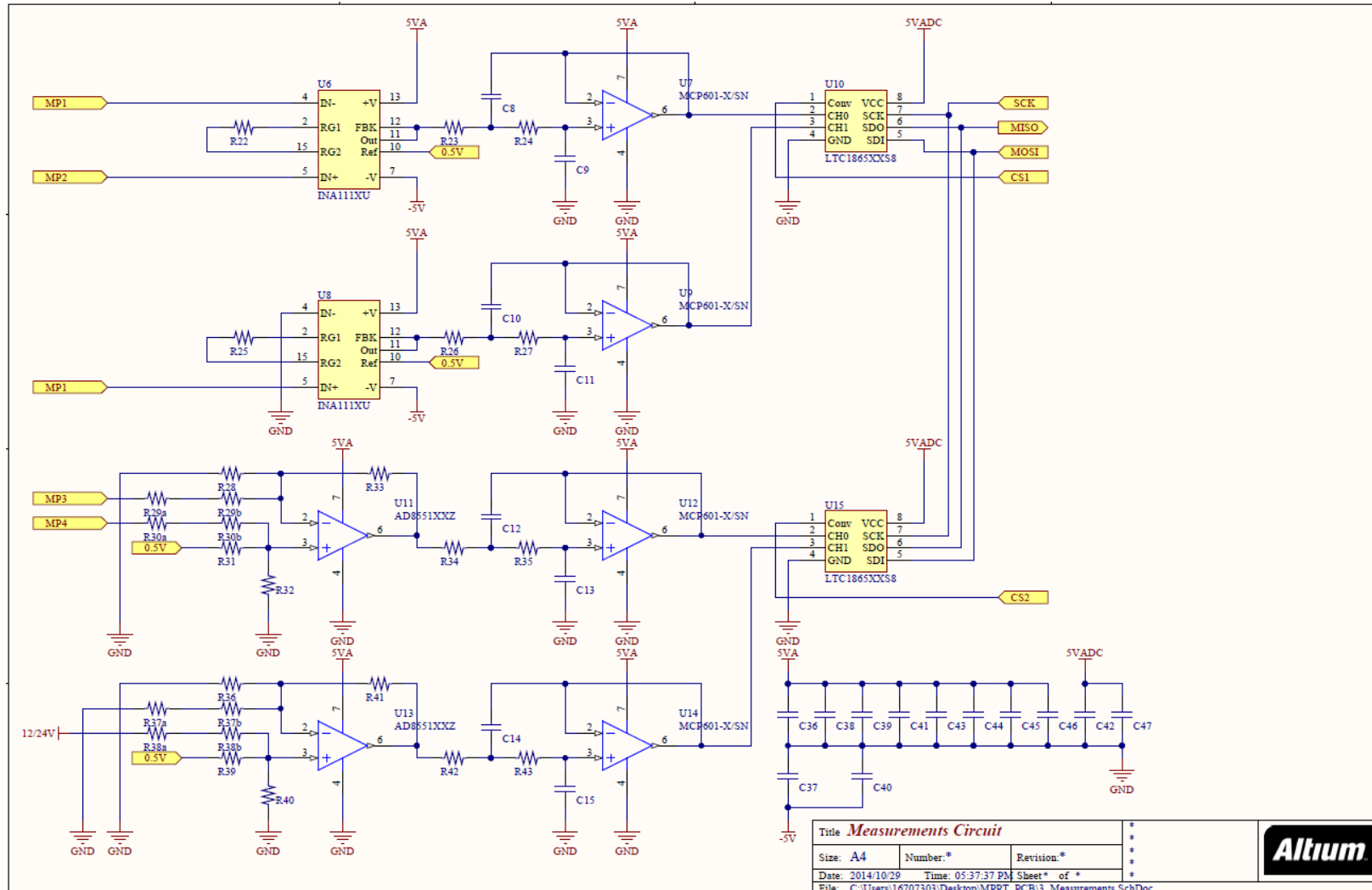


Figure F-3: MPPT Measurements Circuit

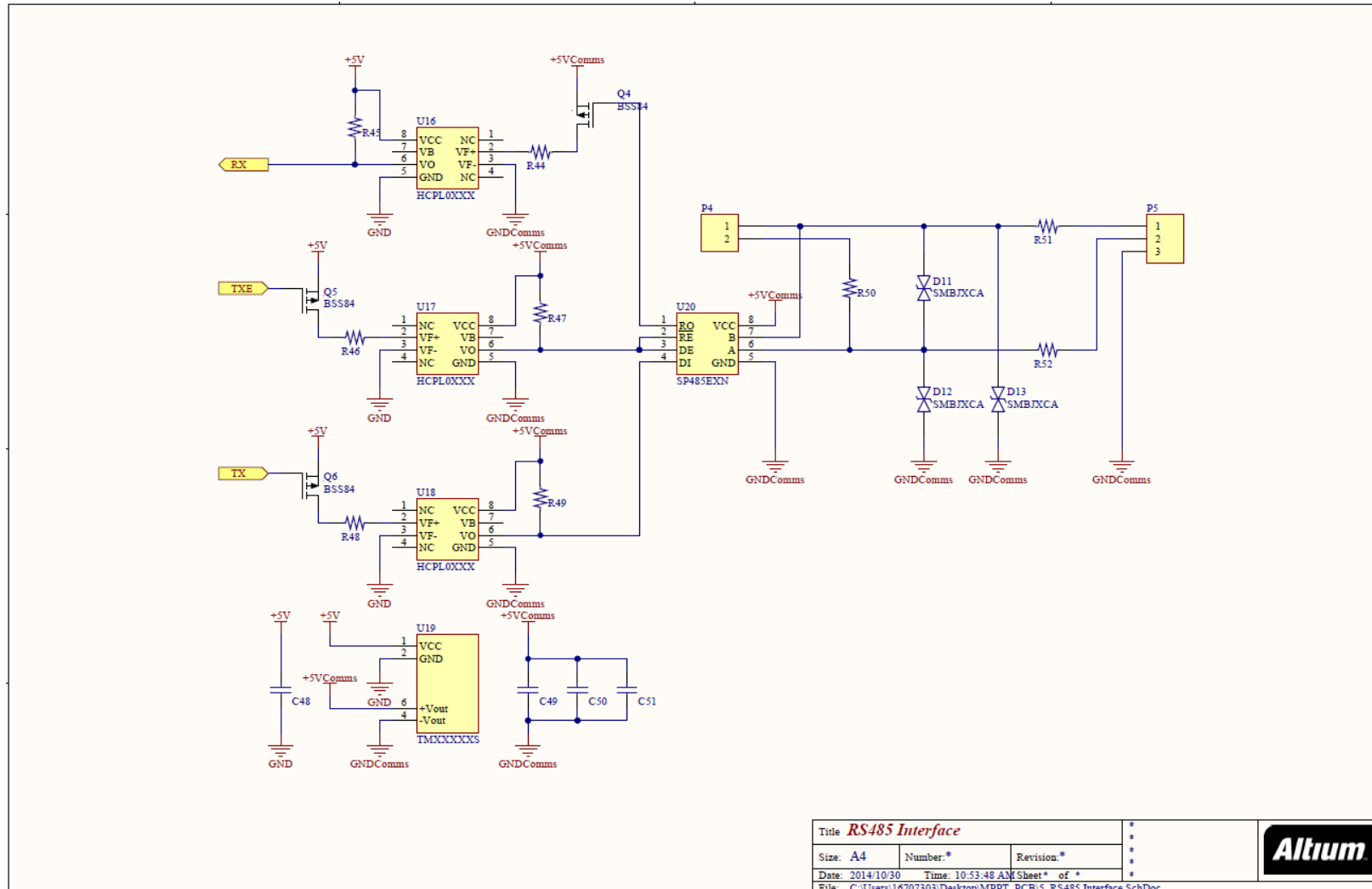


Figure F-4: MPPT Communication Circuit (RS 485)

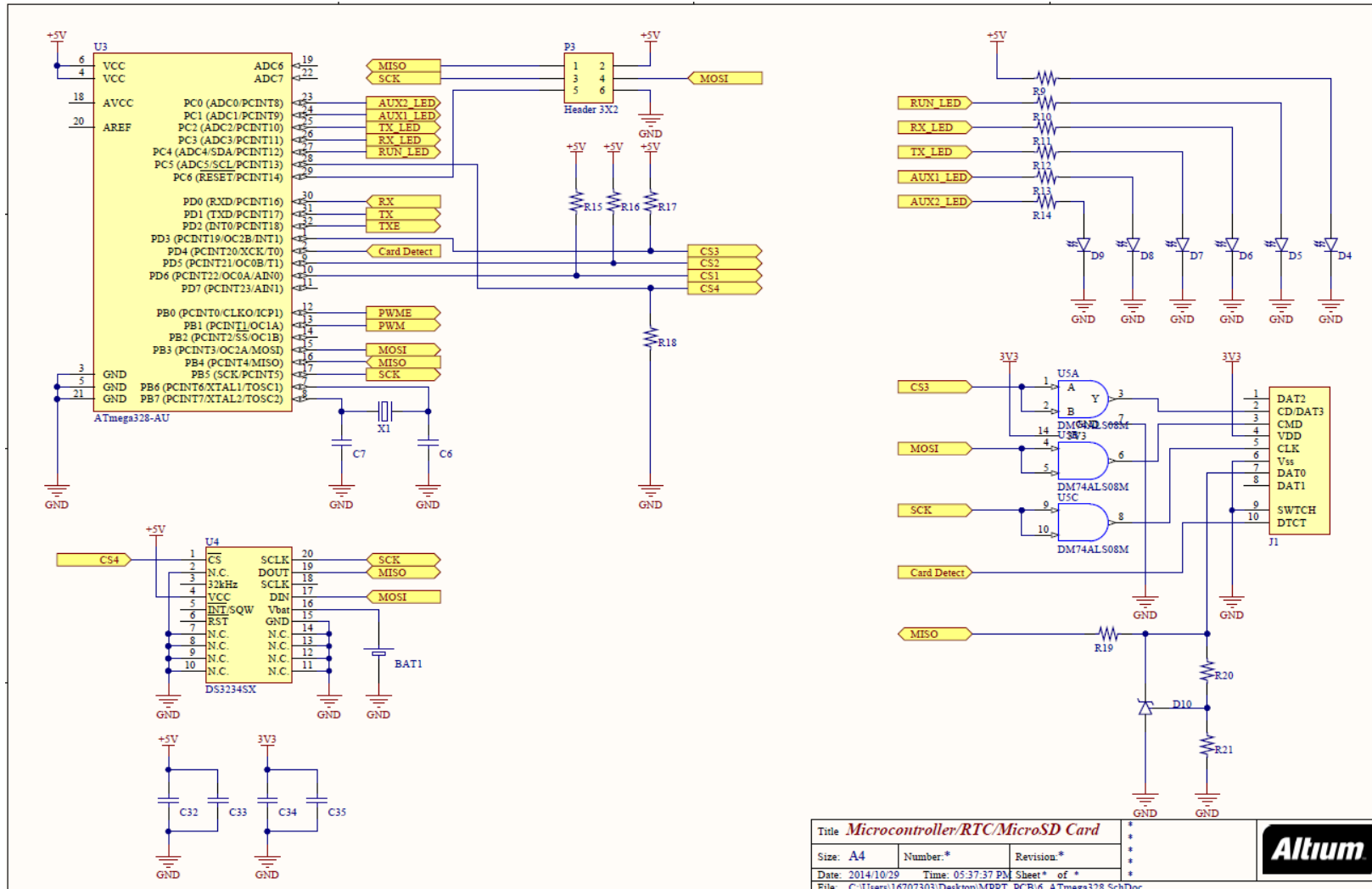


Figure F-5: MPPT Microcontroller Circuit

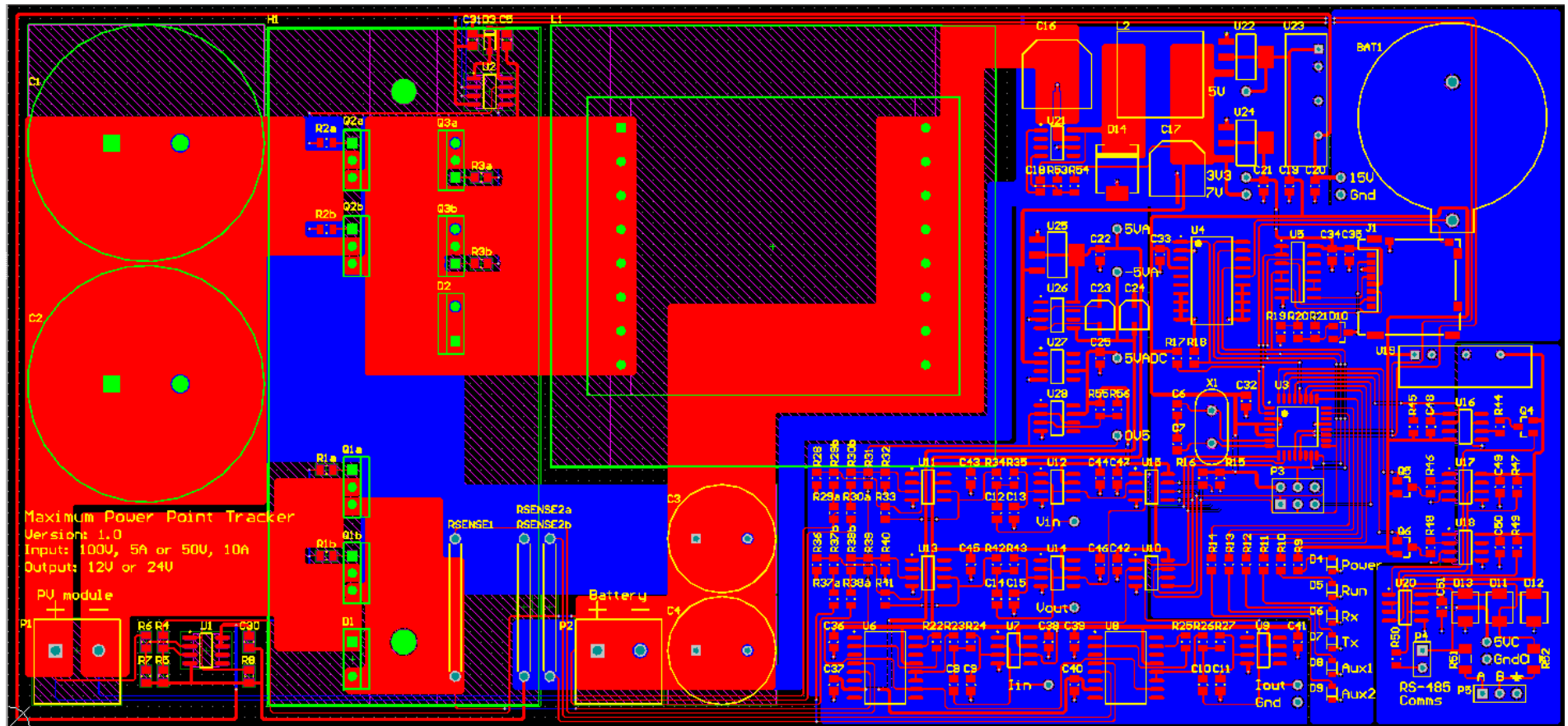


Figure F-6: MPPT PCB Layout

G. ACTIVE LOAD SCHEMATICS AND PCB LAYOUT

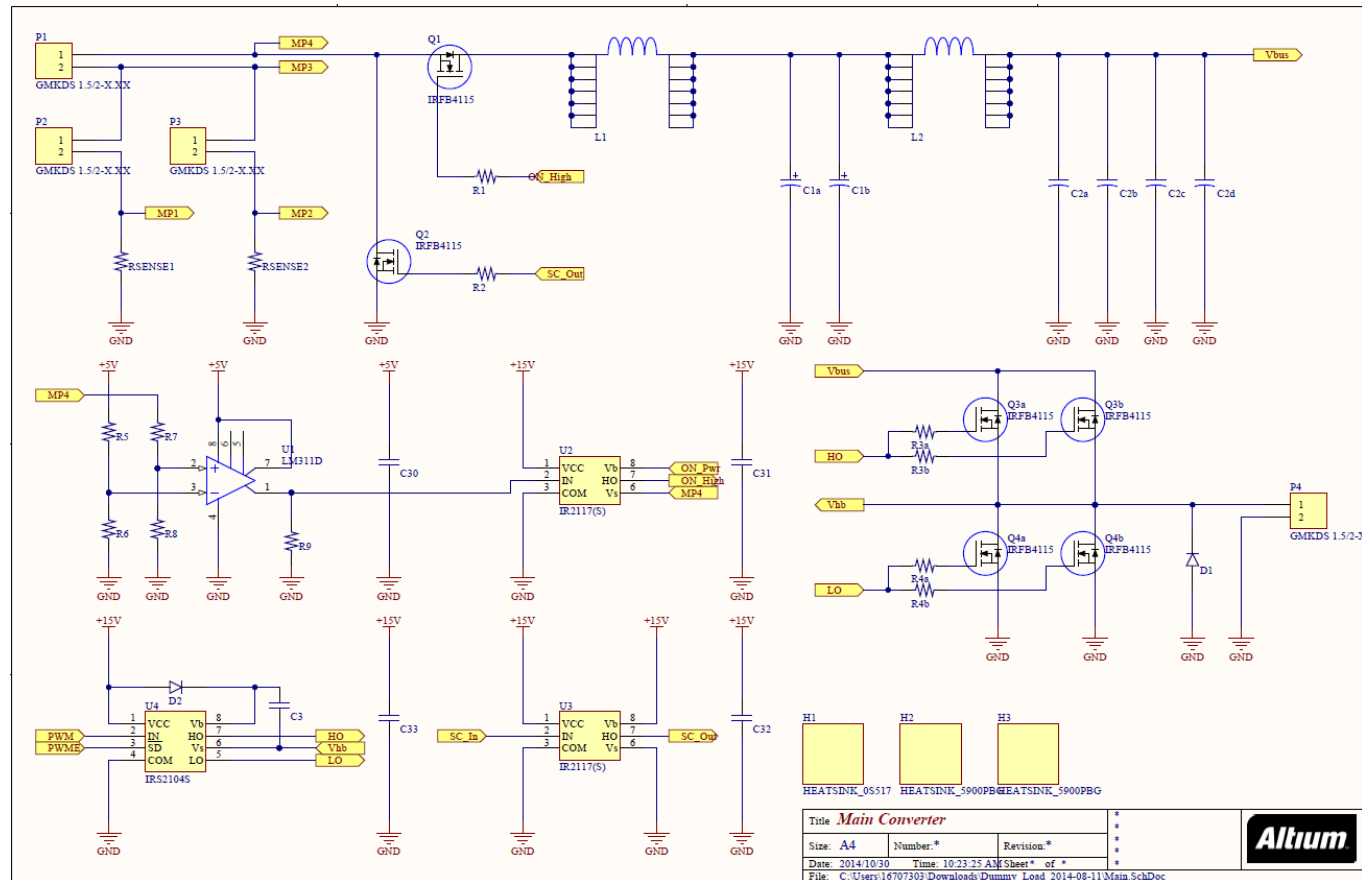


Figure G-1: Active Load Main Converter Circuit

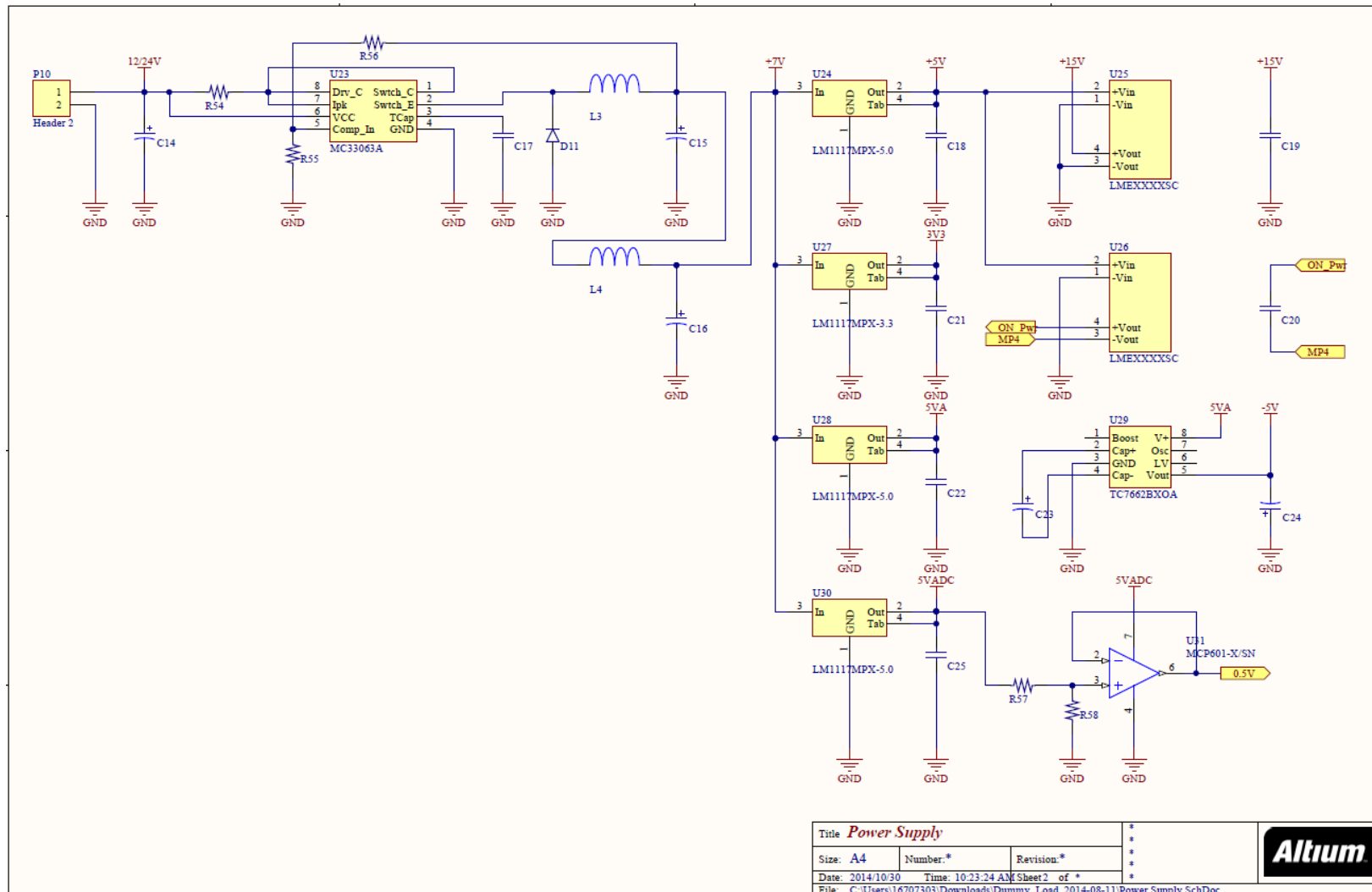


Figure G-2: Active Load Power Supply Circuit

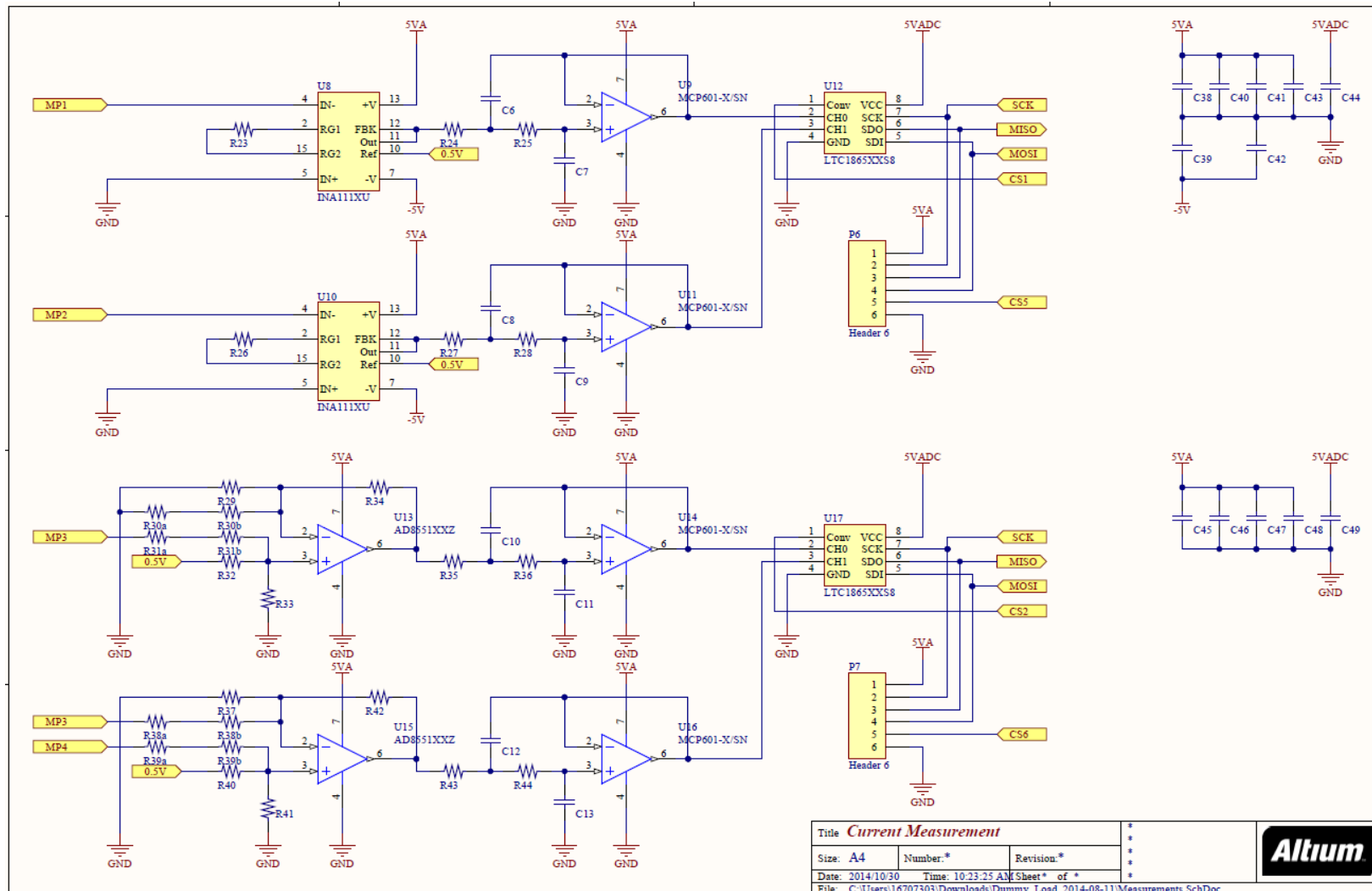


Figure G-3: Active Load Measurement Circuit

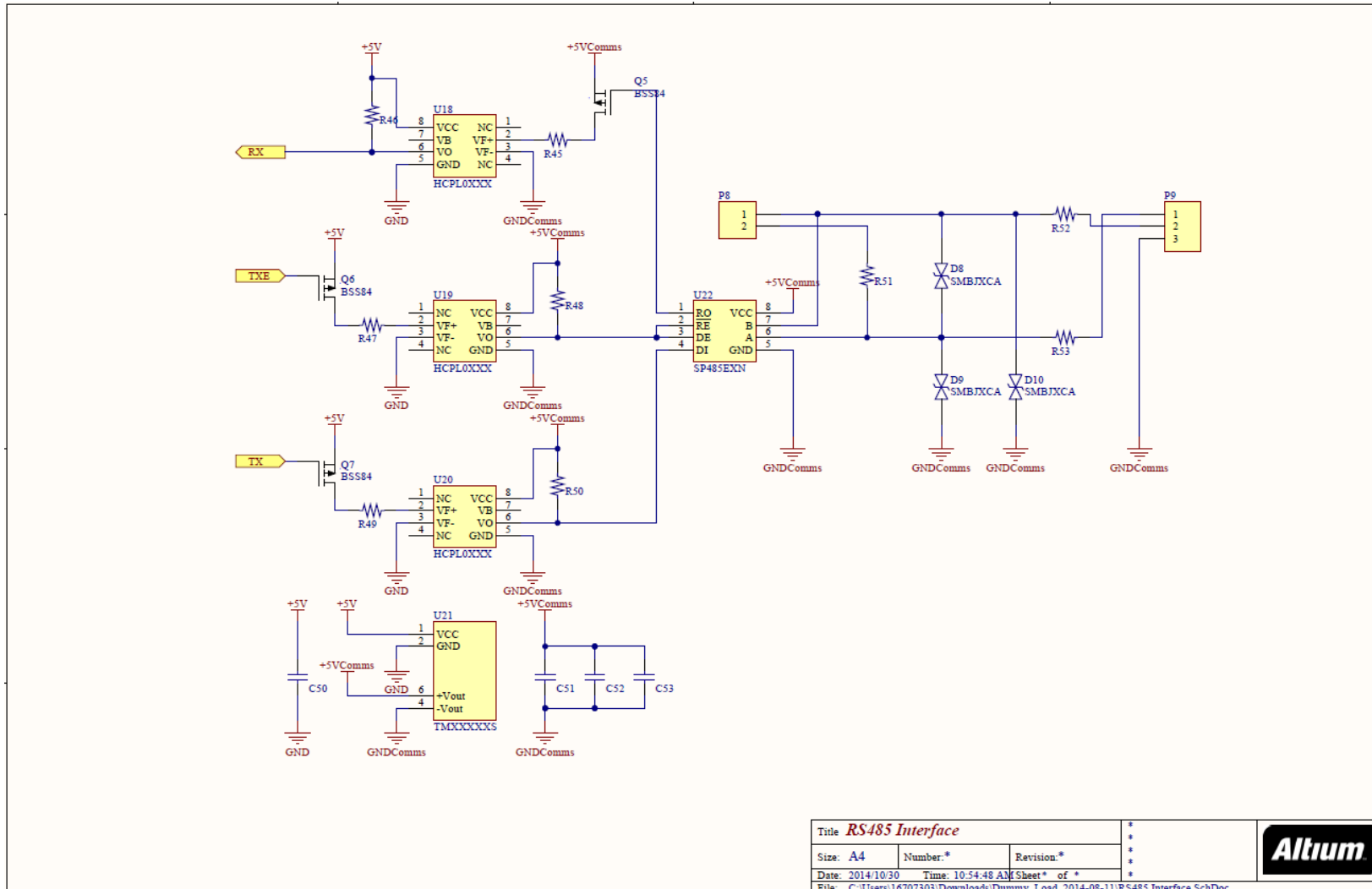


Figure G-4: Active Load Communication Circuit (RS 485)

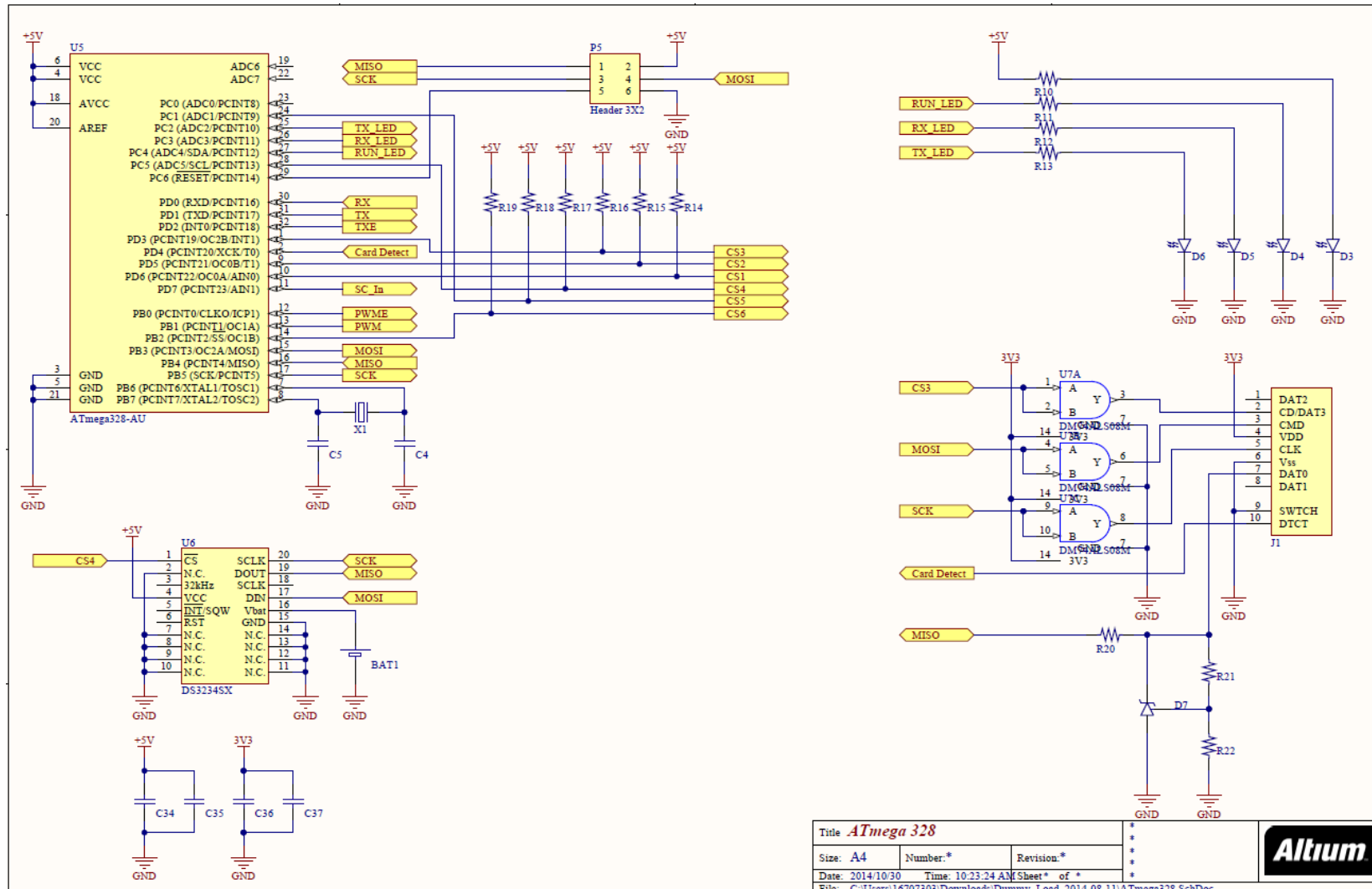


Figure G-5: Active Load Microcontroller Circuit

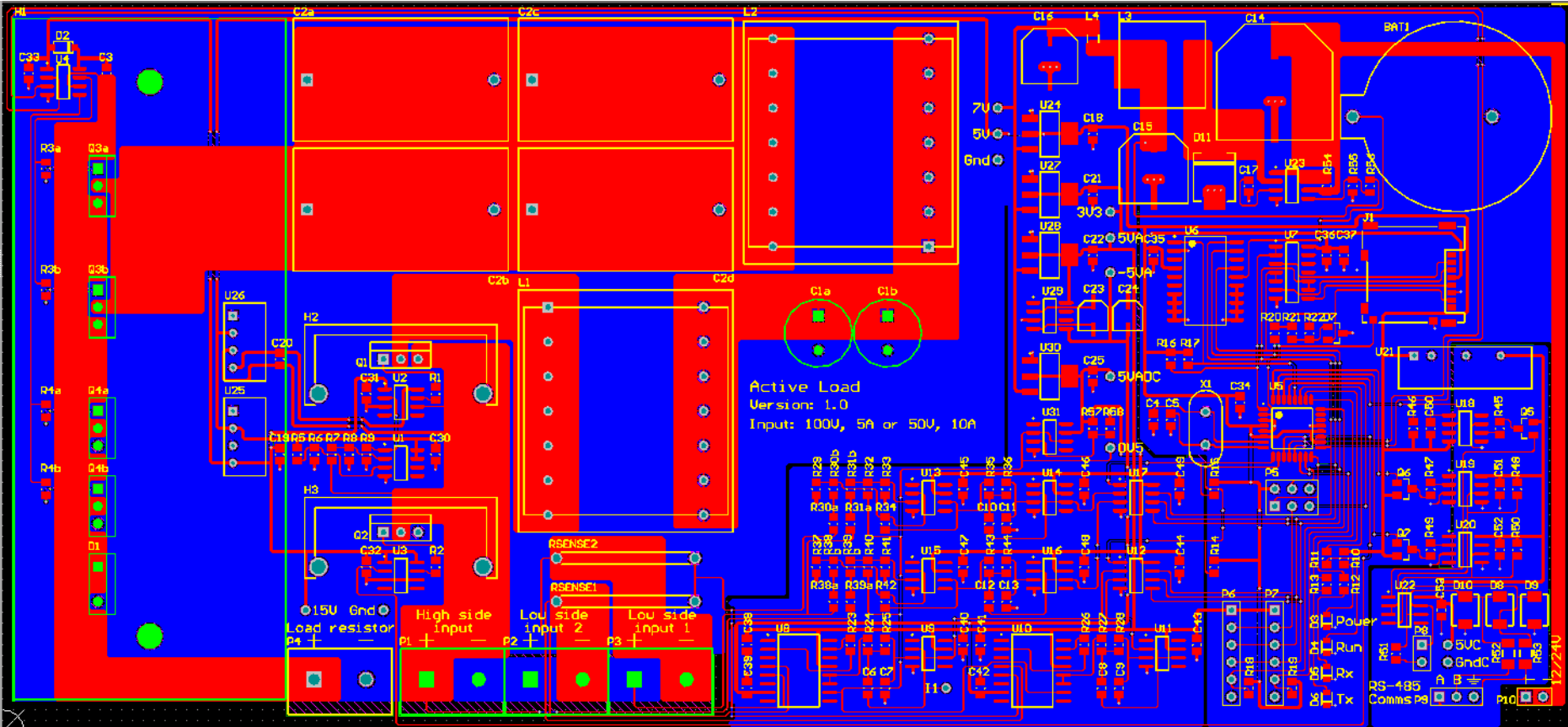


Figure G-6: Active Load PCB Layout

H. ACTIVE LOAD TEST RESULTS

Table H-1: IV Curve derivation data (12 November 2014)

Voltage, V	Current, A	Duty Cycle	Power, W	Comment
0	3.502	N/A	0	Short Circuit
8.032	3.491	0.600	28.040	
9.331	3.490	0.550	32.566	
11.032	3.479	0.500	38.381	
16.534	3.464	0.400	57.274	
21.236	3.456	0.350	73.392	
27.462	3.369	0.300	92.519	MPP
32.592	2.811	0.250	91.616	
37.102	1.668	0.180	61.887	
39.086	1.071	0.140	41.861	
40.468	0.569	0.100	23.026	
41.975	0	N/A	0	Open Circuit

Table H-2: Active Load MPPT Test Results (08.10.2014)

Sample Time	PV Voltage, V	PV Current, A	Duty Cycle	PV Power, W
11:47:26	42.63	0.000	0.000	0.000
11:47:36	28.948	3.454	0.340	99.986
11:47:41	30.725	3.287	0.360	100.993
11:47:43	30.723	3.288	0.360	101.017
11:47:45	30.773	3.291	0.360	101.274
11:47:48	30.702	3.292	0.360	101.071
11:47:51	30.733	3.293	0.360	101.204
11:47:54	29.069	3.466	0.340	100.753
11:47:56	29.106	3.470	0.340	100.998
11:47:58	29.076	3.471	0.340	100.923
11:48:00	29.123	3.475	0.340	101.202
11:48:03	29.138	3.477	0.340	101.313
11:48:05	29.126	3.483	0.340	101.446
11:48:07	29.162	3.487	0.340	101.688
11:48:10	29.342	3.501	0.340	102.726
11:48:13	29.025	3.464	0.340	100.543
11:48:15	30.154	3.238	0.320	97.639
11:48:17	31.072	2.631	0.320	81.750
11:48:19	30.131	2.882	0.300	86.838
11:48:21	30.342	2.904	0.30	88.113
11:48:24	29.518	3.523	0.340	103.992

11:48:26	30.959	3.325	0.360	102.939
11:48:29	31.056	3.328	0.36	103.354
11:48:31	29.436	3.522	0.34	103.674
11:48:33	30.982	3.328	0.36	103.108
11:48:35	29.463	3.529	0.34	103.975
11:48:37	31.130	3.344	0.36	104.099
11:48:39	29.284	3.504	0.34	102.611
11:48:40	32.284	3.090	0.34	99.758
11:48:42	30.237	3.250	0.36	98.270
11:48:49	31.243	2.990	0.34	93.417
11:48:55	29.849	3.205	0.32	95.666

Table H-3: Active Load MPPT Test Results (10.11.2014)

Sample Time	PV Voltage, V	PV Current, A	Duty Cycle	PV Power, W
11:56:14	29.621	2.614	0.258	77.429
11:56:20	29.626	2.612	0.258	77.383
11:56:24	29.03	2.671	0.252	77.539
11:56:27	29.571	2.609	0.258	77.151
11:56:30	29.610	2.611	0.258	77.312
11:56:40	29.602	2.610	0.258	77.261
11:56:51	28.984	2.671	0.252	77.416
11:58:00	29.059	2.668	0.252	77.529
12:00:12	29.734	2.604	0.258	77.427
12:00:16	29.770	2.604	0.258	77.521
12:00:18	29.785	2.603	0.258	77.530
12:00:21	29.100	2.664	0.252	77.522
12:00:25	29.030	2.663	0.252	77.306
12:00:28	29.743	2.605	0.258	77.481
12:02:23	29.073	2.663	0.252	77.421
12:02:39	29.739	2.604	0.258	77.440
12:03:28	29.099	2.662	0.252	77.462
12:13:16	29.674	2.596	0.258	77.034
12:13:25	29.645	2.592	0.258	76.840
12:13:29	28.935	2.656	0.252	76.851
12:15:51	29.737	2.602	0.258	77.376
12:15:53	29.684	2.590	0.258	76.882
12:15:55	29.045	2.659	0.252	77.231
12:19:20	29.746	2.606	0.258	77.519
12:19:23	29.085	2.664	0.252	77.483
12:19:27	29.100	2.667	0.252	77.610
12:19:30	29.774	2.606	0.258	77.591
12:20:36	29.679	2.614	0.258	77.581

12:20:41	29.017	2.659	0.252	77.156
12:21:11	29.749	2.609	0.258	77.615
12:23:38	28.959	2.669	0.252	77.292
12:23:42	29.609	2.615	0.258	77.428
12:25:16	29.042	2.673	0.252	77.62927
12:25:23	29.736	2.615	0.258	77.75964
12:26:29	29.716	2.603	0.258	77.35075
12:26:35	28.994	2.659	0.252	77.09505
12:30:34	29.671	2.611	0.258	77.47098
12:33:39	29.744	2.61	0.258	77.63184
12:33:49	29.016	2.665	0.252	77.32764
12:34:16	28.874	2.67	0.252	77.09358
12:34:19	28.871	2.667	0.252	76.99896
12:34:31	29.197	2.645	0.252	77.22607
12:35:14	29.643	2.608	0.258	77.30894
12:38:08	28.977	2.649	0.252	76.76007
12:38:22	29.573	2.594	0.258	76.71236
12:41:56	29.609	2.591	0.258	76.71692
12:45:43	29.575	2.596	0.258	76.7767
12:47:22	28.842	2.639	0.258	76.11404
12:50:18	28.851	2.651	0.258	76.484
12:53:26	29.807	2.594	0.258	77.31936

I. COMMISSIONING DATA

I.1 Active Loads Data: Day 1

Time	Solar Panel 1				Solar Panel 2			
	PV Voltage (V)	PV Current (A)	Duty Cycle	Power (W)	PV Voltage (V)	PV Current (A)	Duty Cycle	Power (W)
15:25	31.610	3.977	0.248	125.713	31.484	4.102	0.284	129.147
15:30	33.949	2.579	0.238	87.554	31.198	3.184	0.194	99.334
15:35	32.254	2.920	0.232	94.182	32.247	2.921	0.110	94.193
15:40	32.047	3.261	0.246	104.505	31.876	3.349	0.188	106.753
15:45	29.840	3.602	0.250	107.483	30.862	3.313	0.284	102.246
15:50	29.384	3.927	0.326	115.391	33.086	3.354	0.218	110.970
15:55	30.350	4.252	0.302	129.048	32.013	3.105	0.134	99.400
16:00	32.027	3.508	0.222	112.351	32.113	2.918	0.230	93.706
16:05	29.682	4.640	0.302	137.725	29.116	4.748	0.326	138.243
16:10	28.953	4.697	0.310	135.992	29.041	4.827	0.304	140.181
16:15	27.685	4.888	0.342	135.324	28.202	4.686	0.332	132.155
16:20	28.441	4.592	0.310	130.601	28.363	4.545	0.36	128.910
16:25	29.197	4.296	0.278	125.430	29.524	4.404	0.308	130.023
16:30	27.312	4.511	0.326	123.204	28.685	4.263	0.316	122.284
16:35	28.041	4.238	0.310	118.838	28.846	4.122	0.324	118.903
16:40	28.770	3.965	0.294	114.073	29.007	3.981	0.302	115.477
16:45	28.157	3.890	0.278	109.531	28.168	3.840	0.278	108.165
16:50	27.881	3.720	0.286	103.717	28.329	3.699	0.254	104.789
16:55	28.734	3.426	0.270	98.443	28.48	3.558	0.230	101.331
17:00	28.130	3.357	0.270	94.432	28.631	3.327	0.206	95.255
17:05	28.138	3.159	0.246	88.888	28.782	3.276	0.232	94.290
17:10	26.982	3.040	0.246	82.025	28.419	2.832	0.230	80.483
17:15	28.644	2.710	0.238	77.625	27.821	2.798	0.188	77.843
17:20	27.232	2.625	0.222	71.484	27.727	2.522	0.218	69.927
17:25	28.044	2.373	0.206	66.548	28.667	2.255	0.212	64.644
17:30	27.633	2.206	0.198	60.958	28.936	2.044	0.200	59.145
17:35	27.242	2.028	0.190	55.247	27.664	1.950	0.188	53.945
17:40	28.321	1.775	0.190	50.270	28.887	1.688	0.182	48.761
17:45	27.374	1.583	0.166	43.333	27.205	1.582	0.170	43.038
17:50	28.314	1.362	0.166	38.564	28.051	1.346	0.152	37.757
17:55	27.901	1.232	0.142	34.374	28.757	1.159	0.152	33.329
18:00	28.710	1.026	0.142	29.456	27.638	1.048	0.134	28.965

I.2 Active Loads Data: Day 2

Time	Solar Panel 1				Solar Panel 2			
	PV Voltage (V)	PV Current (A)	Duty Cycle	Power (W)	PV Voltage (V)	PV Current (A)	Duty Cycle	Power (W)
8:00	29.662	2.350	0.214	69.706	28.939	2.326	0.204	67.312
8:05	29.901	2.375	0.214	71.015	29.203	2.357	0.216	68.831
8:10	29.725	2.673	0.230	79.455	29.305	2.623	0.228	76.867
8:15	28.585	3.038	0.238	86.841	28.429	2.943	0.236	83.667
8:20	28.261	3.361	0.254	94.985	30.174	2.999	0.242	90.492
8:25	28.828	3.613	0.278	104.156	30.331	3.355	0.248	101.761
8:30	29.090	3.831	0.286	111.444	28.66	3.779	0.284	108.306
8:35	27.972	3.337	0.254	93.343	28.989	3.203	0.232	92.852
8:40	28.442	2.425	0.222	68.972	28.842	2.269	0.212	65.443
8:45	27.808	2.999	0.238	83.396	29.153	2.728	0.236	79.529
8:50	28.780	1.843	0.174	53.042	29.003	1.812	0.188	52.553
8:55	29.350	2.444	0.294	71.731	30.91	2.710	0.206	83.766
9:00	28.475	1.822	0.19	51.881	27.397	1.824	0.182	49.972
9:05	30.798	2.226	0.182	68.557	27.527	2.190	0.146	60.284
9:10	29.233	2.802	0.238	81.911	29.319	2.668	0.230	78.223
9:15	30.468	4.378	0.126	133.389	30.78	4.310	0.284	132.661
9:20	31.429	4.333	0.278	136.182	30.417	4.753	0.320	144.572
9:25	29.794	4.641	0.302	138.274	31.41	3.694	0.254	116.029
9:30	33.171	2.469	0.206	81.8992	31.403	3.635	0.248	114.150
9:35	27.794	3.131	0.262	87.023	27.873	3.006	0.242	83.7862
9:40	28.472	4.651	0.326	132.423	28.343	4.377	0.296	124.057
9:45	31.534	3.936	0.262	124.118	31.477	3.708	0.256	116.717
9:50	30.226	4.952	0.334	149.679	30.611	4.039	0.316	123.638
9:55	30.490	4.953	0.334	151.017	30.725	4.370	0.326	134.268
10:00	31.418	4.186	0.286	131.516	30.169	4.337	0.266	130.843
10:05	29.175	4.948	0.342	144.358	31.299	4.394	0.284	137.528
10:10	31.723	3.237	0.230	102.688	29.812	4.310	0.302	128.490
10:15	27.818	1.918	0.198	53.355	27.771	1.841	0.194	51.126
10:20	31.373	3.208	0.260	100.645	31.411	3.814	0.260	119.802
10:25	29.475	4.781	0.310	140.92	30.751	4.204	0.328	129.277
10:30	32.589	2.957	0.214	96.366	32.192	2.925	0.222	94.162
10:35	32.141	3.652	0.246	117.378	33.621	2.706	0.240	90.978
10:40	33.021	2.259	0.198	74.594	33.153	1.747	0.210	57.918
10:45	33.72	1.205	0.126	40.6326	33.696	1.198	0.140	40.368
10:50	31.182	4.125	0.286	128.626	31.434	4.197	0.280	131.929
10:55	30.518	4.692	0.230	143.191	30.596	4.589	0.296	140.405
11:00	30.090	4.949	0.326	148.915	30.513	4.716	0.314	143.899
11:05	31.234	3.926	0.262	122.624	31.547	3.196	0.264	100.824

11:10	32.701	1.891	0.182	61.838	33.418	1.812	0.184	60.553
11:15	30.903	3.816	0.278	117.926	30.544	4.167	0.278	127.277
11:20	30.792	4.080	0.286	125.631	31.941	2.512	0.212	80.236
11:25	32.295	2.405	0.190	77.670	33.218	1.983	0.186	65.871
11:30	31.743	2.539	0.198	80.595	30.160	4.229	0.296	127.547
11:35	31.734	3.750	0.254	119.003	31.514	4.150	0.272	130.783
11:40	30.535	4.802	0.318	146.629	30.350	4.399	0.306	133.510
11:45	31.607	3.214	0.230	101.585	31.620	3.163	0.242	100.014
11:50	30.120	4.860	0.326	146.383	30.277	4.402	0.342	133.279
11:55	31.295	2.888	0.226	90.380	31.739	2.756	0.224	87.473
12:00	30.806	4.906	0.326	151.134	29.677	4.809	0.332	142.717
12:05	30.812	4.030	0.270	124.172	30.935	4.290	0.288	132.711

I.3 Temperatures: Day 2

Sample Time	Solar Panel 1 (C°)	Solar Panel 2 (C°)
7:06	10.773	10.984
7:16	11.625	12.312
7:31	14.695	15.992
7:46	18.000	19.844
8:16	24.453	25.344
8:31	27.508	28.781
8:46	28.500	29.805
9:01	28.867	30.211
9:16	29.859	31.164
9:31	34.695	36.445
9:46	33.102	34.906
10:01	37.320	39.570
10:16	32.078	33.102
10:31	34.570	35.797
10:46	39.547	40.891
11:01	43.422	45.344
11:16	48.656	50.234
11:31	43.641	44.891
11:46	44.922	46.398
12:01	49.820	52.000

I.4 MPPT Data: Day 2

Time	PV Voltage (V)	PV Current (A)	Battery Voltage (V)	Charge Current (A)
7:08	32.848	0.002	24.192	0
7:25	29.033	0.944	26.342	0.929
7:30	29.205	1.103	26.487	1.130
7:35	29.368	1.292	26.630	1.312
7:40	29.550	1.482	26.747	1.514
7:45	29.358	1.654	26.859	1.712
7:50	29.538	1.818	26.967	1.868
7:55	31.195	1.806	27.024	1.995
8:00	31.355	1.953	27.125	2.157